Astronomy Reports, Vol. 49, No. 2, 2005, pp. 102–108. Translated from Astronomicheskiĭ Zhurnal, Vol. 82, No. 2, 2005, pp. 123–130.

Gravitational Darkening Coefficients of the Stars in the Semidetached Binary V Puppis

E. A. Antokhina, E. V. Seifina, and A. M. Cherepashchuk

Sternberg Astronomical Institute, Universitetskiĭ pr. 13, Moscow, 119899 Russia

Received January 18, 2004; in final form, May 27, 2004

Abstract—We have analyzed high-precision *vby* light curves for the semi-detached binary V Pup in a Roche model. They are consistent with the standard gravitational darkening coefficient for hot stars, $\beta = 0.25$, rather than the value $\beta = 1.36 \pm 0.04$ derived by Kitamura and Nakamura [1] using a simpler model. We rigorously estimate the confidence intervals for the allowed gravitational darkening coefficients for a star filling its Roche lobe to be $\beta = (-0.24, +1.29)$ for the 99% confidence level and $\beta = (-0.21, +1.26)$ for the 67% confidence level. © *2005 Pleiades Publishing, Inc.*

1. INTRODUCTION

V Pup (HD 6518; $P = 1.454^{\mathrm{d}}$) is an eclipsing binary system. Its binarity was first discovered by Williams [2] in 1886, and the star was found to be a spectral binary by Pickering [3] in 1896. According to [4], the system consists of B1V + B3 components; the B1V primary is confined within its Roche lobe, while the B3 secondary fills or overfills its Roche lobe. Thus, V Pup is usually classified as a semi-detached binary.

Andersen *et al.* [5] carried out extensive spectral and photometric studies of V Pup. The spectroscopic data made it possible to determine reliable orbital elements and the component-mass ratio. The light curves [5, 6] were analyzed using the technique developed by Wilson and Devinney [7] assuming synchronous rotation of the components along circular orbits and taking into account "third light." The temperature of the primary ($T_h = 27\,000$ K), component-mass ratio ($q = M_h/M_c = 0.53$), and bolometric albedo ($A_h = A_c = 0.5$) and gravitational darkening coefficients $\beta_h = \beta_c = 0.25$ of the components were estimated. Linear limb darkening was assumed in these calculations. The theoretical and observed light curves were consistent; the system's parameters (absolute size, mass, and temperature of the stars, etc.) were estimated and some conclusions were drawn concerning the semi-detached model considered and a possible evolution scenario for V Pup. According to these data, the contribution of third light in the system does not exceed 5% at yellow wavelengths.

Kitamura and Nakamura [1] analyzed light curves of V Pup and eight other semi-detached systems obtained by Andersen *et al.* [5] and Clausen *et al.* [6] to study gravitational darkening for stars filling their Roche lobes. These same authors had previously carried out a series of studies of the gravitational darkening coefficient β in different types of binaries, including detached systems containing B1V–A2V main-sequence stars [8]. The gravitational darkening coefficients obtained were consistent with $\beta = 0.25$, in agreement with the theory of radiative energy transport in stars [9]. Based on this result, Kitamura and Nakamura [1] fixed the gravitational darkening coefficient of one of the components (the main-sequence star) to be $\beta = 0.25$ in their study of gravitational darkening in stars in semi-detached binaries, leaving β in the Roche-lobe-filling star as a free parameter.

They obtained fits to the light curves using the Russell–Merrill method, allowing for ellipticity and reflection effects. Their fit of *vby* light curves of V Pup yielded $\beta = 1.36 \pm 0.04$ for the cooler and less massive component ($\alpha = 5.44 \pm 0.16$—see explanation below). The authors noted that this high gravitational darkening coefficient for the secondary cannot be removed by varying the other parameters of the system.

Here and below, we will use β in the gravitational darkening law describing the temperature of a surface element on the star:

$$T = T_0(g/g_0)^{\beta}, \tag{1}$$

where g and g_0 are the local and average gravitational accelerations, and T_0 is the average effective temperature of the star.

The coefficient α characterizing the flux ratio [10] is also sometimes used to describe the gravitational darkening law (see, for example, [1]). The relationship between these two coefficients is

$$\alpha = 4\beta. \tag{2}$$

We can see that the value $\alpha = 1.0$ (used in [1]) corresponds to $\beta = 0.25$.

1063-7729/05/4902-0102$26.00

Table 1. Input parameters for the synthesis of the theoretical close-binary light curves in the Roche model

Input parameters of the code for the light-curve synthesis	
$q = M_h/M_c$	Component-mass ratio
e	Eccentricity
ω	Longitude of periastron of the primary
i	Orbital inclination
μ_h, μ_c	Roche lobe filling factors for the stars; $\mu = R/R^*$, where R and R^* are the polar radii for partial and total filling of the critical Roche lobes at periastron ($0 < \mu \leq 1$)
F_h, F_c	Ratios of the rotational velocities of the stars and the velocity of synchronous rotation
T_h, T_c	Average effective temperatures of the stars
β_h, β_c	Gravitational darkening coefficients (temperature of a surface element of the primary $T = T_h(g/g_0)^{\beta_h}$, where g and g_0 are the local and average gravitational accelerations)
A_h, A_c	Bolometric albedo (coefficients for reemission of the incident radiation of its companion star)
u_h, u_c	Limb-darkening coefficients at various wavelengths $\lambda(n)$ for a linear limb-darkening law
$x_{h,c}$, $y_{h,c}$	Monochromatic limb-darkening coefficients in the nonlinear (square-root) limb-darkening law: $I(\cos\gamma) = I(1)[1 - x(1 - \cos\gamma) - y(1 - \sqrt{\cos\gamma})]$, where γ is the angle between the line of sight and the normal to the stellar surface

The effect of gravitational darkening was also studied for eight similar systems in [1], where it was shown that the empirical gravitational darkening coefficients derived for the secondaries substantially exceeded the theoretical values ($\beta > 0.25$). It is reasonable to suppose that the high gravitational darkening coefficients obtained by Kitamura and Nakamura [1] are associated with the simplified binary model they used. This is confirmed by the fact that Andersen *et al.* [5] were able to obtain good consistency between theoretical and observed light curves of V Pup using the standard value, $\beta = 0.25$.

In a recent study of the gravitational darkening in binaries considered in [1], Djurasevic *et al.* [11] derived substantially lower gravitational darkening coefficients for the secondaries than in [1], using the same observational data and initial parameters as in [1], but analyzing the light curves in a Roche model. Nevertheless, their empirical estimates of the gravitational darkening coefficients for V Pup and several other systems diverged from the theoretical value [9]. For example, the gravitational darkening coefficient $\beta_c \sim 0.383$ was obtained for the V Pup secondary [11]—a factor of 1.5 higher than predicted by the theory of radiative energy-transport in stars ($\beta_c = 0.25$). Djurasevic *et al.* [11] explain this difference as a consequence of mass transfer in the systems, as well as deviation of the shape of the equipotential surfaces from that assumed in a classical Roche model (due to the influence of radiation pressure) and deviation of the rotation of the stars from differential rotation. Note that the solution found in [11] is only one of the solutions that fall within the derived range of possible β_c (see below).

Here, we study light curves of V Pup [5, 6] using the same initial parameters as in [1, 11] in order to determine the gravitational darkening coefficient β_c for the secondary and the corresponding confidence intervals using rigorous statistical characteristics. We analyze the light curves in a Roche model, which is more adequate for close binaries than the model used by Kitamura and Nakamura [1].

2. THE MODEL OF THE SYSTEM

Multicolor light curves of V Pup were analyzed using our procedure for synthesizing theoretical light curves and radial-velocity curves in a Roche model [12]. This procedure is similar to the well-known procedure of Wilson [7], which is generally acknowledged as the most adequate technique for light-curve fitting and is widely used in studies of light curves of close binaries. Our procedure is described in detail in [12], and we briefly review here the basic aspects of the model. It is assumed that stars with thin atmospheres move along elliptical orbits about their common center of mass (in the case of V Pup,

Table 2. Fixed input parameters for the synthesis of the V Pup light curve

Parameter	Value	Reference
$q = M_h/M_c$	0.53	[5]
μ_c	1.0	[1, 5]
T_c	26 600 K	[1]
β_h	0.25	[1]

the orbit is assumed to be circular). The shape of each star is described by the equipotential surface in the Roche model. Gravitational darkening, edge darkening, and heating of the atmosphere of the star by the radiation of its companion (the reflection effect) are included. Table 1 presents the input parameters for the synthesis of the theoretical light curves of the close binary in the Roche model. We denote quantities for the hot primary with the subscript h and those for the cooler secondary with the subscript c when comparing our results with those of other studies.

Some of the parameters can be fixed based on the available information about the system (see [1] and references therein). Since the orbit of V Pup is circular and the stars rotate synchronously [5], we fix the eccentricity to be $e = 0$ and the rotational-synchrony parameters to be $F_h = F_c = 1$. According to [5], the component-mass ratio is $q = M_c/M_h = 0.53$. It is also known [1] that the (cooler and less massive) secondary fills its Roche lobe. Therefore, we fixed the Roche-lobe filling factor to be $\mu_c = 1$ and the average effective temperature of the secondary to be $T_c = 26\,600$ K. As in [1], we set the gravitational darkening coefficient for the hotter and more massive primary to be $\beta_h = 0.25$ (the standard value for stars with radiative energy transport). The free parameters in the fits were the orbital inclination i, the Roche-lobe filling factor μ_h, the temperature of the primary T_h, and the gravitational darkening coefficient β_c for the secondary. Table 2 presents the fixed model parameters. Our aim was to elucidate whether it is possible to describe the observed light curves of V Pup adequately using a more correct model for the binary and avoiding the high gravitational darkening coefficient for the secondary, β_c, obtained in [1] by appropriately adjusting the other system parameters (i, μ_h, and T_h).

To study the sensitivity of the theoretical light curves to various effects, we considered two values of the reflection factor ($A_{h,c} = 0.5$ and $A_{h,c} = 1$) and two types of edge-darkening law (linear and nonlinear). Table 3 presents the edge-darkening coefficients for both laws. The coefficients for the linear edge-darkening law were taken from [13]. A new

Table 3. Limb-darkening coefficients for linear and nonlinear laws

Limb-darkening coefficient	λ, Å		
	4110 (v)	4670 (b)	5470 (y)
Linear law			
u_h	0.35	0.32	0.27
u_c	0.36	0.33	0.28
Nonlinear law			
x_h	−0.141	−0.128	−0.146
y_h	0.712	0.717	0.698
x_c	−0.146	−0.114	−0.115
y_c	0.644	0.647	0.598

nonlinear edge-darkening law (the square-root law) was suggested in [14–16]: $I(\cos\gamma) = I(1)[1 - x(1 - \cos\gamma) - y(1 - \sqrt{cos\gamma})]$, where γ is the angle between the line of sight and the normal to the stellar surface. As was shown in [16], this edge-darkening law is the best to use at optical wavelengths when $T \geq 10\,000$ K. The monochromatic edge-darkening coefficients (Table 3) were taken from the CD-ROM Appendix to [16]. For the adopted system parameters, the average gravitational accelerations for the primary and secondary are $\log g = 4.0$ and $\log g = 3.9$, respectively.

Monochromatic theoretical light curves were calculated for the three wavelengths $\lambda = 4110, 4670$, and 5470 Å, corresponding to the central wavelengths of the v, b, and y filters.

3. LIGHT-CURVE ANALYSIS

As in [1], we used the normal v, b, y light curves of V Pup published by Andersen *et al.* [5] for the analysis. Individual observations of V Pup are presented in [6]. We did not use the u light curves, since the blackbody approximation used in our model is not applicable at wavelengths shorter than the Balmer limit.

We selected the best-fit solutions by minimizing the weighted sum of the squared deviations of the theoretical from the observed light curve. The deviation was calculated as the sum of the deviations for the v, b, y light curves:

$$\chi^2_\Sigma = \chi^2_v + \chi^2_b + \chi^2_y. \quad (3)$$

The normal light curves contained 108 points for each filter, so that the total number of normal points in the three filters was $N = 324$; the χ^2_{N-3} critical value was

Table 4. Results of the fitting of the V Pup light curves. (The parameter intervals were determined using the χ^2 test.)

Parameter	Confidence intervals			
	Linear limb-darkening law		Nonlinear limb-darkening law	
For 99% confidence level				
$A_{h,c}$	0.5	1.0	0.5	1.0
β_c	−0.29–1.09	−0.23–1.25	−0.29–1.13	−0.24–1.29
T_h, K	25600–33200	24500–33100	25200–33400	24500– 33400
μ_h	0.82–0.98	0.84–0.98	0.83–0.97	0.84–0.98
i, deg	77.3–79.5	76.2–79.1	76.9–79.6	76.2–79.2
For 67% confidence level				
$A_{h,c}$	0.5	1.0	0.5	1.0
β_c	−0.26–1.07	−0.2–1.22	−0.26–1.11	−0.21–1.26
T_h, K	25400–32600	24500–32700	25200–33200	24500–33000
μ_h	0.83–0.97	0.82–0.97	0.82–0.97	0.83–0.97
i, deg	77.1–79.4	76.5–79.3	77.1–79.5	76.4–79.3

390 for the 1% significance level and 346 for the 33% significance level. The mean error of the points in the normal light curve is 0.007^m for all three filters [5, 6].

Recall that, with the fixed system parameters given in Table 2, the free parameters in the fit were i, T_h, μ_h, and β_c. The best-fit solution was found via a direct exhaustive search for β_c, which enabled us to derive the errors in β_c from the light curves. Thus, we found the i, T_h, and μ_h values for a fixed β_c for which the sum of the squared deviations of the theoretical from the observed light curves reached a minimum. The gravitational darkening coefficient was varied in the interval $\beta_c = -0.4–1.5$.

Table 4 presents the calculated allowed intervals for the system parameters for the 99 and 67% confidence levels estimated according to the χ^2 test. Figure 1 displays the minimum of the χ^2_Σ deviation for i, T_h, and μ_h as a function of β_c for two reflection factors. Note that each point in Fig. 1 results from a minimization over three parameters (i.e., there are $N-3$ degrees of freedom, where N is the total number of normal points in the v, b, y light curves), so that the distribution of the total set of points is somewhat different from χ^2. It was shown in [17] that, in the case of minimization over nonlinear parameters, the residuals are distributed as χ^2 only asymptotically, when $N \to \infty$. Since N is very large in our case ($N = 324$), we expect that our residual distribution should follow the χ^2_{N-3} law.

In [1], errors are given for the 1σ significance level, and we, accordingly, have marked the 33% significance level in Fig. 1, so that the results would be compatible.

Figure 1 and Table 4 indicate that the above model describes the observations of [5] adequately over a fairly broad range of parameters; the gravitational

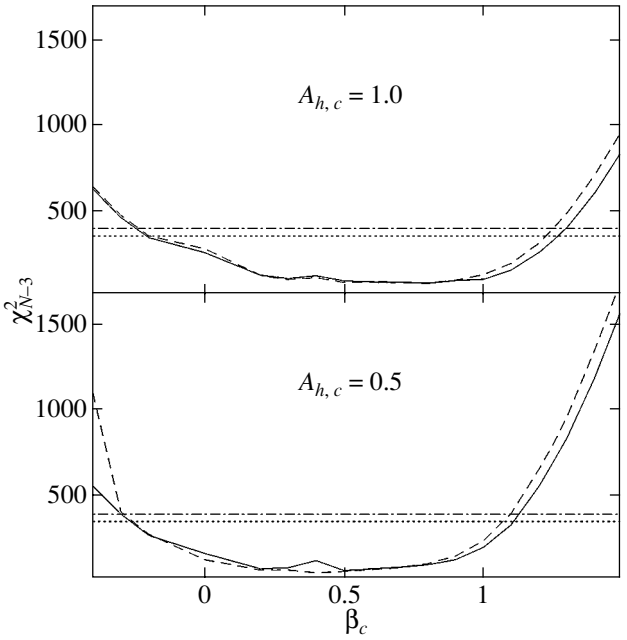

Fig. 1. Minimum residuals χ^2_{N-3} for the parameters i, T_h, and μ_h as a function of β_c for albedos $A_{h,c} = 1.0$ (top) and $A_{h,c} = 0.5$ (bottom). The solid and dashed curves correspond to nonlinear and linear edge-darkening. The dot–dashed and dotted horizontal lines indicate the critical residuals χ^2_Σ for the 1% and 33% (1σ) significance levels.

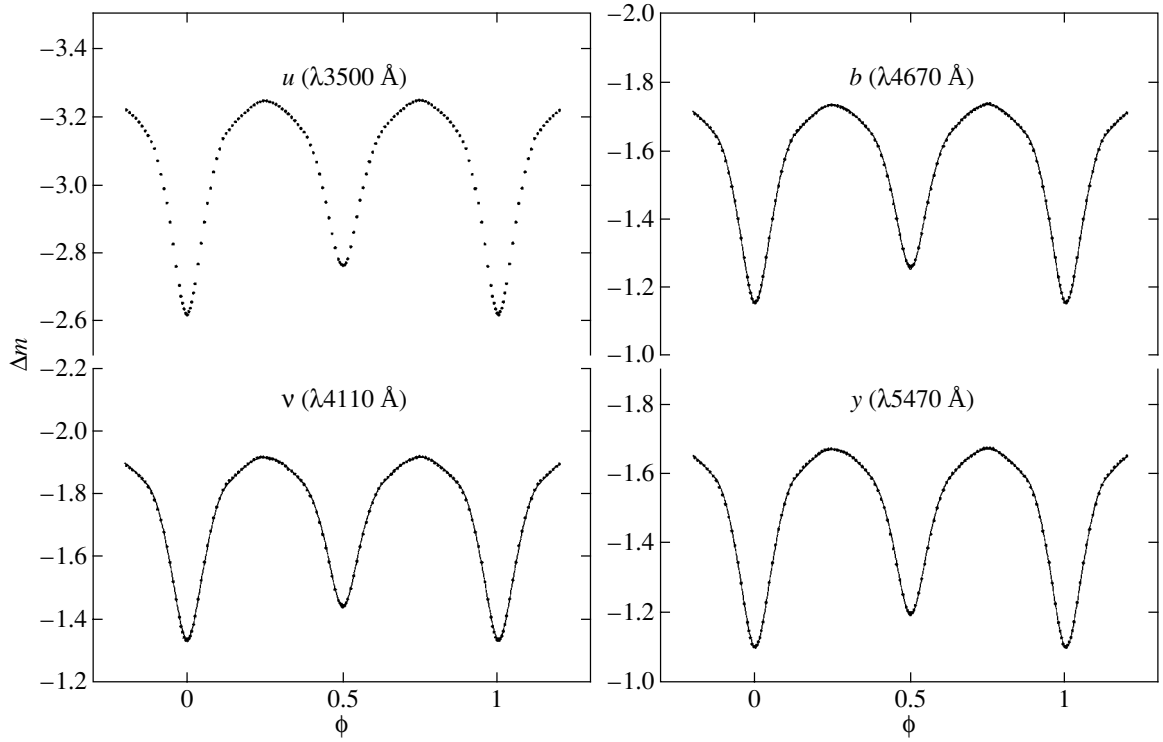

Fig. 2. Best-fit theoretical light curves for the semi-detached binary V Pup (solid curves). The dots represent the observed normal light curves published in [5]. The parameters of the binary obtained for the nonlinear (square-root) edge-darkening law for the 1% significance level are $q = M_h/M_c = 0.53$, $i = 77.8°$, $\mu_h = 0.90$, $\mu_c = 1.0$, $T_h = 27\,800$ K, $T_c = 26\,600$ K, $\beta_h = 0.25$, $\beta_c = 0.25$, and $A_{h,c} = 1.0$.

darkening coefficient β_c is consistent with that expected for hot stars ($\beta_c = 0.25$). For all versions of the fits, the minimum residuals yield $\beta_c < 1$.

We can see from Fig. 1 that using the albedo $A = 0.5$ or the linear edge-darkening law does not affect the results substantially. Therefore, the value $A = 1.0$ and the square-root edge-darkening law can be given preference, since they are the best to use at optical wavelengths for hot stars.

Figure 2 presents the theoretical light curves providing the best fit to the observations. Figure 3 displays a fragment of the b-band theoretical light curve (λ4670 Å), as well as the theoretical light curves for the ends of the confidence intervals for β_c ($-0.24, +1.29$), so that deviations from the exact light curve can be seen clearly.

Note that we obtained solutions for different sets of parameters (T_h, μ_h, i); the theoretical light curves for the ends of the confidence intervals in Fig. 3 correspond to the minimum residual for these three parameters. The parameters for the solutions at the ends of the confidence intervals are presented in the caption to Fig. 3.

Figure 4 presents a schematic model of V Pup for the best-fit parameters.

Note that the confidence interval for the 99% confidence level includes parameters for which the average effective temperatures of the stars contradict the relation $T_h < T_c$ derived from spectral observations; i.e., for which the theoretical temperature of the cool star exceeds that of the hot star. This occurs when $\beta_c \geq 0.9$, for various A values and edge-darkening laws. Therefore, β_c can be taken to have an upper limit of $\beta_c = 0.9$.

4. CONCLUSION

Based on our study, we conclude that the observed light curves of V Pup can be described with an acceptable level of significance in a Roche model, without substantially increasing the gravitational darkening coefficient for the Roche-lobe-filling secondary. It may be that the high β_c value obtained in [1] is due to the simpler model (compared to the Roche model) used for the binary system. The high gravitational darkening coefficient ($\beta_c = 0.380 \pm 0.006$ for the v band) derived for V Pup in [11] using a Roche model lies within the allowed interval for β_c. Thus, only one particular allowed solution was found in [11]. Our analysis of the V Pup light curves, as well as the earlier analysis by Andersen *et al.* [5] using the Wilson–Devinney method, indicate that a

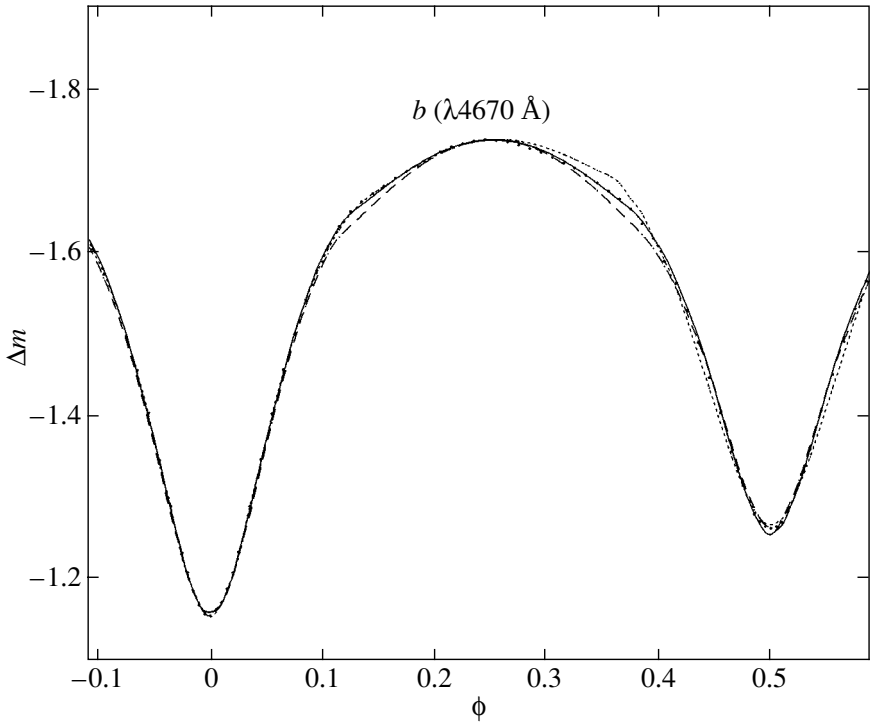

Fig. 3. Fragment of the theoretical b light curve (λ4670 Å) for orbital phases $-0.1-0.55$. Corresponding theoretical light curves for the ends of the confidence intervals for $\beta_c = 0.25$ (-0.24, 1.29) are presented for comparison. The dots represent the observed normal light curves. The solid curve indicates the solution with the minimum residual, whose parameters are given in the caption to Fig. 2. The parameters of the solution for the ends of the 99% confidence level for the model with nonlinear edge darkening are $i = 79.2°$, $\mu_h = 0.98$, $T_h = 33\,400$ K, $q = M_h/M_c = 0.53$, $\mu_c = 1.0$, $T_c = 26\,600$ K, $\beta_h = 0.25$, and $A_{h,c} = 1.0$ for $\beta_c = -0.24$ (dotted curve); and $i = 76.2°$, $\mu_h = 0.84$, $T_h = 24\,500$ K, $q = M_h/M_c = 0.53$, $\mu_c = 1.0$, $T_c = 26\,600$ K, $\beta_h = 0.25$, and $A_{h,c} = 1.0$ for $\beta_c = -1.29$ (dashed curve).

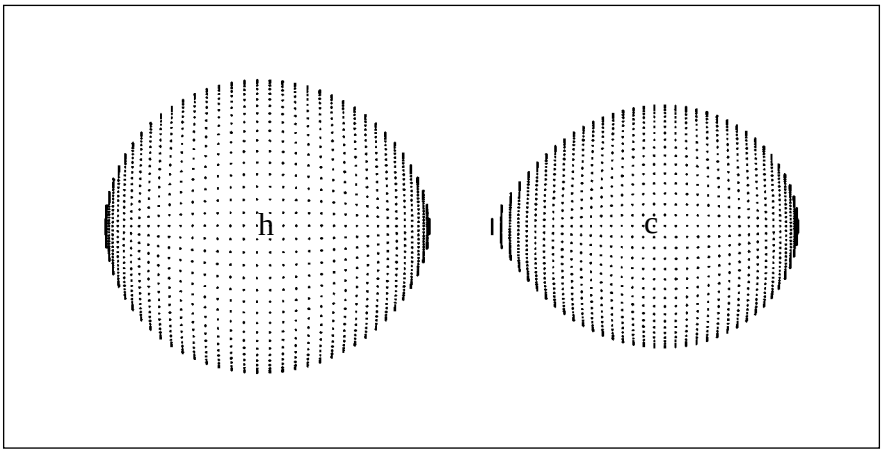

Fig. 4. Schematic geometrical model of V Pup. The letters h and c denote the primary (B1V) and secondary (B3) components. The model parameters are $q = M_h/M_c = 0.53$, $\mu_h = 0.90$, $\mu_c = 1.0$, and $i = 77.8°$.

satisfactory fit to the observations can be acquired for the gravitational darkening coefficient $\beta_c = 0.25$, predicted by the theory of von Zeipel [9] for stars with radiative energy transport.

The final gravitational darkening coefficients derived in our model are $\beta_c = 0.25$ (-0.24, $+1.29$) for the 99% and $\beta_c = 0.25$ (-0.21, $+1.26$) for the 67% confidence levels. The values for the ends of the confidence intervals are given in parentheses. It is clear that our results contradict those of [1], are consistent

with those of [11], and are fully consistent with the theoretical value $\beta_c = 0.25$ for stars with radiative atmospheres.

ACKNOWLEDGMENTS

This work was supported by a Grant of the President of the Russian Federation to Support Leading Scientific Schools of Russia (NSh-388.2003.2) and the Russian Foundation for Basic Research (project no. 02-02-17524).

REFERENCES

1. M. Kitamura and Y. Nakamura, Ann. Tokyo Astron. Obs. **21**, 387 (1987).
2. A. S. Wiliams, Mon. Not. R. Astron. Soc. **47**, 91 (1886).
3. E. C. Pickering, Astron. Nachr. **142**, 107 (1896).
4. B. Cester, B. Fedel, G. Giurich, *et al.*, Astron. Astrophys. **61**, 275 (1977).
5. J. Andersen, J. V. Clausen, A. Gimenez, *et al.*, Astron. Astrophys. **128**, 17 (1983).
6. J. V. Clausen, B. Nordstrom, and B. Reipurth, Astron. Astrophys., Suppl. Ser. **52**, 323 (1983).
7. R. E. Wilson, Astrophys. J. **234**, 1034 (1979).
8. M. Kitamura and Y. Nakamura, Ann. Tokyo Astron. Obs. **21**, 331 (1986).
9. Von. H. Zeipel, Mon. Not. R. Astron. Soc. **84**, 684 (1924).
10. R. E. Wilson and E. J. Devinney, Astrophys. J. **166**, 605 (1971).
11. G. Djurasevic, H. Rovithis-Livaniou, P. Rovithis, *et al.*, Astron. Astrophys. **402**, 667 (2003).
12. E. A. Antokhina, Astron. Zh. **73**, 532 (1996) [Astron. Rep. **40**, 483 (1996)].
13. H. M. Al-Naimiy, Astrophys. Space Sci. **53**, 181 (1978).
14. J. Diaz-Cordoves and A. Gimenez, Astron. Astrophys. **227**, 259 (1992).
15. J. Diaz-Cordoves, A. Claret, and A. Gimenez, Astron. Astrophys., Suppl. Ser. **110**, 329 (1995).
16. W. Van Hamme, Astron. J. **106**, 2096 (1993).
17. A. M. Cherepashchuk, Astron. Zh. **70**, 1157 (1993) [Astron. Rep. **37**, 585 (1993)].

Translated by K. Maslennikov

Astronomy Reports, Vol. 49, No. 2, 2005, pp. 109–126. Translated from Astronomicheskiĭ Zhurnal, Vol. 82, No. 2, 2005, pp. 131–148.

Radial-Velocity Curves and Theoretical Spectral-Line Profiles of the Components of Low-Mass Close X-ray Binary Systems

E. A. Antokhina[1], A. M. Cherepashchuk[1], and V. V. Shimanskii[2]

[1] *Sternberg Astronomical Institute, Universitetskiĭ pr. 13, Moscow, 119992 Russia*

[2] *Kazan State University, ul. Lenina 18, Kazan, 420008 Tatarstan, Russia*

Received March 30, 2004; in final form, July 15, 2004

Abstract—We present the results of calculations of theoretical absorption-line profiles and radial-velocity curves for optical components in X-ray binary systems. Tidal distortion of the optical star and X-ray heating by incident radiation from the relativistic object are taken into account. An emission component forms whose intensity varies with orbital phase in the absorption-line profile in the presence of significant X-ray heating. As a result, the width of the line decreases rather than increases at quadrature. The line profiles and equivalent widths and the radial-velocity curves depend substantially on the parameters of the binary systems. This provides the possibility of directly determining component masses and orbital inclinations from high-resolution spectroscopic observations of X-ray binary systems. © *2005 Pleiades Publishing, Inc.*

1. INTRODUCTION

Antokhina and Cherepashchuk [1] and Shahbaz [2] suggested a new method to estimate the component-mass ratios q and orbital inclinations i of X-ray binary systems using data on the orbital variability of absorption-line profiles in the spectrum of the optical component. This variability is due to the finite size of the optical star, tidal distortion by the companion, and the complex pattern of its surface-temperature distribution. In point-source or spherical models for binary components, the line profile and, accordingly, the shape of the radial-velocity curve, does not depend on the orbital inclination i. For this reason, radial-velocity curves can yield only the product $m\sin^3 i$ (where m is mass of the star). If a star with a significant size is tidally distorted, the shape of the line profiles and radial-velocity curve depend on i and q. In principle, this provides the possibility of deriving both the component masses and the orbital inclination from the orbital variations of line profiles (or from the corresponding radial-velocity curve). Recently, Abubekerov *et al.* [3] used this approach to estimate the mass of the black-hole component of the X-ray binary Cyg X-1 and the orbital inclination of the system based on a high-precision radial-velocity curve.

In our earlier work [1, 4, 5], we calculated line profiles for tidally-distorted components of binary systems using theoretical hydrogen-line profiles for various effective temperatures T_{eff} and surface gravities g computed by Kurucz [6]. The reflection effect was taken into account using a model implementing a simple summation of the radiated and incident fluxes, without considering the transfer of the incident radiation in the atmosphere of the externally heated star. This approach is not completely correct; in particular, it does not enable us to take into account emission components of the lines that may arise in the case of strong heating by incident radiation. For X-ray binaries, such a crude model is valid only in the case of weak X-ray heating, when the ratio of the bolometric luminosities of the X-ray source (L_x) and optical star (L_v) is $k_x = L_x/L_v < 1$.

In the present study, we have computed absorption-line profiles for a tidally-distorted optical star in an X-ray system by correctly solving for the radiative transfer in the line at a given point of the stellar surface in the presence of external X-ray irradiation.

2. MODEL OF THE BINARY SYSTEM

The basic idea behind the synthesis of theoretical light curves and stellar spectral-line profiles is the decomposition of the complex stellar surfaces into thousands of area elements for which the outgoing local flux is computed. The contributions of the areas are summed for each orbital phase, taking into account the Doppler effects and visibilities of the areas. Thus, for each orbital phase, we can find the radiation flux in the continuum directed toward the observer and the rotationally broadened spectral line profiles, which enables us to determine the radial velocity of the star. Line synthesis is able to allow for effects related to the proximity of the components in a binary system: tidal–rotational distortion of the stars (the ellipticity effect), the nonuniform temperature distribution over the stellar surface due to gravitational

1063-7729/05/4902-0109$26.00

darkening, heating due to irradiation by a companion (the reflection effect), and other effects.

The first version of our line-synthesis algorithm for X-ray binaries with circular orbits was described in [7]. Here, we present a new algorithm for the computation of theoretical line profiles and the construction of radial-velocity curves. The line profiles of area elements on the surface of a star are computed using models in which their atmospheres are subject to incident X-ray radiation. This new algorithm for computing theoretical spectral-line profiles opens broad possibilities for more correct interpretations of spectroscopic observations and the derivation of reliable physical parameters of close binaries. It also makes it possible to derive theoretical line profiles for stars that are subject to ultraviolet or optical irradiation.

We consider here an X-ray binary system. Let us describe the main features of our algorithm for modeling theoretical line profiles for the optical star in the binary and the construction of the binary's radial-velocity curve. The binary consists of an optical star and a relativistic object, which usually move in elliptic orbits about their center of mass. The orbital inclination is i and the component-mass ratio is $q = M_x/M_v$, where M_x is the mass of the relativistic object and M_v the mass of the optical star. The surface of the star coincides with the Roche equipotential surface, and the size of the star is determined by the Roche-lobe filling factor μ_v, where $\mu_v = R/R^*$ is the ratio of the polar radii for partial and total Roche-lobe filling. The star's rotation can be asynchronous with the orbital motion [5], with the degree of asynchronous rotation specified by the parameter $F = \omega_{rot}/\omega_K$, where ω_{rot} is the angular velocity of the rotation, ω_K is the mean Keplerian orbital angular velocity ($\omega_K = 2\pi/P$), and P the orbital period of the binary.

We introduce a Cartesian coordinate system (X, Y, Z) with its origin at the center of mass of the optical star. The X axis is directed along the line passing through the component centers, the Y axis lies in the orbital plane, and the Z axis is perpendicular to the orbital plane. We also introduce a spherical coordinate system (r, η, ψ) with its origin at the center of the optical star. The stellar surface is decomposed into a large number of area elements. Let $\mathbf{r}$ be the radius vector of a surface element, and λ, ν the direction cosines of $\mathbf{r}$ relative to the X, Z axes (see [5] for more details). In the spherical coordinate system (r, η, ψ), the equation for the equipotential surface of the star is [8]

$$\Omega = \frac{1}{r} + q\left(\frac{1}{\sqrt{D^2 + r^2 - 2Dr\lambda}} - \frac{r\lambda}{D^2}\right) + \frac{1}{2}(1+q)r^2F^2(1-\nu^2). \quad (1)$$

Here, D is the instantaneous distance between the centers of the stars moving in elliptical orbits and r is measured in units of D.

The equation for the equipotential surface is solved numerically for every surface element for fixed η, ψ, and the radius vector $\mathbf{r}$ and coordinates x, y, z are found. The local surface gravity $g(\mathbf{r}) = |\mathrm{grad}\Omega|$ is also computed for every surface element (in relative units; it is converted into absolute units later), as well as the coordinates of the unit normal vector

$$\mathbf{n} = -\frac{\mathrm{grad}\Omega}{|\mathrm{grad}\Omega|}. \quad (2)$$

In the first stage of the computations, the temperature of a surface element is found, taking into account only gravitational darkening. The effect of the incident radiation is taken into account later, when the model atmosphere is computed for every element:

$$T(\mathbf{r}) = T_0\left(\frac{g(\mathbf{r})}{g_0}\right)^{\beta}, \quad (3)$$

where T_0 is the mean effective temperature of the star, $g(\mathbf{r})$ and g_0 are the local gravity and the effective gravity averaged over the stellar surface, and β is the gravitational-darkening coefficient. For a star in radiative equilibrium, $\beta = 0.25$ [9], while $\beta = 0.08$ for a star with a convective envelope [10].

We can compute for each surface element the parameter K_x^{loc}: the ratio of the incident X-ray flux H and the total flux radiated by the corresponding non-irradiated atmosphere H_0:

$$K_x^{loc} = \frac{H}{H_0} = \frac{k_x L_v \cos\theta}{4\pi\rho^2\sigma T^4(\mathbf{r})}. \quad (4)$$

Here, k_x is the ratio of the X-ray luminosity of the compact object and the bolometric luminosity of the star, L_v is the bolometric luminosity of the optical star, σ is the Stefan–Boltzmann constant, $T(\mathbf{r})$ is the effective temperature of the surface element, θ is the angle between the normal to the surface and the direction to the X-ray source, and ρ is the distance from the center of the surface element to the X-ray source. For surfaces that are not subject to incident radiation, $K_x^{loc} = 0$. The value of K_x^{loc} is an input parameter for the routine that computes the local model atmosphere for a surface element; this procedure will be described in the next section.

To compute the stellar emission at various orbital phases, we introduce a stationary Cartesian coordinate system $(\overline{X}, \overline{Y}, \overline{Z})$ with its origin at the star's center of mass. The relative rotation angle of the components θ_{orb} is the angle between the X and $\overline{X}$ axes. At orbital phase $\varphi = 0$, the first star eclipses the secondary and $\theta_{orb} = 0°$. The coordinates of a unit

vector pointing in the direction of the observer in the moving (X, Y, Z) coordinate system are

$$\mathbf{a}_0 = (-\sin i \cos\theta_{orb}, -\sin i \sin\theta_{orb}, \cos i) \quad (5)$$
$$= (a_x, a_y, a_z).$$

The cosine of the angle γ between the normal to the surface element and the direction to the observer is then defined as the scalar product $\cos\gamma = (\mathbf{a}_0, \mathbf{n})$. If $\cos\gamma > 0$, a surface element can be seen by the observer. The total observed emission of the star is obtained by summing the fluxes from all observable surface elements in the direction toward the observer at each orbital phase.

Let consider the procedure for computing the velocities of the surface elements relative to the star's center of mass. Let us take a surface element with its center at the coordinates (x, y, z). The velocity of the element $\mathbf{v}$ relative to the center of mass in the stationary coordinate system (X, Y, Z) is

$$\mathbf{v} = [\boldsymbol{\omega}_{rot}, \mathbf{r}] = (\omega_{rot} y, -\omega_{rot} x, 0). \quad (6)$$

Here, $\boldsymbol{\omega}_{rot}$ is the angular velocity of the stellar rotation, $\boldsymbol{\omega}_{rot} = (0, 0, \omega_z = \omega_{rot} = \omega)$. The projection of $\mathbf{v}$ onto the line of sight directed away from the observer (when the velocity is positive away from the observer) is

$$v_r = (-\mathbf{v} \cdot \mathbf{a}) = (\omega_{rot} y, -\omega_{rot} x, 0) \quad (7)$$
$$\times (-a_x, -a_y, -a_z) = -\omega_{rot} y a_x + \omega_{rot} x a_y.$$

Let the radial velocity of the center of mass of the star be V_c. The resultant velocity of the surface element relative to the center of mass of the system (projected onto the line of sight) is then

$$V_r = v_r + V_c. \quad (8)$$

Thus, it is possible to compute the radial velocities of all the surface elements over the star for every orbital phase. The summation of the local spectral-line profiles and computation of the total line profile for a star at different orbital phases is done taking into account the Doppler shifts of the local profiles relative to the velocity of the center of mass of the star.

Let us now describe the procedure for computing the local absorption-line profile of a surface element with effective temperature T, local effective gravity g, and irradiation parameter K_x^{loc}, which is the ratio of the incident X-ray flux to the emitted flux (in the absence of irradiation).

3. COMPUTATION OF THE MODEL ATMOSPHERE AND THE EMISSION SPECTRUM FOR A SURFACE ELEMENT

To correctly compute the continuum emission and line profiles of the local surface elements, it is necessary to make a preliminary estimate of the structure of the stellar atmosphere in the presence or absence of irradiation. In general, this requires that we solve the radiative-transfer equations

$$\mu \frac{dI_\nu}{dr} = \alpha_\nu (S_\nu - I_\nu) \quad (9)$$

for a set of frequencies ν, some of which are present in the incident flux, which has angle of incidence θ ($\mu = \cos\theta$) and power μI_ν^+.

The standard conditions of radiative and hydro-

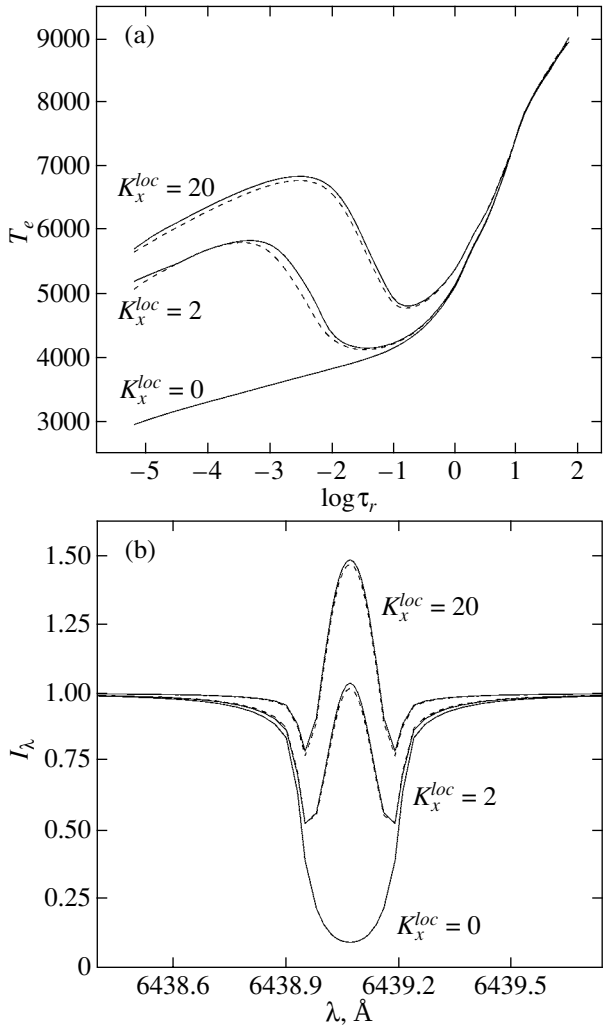

Fig. 1. (a) Comparison of the distributions of the electron temperature T_e in models computed using the method of heating- and cooling-function balance (dashed) and in precise blanketed models with atmospheric parameters $T_{eff} = 4752$ K, $\log g = 2.63$ and various irradiation coefficients K_x^{loc} (solid). (b) Comparison of the CaI λ6439.075 Å line profiles computed for the atmospheres shown in (a).

static stability are fulfilled for each atmospheric layer:

$$\int_0^\infty \int_{-1}^{1} \alpha_\nu I_\nu d\mu d\nu = \int_0^\infty \int_{-1}^{1} \alpha_\nu S_\nu d\mu d\nu, \qquad (10)$$

$$\frac{dp}{dm} = g, \qquad (11)$$

where m is the mass of a unit column of gas measured down from the upper boundary. The solution of this problem using standard software packages developed for nonirradiated atmospheres (e.g., ATLAS 9 [11]) encounters considerable difficulties, due to the dependence of the incident radiation on the angle θ, which is close to a δ function. This contradicts the basic assumption that the radiation intensity depends smoothly on μ, which is applied in subroutines for the numerical solution of the radiative-transfer equation in ATLAS-type software packages.

For this reason, we suggest a different approach to computing the atmospheric structure, which takes into account the lack of any direct interaction between the incident radiation and the intrinsic stellar radiation. In the first step of this procedure, the set of equations (9) is solved with a nonzero upper boundary condition, specified values of μ, and a source function S_ν that is equal to zero. This yields the dependences of the distributions of the mean intensity J_ν and the flux H_ν on the optical depth τ_ν at the frequency ν in the form

$$J_\nu^+(\tau_\nu) = I_\nu^+ \exp(-\tau_\nu/\mu), \qquad (12)$$

$$H_\nu^+(\tau_\nu) = \mu I_\nu^+ \exp(-\tau_\nu/\mu). \qquad (13)$$

In the second step, Eqs. (9) are solved again, but with a zero upper boundary condition, a set of μ values, and a source function determined by the sum of the total scattered (including external) radiation and the Planck function for each layer:

$$S_\nu = \frac{2\alpha_\nu' B_\nu(\tau_v) + \sigma_e \int_{-1}^{1} I_\nu d\mu}{2(\alpha_\nu' + \sigma_e)}, \qquad (14)$$

where α_ν' and σ_e are the true-absorption and electron-scattering coefficients.

A simple expression for the distribution of the source function over optical depth is given in [12], where this problem is solved for a gray model with mean opacity coefficients for the external and intrinsic radiation α_x and α_v:

$$S(\tau_v) = S^0(\tau_v) + I^+ \frac{\alpha_x}{\alpha_v} \exp\left(-\frac{\alpha_x \tau_v}{\alpha_v \mu}\right) + \frac{1}{2}\mu I^+ + \frac{3\mu\alpha_v}{4\alpha_x}\mu I^+ \left[1 - \exp\left(-\frac{\alpha_x \tau_v}{\alpha_v \mu}\right)\right] \qquad (15)$$

or

$$S(\tau_v) = S^0(\tau_v) + a_2 S_2(\tau_v) + a_3 S_3(\tau_v) + a_4 S_4(\tau_v), \qquad (16)$$

where $S^0(\tau_v) = \sigma T_e^4$ is the distribution for a non-irradiated atmosphere.

The presence in Eq. (15) of the term $S_2(\tau_v)$, which decreases exponentially with depth, results in a negative gradient $dS(\tau_v)/d\tau_v$ in the upper layers of the stellar atmosphere; i.e., in the formation of a high-temperature chromosphere. Equation (15) shows that the source-function excess in the chromosphere is proportional to the ratio α_x/α_v. As was shown in [12], the absorption coefficient of stellar material with T_e below 100 000 K in the X-ray range depends on ν as a power-law with an exponent close to -2.3. Therefore, the presence in the incident flux of even a weak soft component with $E < 2.0$ keV (with $\alpha_x/\alpha_v \gg 1$) results in the rapid growth of the temperature in the chromospheric layers and the development of strong emission features in the emitted stellar spectra. This circumstance demands a rigorous determination of the frequency distribution in the incident flux in the course of the modeling (see also [13]).

Subsequent computations of exact blanketed model atmospheres with irradiation [14] have shown that their temperature structure is described well by Eq. (16). In this case, the terms S_2, S_3, and S_4 must be written in quadrature form:

$$S_2(\tau_v) = \int_{\nu_1}^{\nu_2} \frac{dH_\nu^+(\tau_v)}{d\tau_v} d\nu_x, \qquad (17)$$

$$S_3(\tau_v) = \int_{\nu_1}^{\nu_2} H_\nu^+(\tau_v' = 1) d\nu_x, \qquad (18)$$

$$S_4(\tau_v) = \int_{\nu_1}^{\nu_2} \int_0^{\tau_v} \left(S_2(\tau_v') + H_\nu^+(\tau_v')\right) d\tau_v' d\nu_x. \qquad (19)$$

They are easily found numerically for a given frequency distribution for the incident flux H_ν^+, incidence angle θ, and ratio of the absorption coefficients at the frequencies of the external and intrinsic radiation $\alpha_x(\tau_v)/\alpha_v(\tau_v)$, which is found in the course of the computations. In our method, the absorption coefficient α_x at the frequencies of the incident radiation is computed allowing for ionization from the inner and outer shells of hydrogen, helium, and the 20 most abundant heavy elements in five ionization stages in accordance with Yakovlev *et al.* [15], and also including Thompson scattering. As was shown by Sakhibullin and Shimanskii [14], the absorption

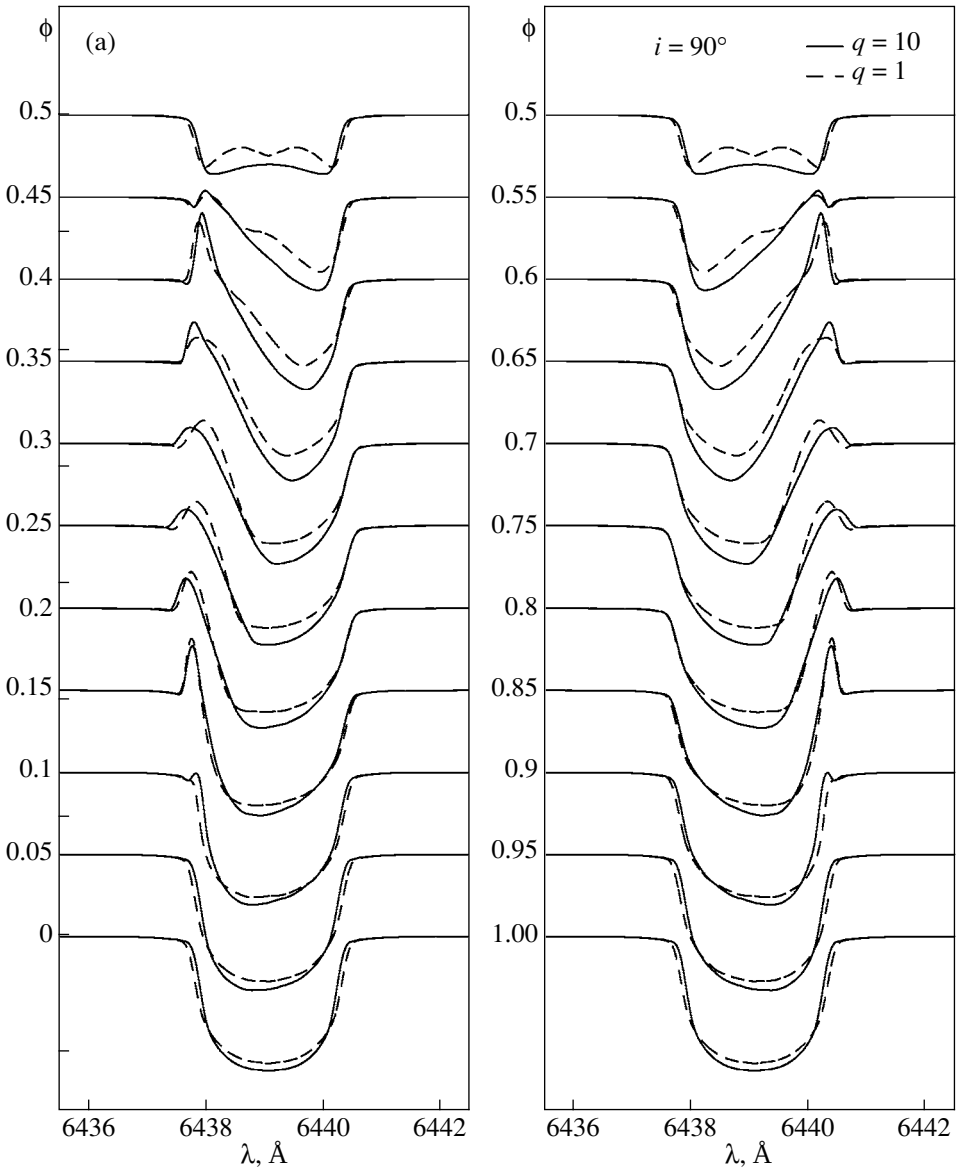

Fig. 2. Orbital-phase variations of the CaI λ6439 Å line profile in the spectrum of an X-ray-irradiated star ($k_x = 10$) for the two orbital inclinations (a) $i = 90°$ and (b) $i = 45°$. The profiles are normalized to the continuum, and Doppler shifts have been subtracted. At phase $\varphi = 0$, the optical star is in front of the X-ray source. The parameters of the optical star are $M_v = 1M_\odot$, $\mu_v = 1$, and $T = 5000$ K. Line profiles are shown for the two component-mass ratios $q = 10$, $M_x = 10M_\odot$ (solid) and $q = 1$, $M_x = 1M_\odot$ (dashed).

coefficient at the frequencies of the intrinsic atmospheric radiation α_v can be represented with high accuracy by combinations of Planck and Rosseland absorption coefficients, α_p and α_r. Fitting our models of irradiated atmospheres obtained using this method and of exact blanketed models obtained using the BINARY 3 code [14] yielded the following expression for α_v [16]:

$$\alpha_v = (\alpha_r^{5.97+0.73\log\tau_r}\alpha_p)^{\frac{1}{6.97+0.73\log\tau_r}}. \qquad (20)$$

Simultaneously, the weight coefficients for the components of the complete source function (16) were found: $a_2 = 0.67$, $a_3 = 0.51$, and $a_4 = 0.63$. Our method for modeling the atmospheres of irradiated stars has certain advantages when applied to binary stars.

(1) The determination of the temperature structure of the irradiated atmosphere is based on the balance of the gas heating and cooling functions, but not on the standard methods of temperature correction. As is noted in [14], the temperature correction diverges for models of irradiated atmospheres if the flux gradients

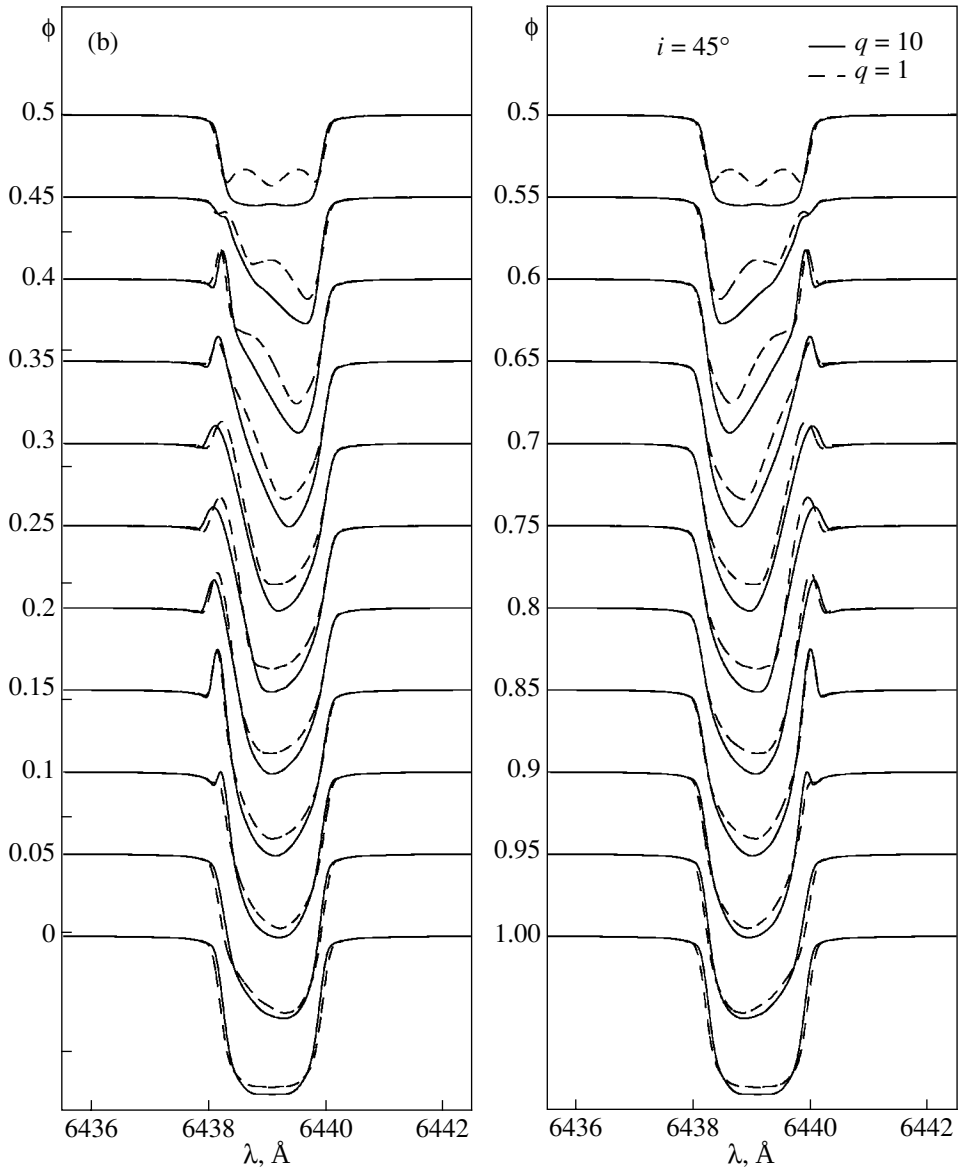

Fig. 2. (Contd.)

in high layers are large. Therefore, as a rule, correction methods cannot be used to compute model atmospheres with strong irradiation. At the same time, the method of heating- and cooling-function balance remains stable even for irradiation coefficients K_x^{loc} in the hundreds. Moreover, since it is not necessary to solve the radiation-transfer equation for optical frequencies, the required computational time decreases by a factor of 30–80, which is especially important for close binary systems.

(2) The source function of the irradiated atmosphere $S(\tau_v)$ is determined by the change of the initial source function of an ordinary atmosphere $S^0(\tau_v)$, when the terms S_2, S_3, and S_4, which depend linearly on H_ν^+, appear. As a result, the temperature structure characteristic of a nonirradiated atmosphere is preserved in the case of small or zero incident fluxes. This makes it possible to use our method to study binary stars and single stars with weak reflection effects. Note that the initial models for the nonirradiated atmospheres were found by interpolating the grids of Kurucz [11] for blanketed models for specified T_{eff} and $\log g$ values, as is described in [17].

(3) Our method is able to compute models of stellar atmospheres irradiated by X-ray, UV, and optical radiation with an accuracy sufficient for numerical studies of close binary stars. It was shown in [16] that the errors in the temperature distribution do not exceed 4% for model atmospheres with incident fluxes

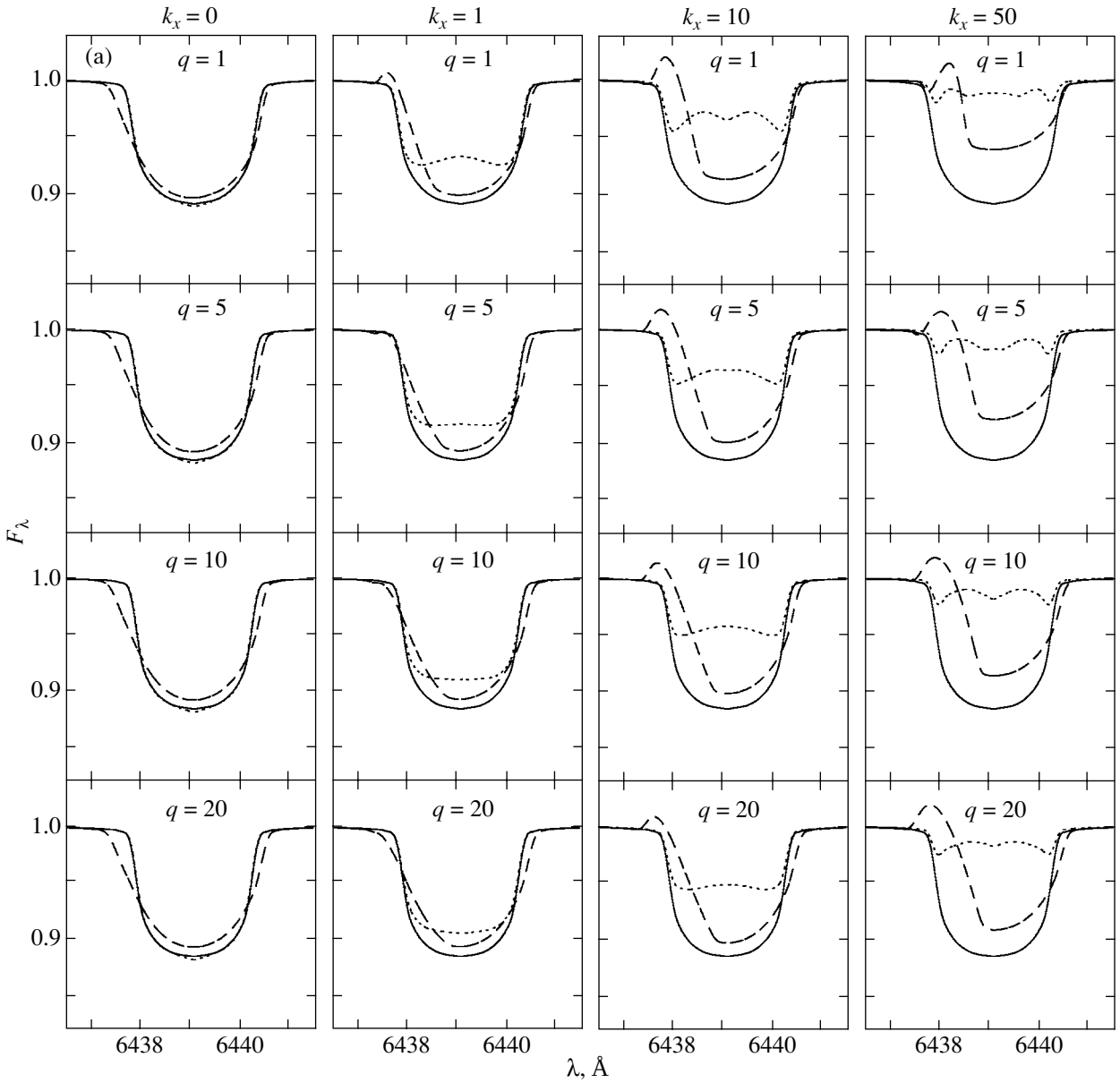

Fig. 3. Dependence of the CaI λ6439 Å line profiles on q and k_x for the two orbital inclinations (a) $i = 90°$ and (b) $i = 45°$. The model parameters cover the ranges $q = 1{-}20$, $k_x = 0{-}50$, $\mu_v = 1$, and $T = 5000$ K, $i = 90°$. The profiles are shown for the three orbital phases $\varphi = 0$, when the X-ray source is behind the optical star (solid), $\varphi = 0.25$, when the star is viewed from the side (dashed), and $\varphi = 0.5$, when the X-ray source is in front of the optical star (dotted).

with $K_x^{loc} < 100$ and for wavelengths 0.30 Å $\leq \lambda \leq$ 50.0 Å, 250 Å $\leq \lambda \leq$ 3000 Å. The corresponding errors in the total radiated fluxes in the regions of the Balmer and Paschen continua are 1–3%.

We compared model atmospheres computed using the above method and blanketed models computed using the BINARY 3 code [14]. Figure 1 shows the results for two sets of input atmospheric parameters for the models in which we are directly interested: $T_{eff} = 4752$ K, $\log g = 2.63$, and $K_x^{loc} =$ 2.0 and 20.0. Figure 1a shows the temperature distributions in the irradiated and nonirradiated atmospheres, while Fig. 1b shows the corresponding CaI λ6439.075 Å line profiles. This comparison shows that the maximum errors in T_e are less than 4% and are larger in the model with weaker irradiation ($K_x^{loc} = 2.0$), in particular, in the narrow transition region from the chromospheric layers to the temperature minimum. The difference in the CaI line profiles that arise when the two different computational methods are applied results in variations of the equivalent widths that are less than $\Delta W_\lambda = 8$ mÅ. Thus, we

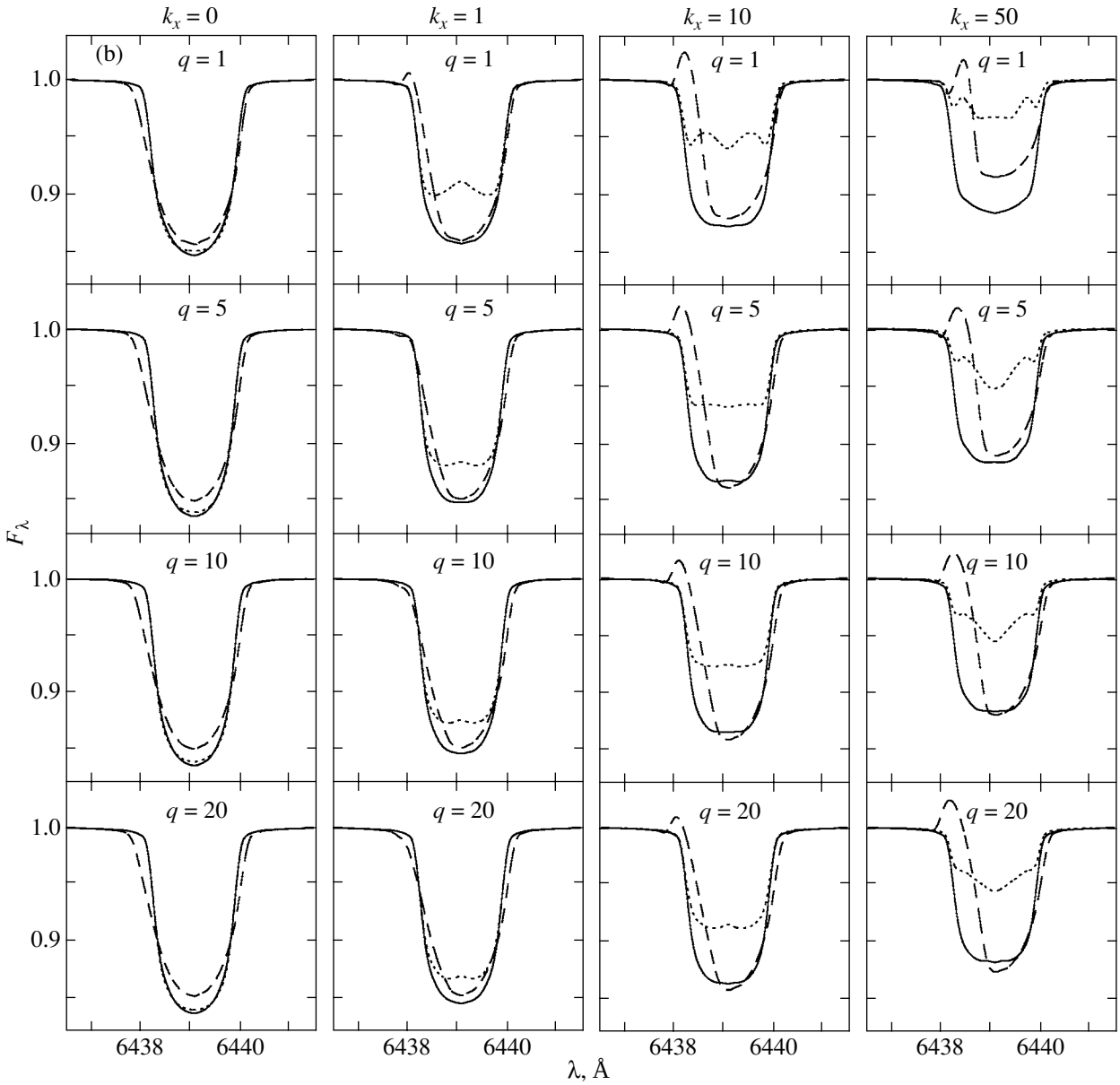

Fig. 3. (Contd.)

conclude that our method is fully adequate for the modeling of irradiated atmospheres.

The specific intensity of the radiation in the computed model atmospheres was found at three main angles θ' (for $\cos\theta' = 0.11, 0.50, 0.89$) by solving the radiative-transfer equation using the Hermitian method. The emission in the direction of the observer was subsequently computed by interpolating between the intensities for the three angles θ' for the real surface-element viewing angle γ. In this way, we physically accurately determined the emitted fluxes taking into account limb darkening using the model atmospheres.

The solution of the radiative-transfer equation included all sources of continuum absorption tabulated in the ATLAS 5 [18], STARDISK [19], and SPECTR [20] software packages, as well as the strongest lines and main molecular bands, according to the theoretical analysis of Nersisyan *et al.* [21]; the line and molecular-band data were derived and kindly provided to us by Ya. Pavlenko (Main Astronomical Observatory of the National Academy of Sciences of Ukraine). When computing the Balmer lines of HI, we applied the theory of Griem [22]; the oscillator strengths for HeI lines were taken from [23, 24], and the corresponding broadening parameters were found using the approximation of Barnard *et al.* [25] and

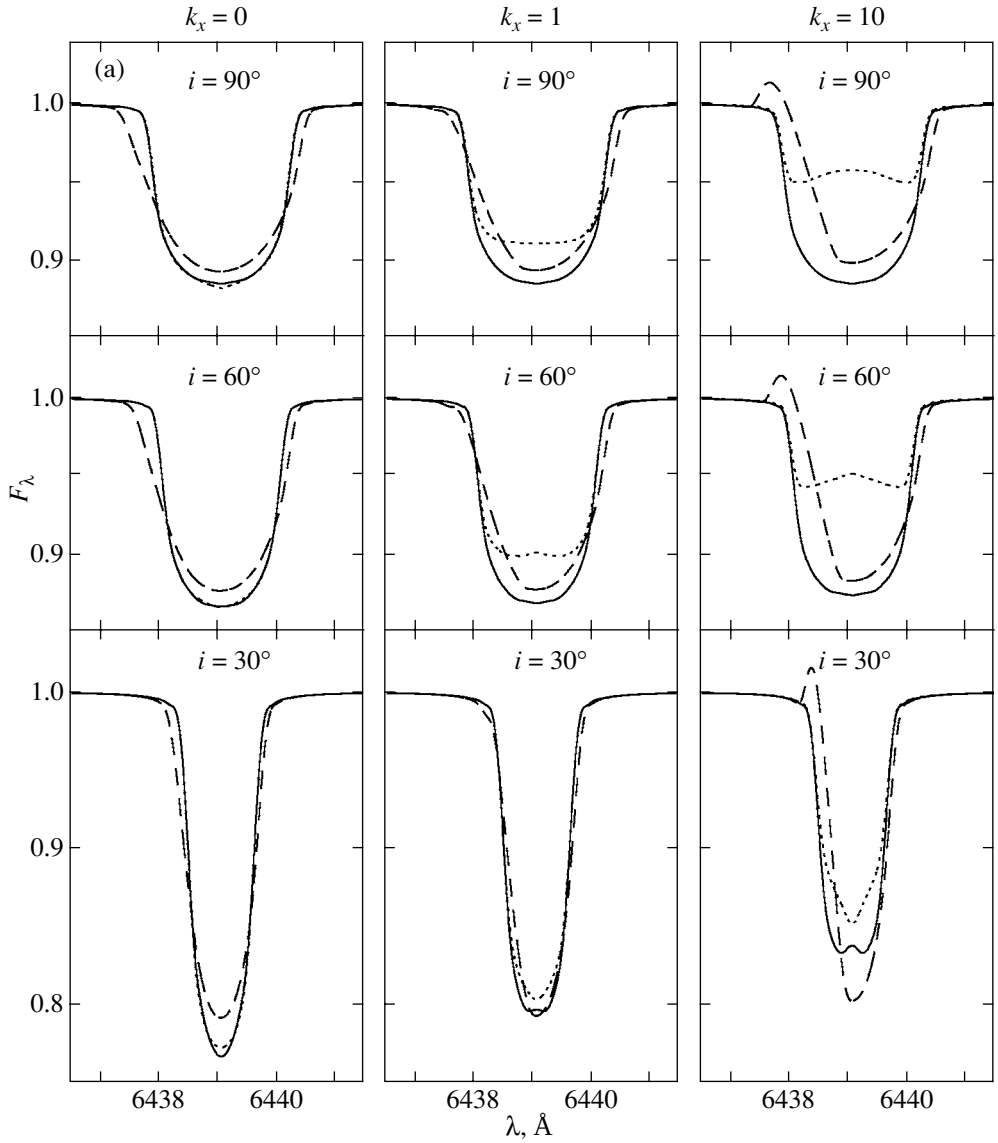

Fig. 4. Dependence of the CaI λ6439 Å line profile on i and k_x for the two orbital inclinations (a) $i = 90°$ and (b) $i = 45°$. The model parameters are $i = 30°-90°$, $k_x = 0-10$, $q = 10$, $\mu_v = 1$, and $T = 5000$ K. Profiles are shown for orbital phases $\varphi = 0$ (solid), 0.25 (dashed), and 0.5 (dotted).

Mihalas *et al*. [26]. The oscillator strengths for lines of heavy elements were taken from Kurucz [11], the van der Waals broadening constants C_6 were found using the classical formula of Unsold [27] with the scaling factor $\Delta \log C_6 = 0.7$, and the Stark broadening constants C_4 were found using the approximation of Kurucz and Furenlid [28]. All the line-profile computations took into account Doppler broadening due to thermal motions and microturbulence (which was assumed constant with $\xi_{turb} = 1.5$ km/s), as well as natural damping, and assumed the solar chemical abundance given in [29].

4. MODELING OF THE THEORETICAL SPECTRAL-LINE PROFILES FOR THE OPTICAL STAR IN AN X-RAY SYSTEM

Let us list the main input parameters for the synthesis of theoretical line profiles for a close binary system containing an optical star and a pointlike compact object that is a source of X-ray emission. The masses of the optical star M_v and X-ray source M_x and the orbital period are given in absolute units. The other input parameters are the Roche-lobe filling factor μ_v, mean effective temperature of the star T (without allowance for heating), ratio of the X-ray luminosity of the compact object and the bolomet-

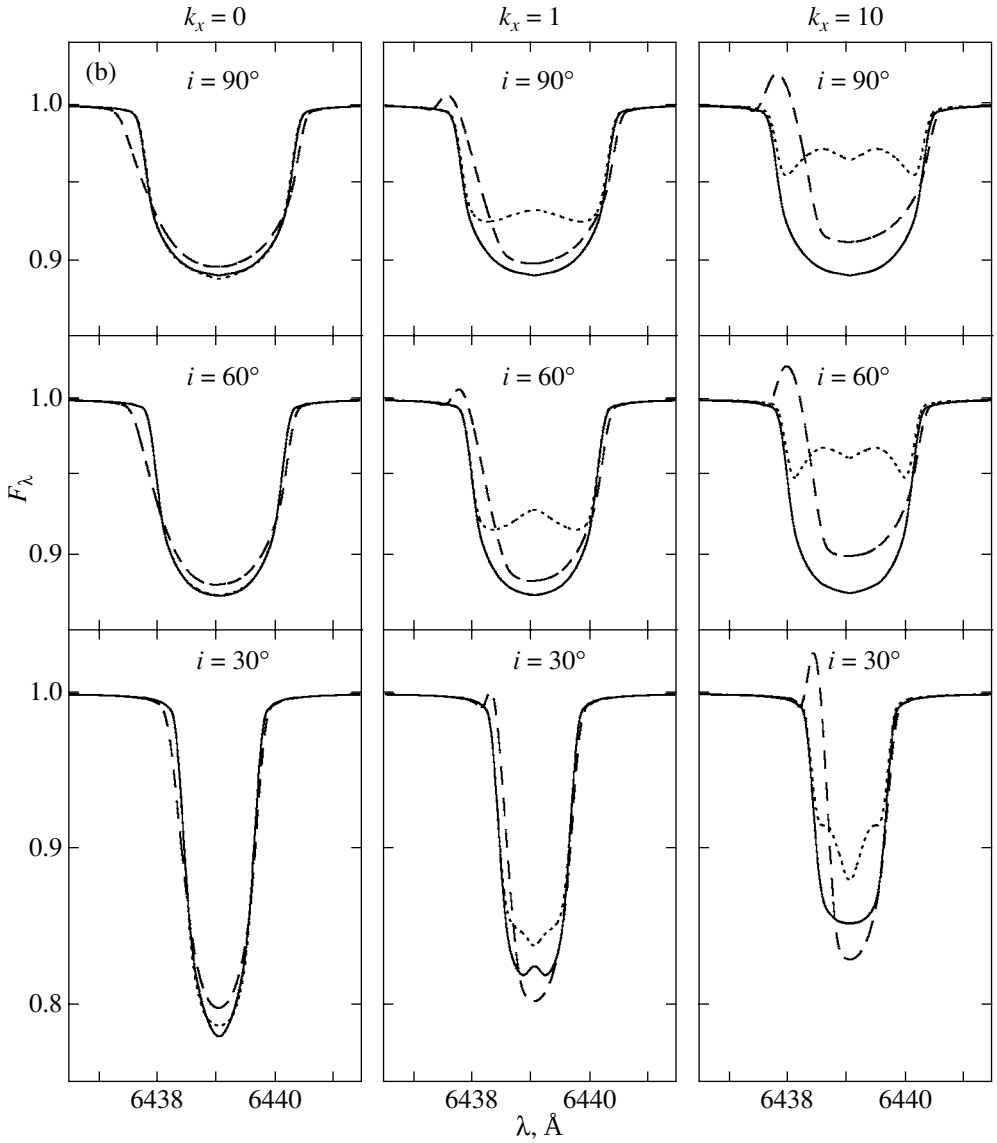

Fig. 4. (Contd.)

ric luminosity of the normal star k_x, gravitational-darkening coefficient β, orbital inclination i, orbital eccentricity e, longitude of periastron ω, and degree of asynchronous rotation F. The data on spectral lines and the spectrum of the compact object are also used as input data.

We selected input parameters that were close to the parameters of low-mass X-ray novae to model the theoretical line profiles. The mass $M_v = 1M_\odot$ and temperature $T = 5000$ K of the optical star were kept fixed. The gravitational-darkening coefficient was assigned the value $\beta = 0.08$ (standard for stars with convective envelopes). The stellar rotation was assumed to be synchronous with the orbital revolution ($F = 1$), and the orbit to be circular. The orbital period was taken to be $P = 5^{\rm d}$ ($P = 12^{\rm d}$ for the computation of the radial-velocity curves). The spectrum of the external compact object in the wavelength range 12–0.5 Å (photon energies of 1–20 keV) was given by the function

$$I_x(\nu) = I_x \nu^{-0.6}. \qquad (21)$$

We studied the behavior of the line profiles of the optical star during the orbital motion for various powers of the incident X-ray flux k_x. The component-mass ratio $q = M_x/M_v$, Roche-lobe filling factor μ_v, and orbital inclination i were varied as well. Theoretical profiles were computed for the CaI λ6439.075 Å absorption line. We did not include non-LTE effects when modeling this line for a star with $T = 5000$ K. In their recent study of the formation of lines of heavy elements in the spectra of X-ray-irradiated cool stars,

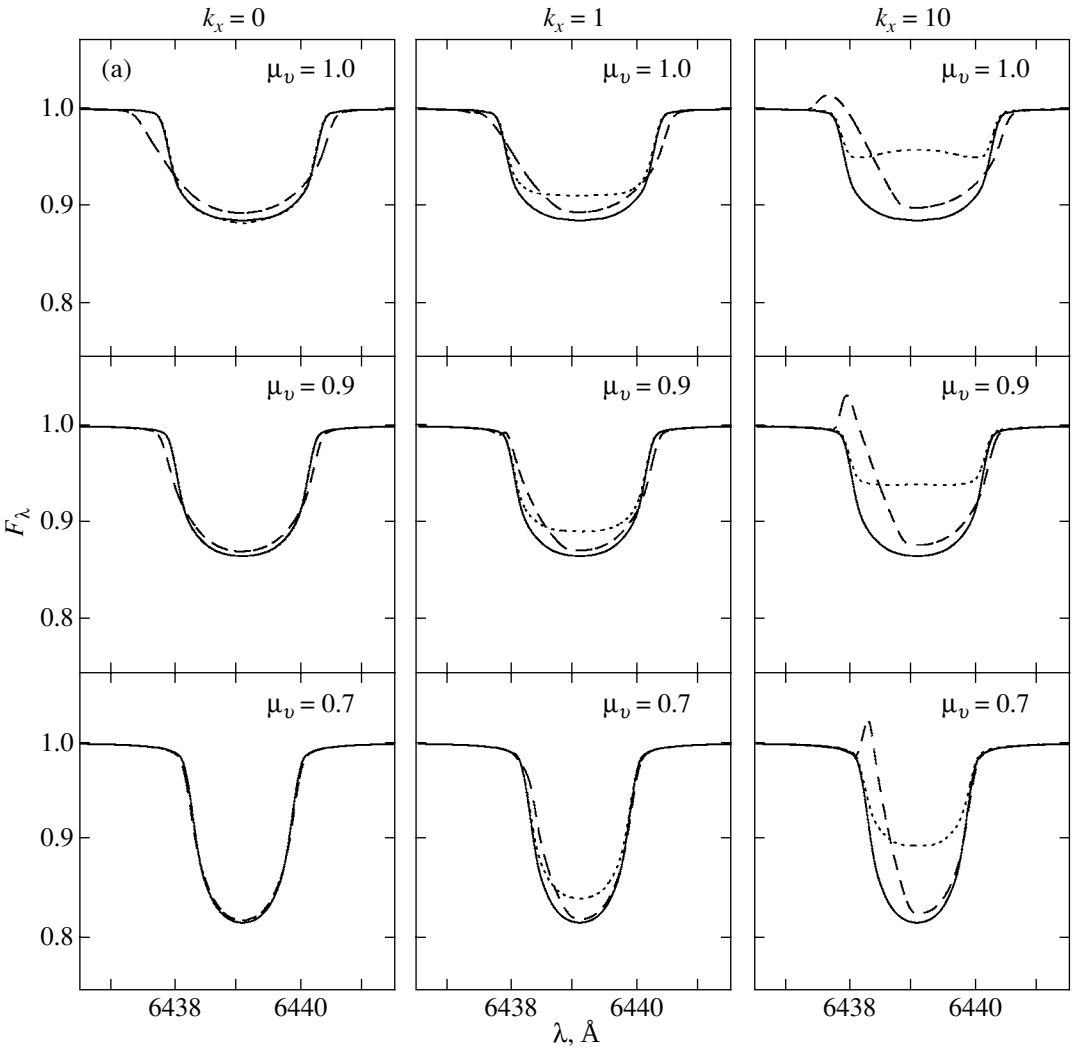

Fig. 5. Dependence of the CaI λ6439 Å line profiles on μ_υ and k_x for the two orbital inclinations (a) $i = 90°$ and (b) $i = 45°$. The model parameters are $\mu_\upsilon = 0.7–1.0$, $k_x = 0–10$, and $q = 10$. Profiles are shown for orbital phases $\varphi = 0$ (solid), 0.25 (dashed), and 0.5 (dotted).

Sakhibullin and Shimanskii [30] showed that non-LTE effects do appear in the atmospheres of such cool stars, but, although the numerical parameters change by 10–20%, the results obtained assuming LTE remain qualitatively correct.

Figure 2 shows the variations of the shape and intensity of the line profile with orbital phase for $k_x = 10$ and $i = 45°$ and 90° using a dense grid in phase. We can clearly see the evolution of the summed line profile of the optical star as it turns the X-ray-heated side toward the observer. At phase 0, the optical star is in front of the X-ray source, and the unheated portion of the surface of the optical star is observed. Starting from about $\varphi = 0.1$, we begin to see the part of the star that is heated by external radiation. At $\varphi = 0.25$ (quadrature), the size of the star in the frontal plane is maximum, and both unheated and heated parts of the star are observed. At phase 0.5, the part of the star that is maximally heated by the incident X-ray radiation is fully turned toward the observer. As the phase increases from 0 to 0.5, an emission component of the profile forms in the region of the star heated by the incident radiation, becoming increasing prominent in the summed line profile. After phase 0.5, the contribution of the emission feature begins to diminish. The line profiles are symmetric about phase $\varphi = 0.5$. At orbital phases when both heated and unheated regions of the star moving with different velocities can be observed, the absorption profile becomes narrower due to the formation of the emission component.

We emphasize that, in the case of a pure ellipticity effect for an optical star without X-ray heating, the width of the line increases at quadrature, when the

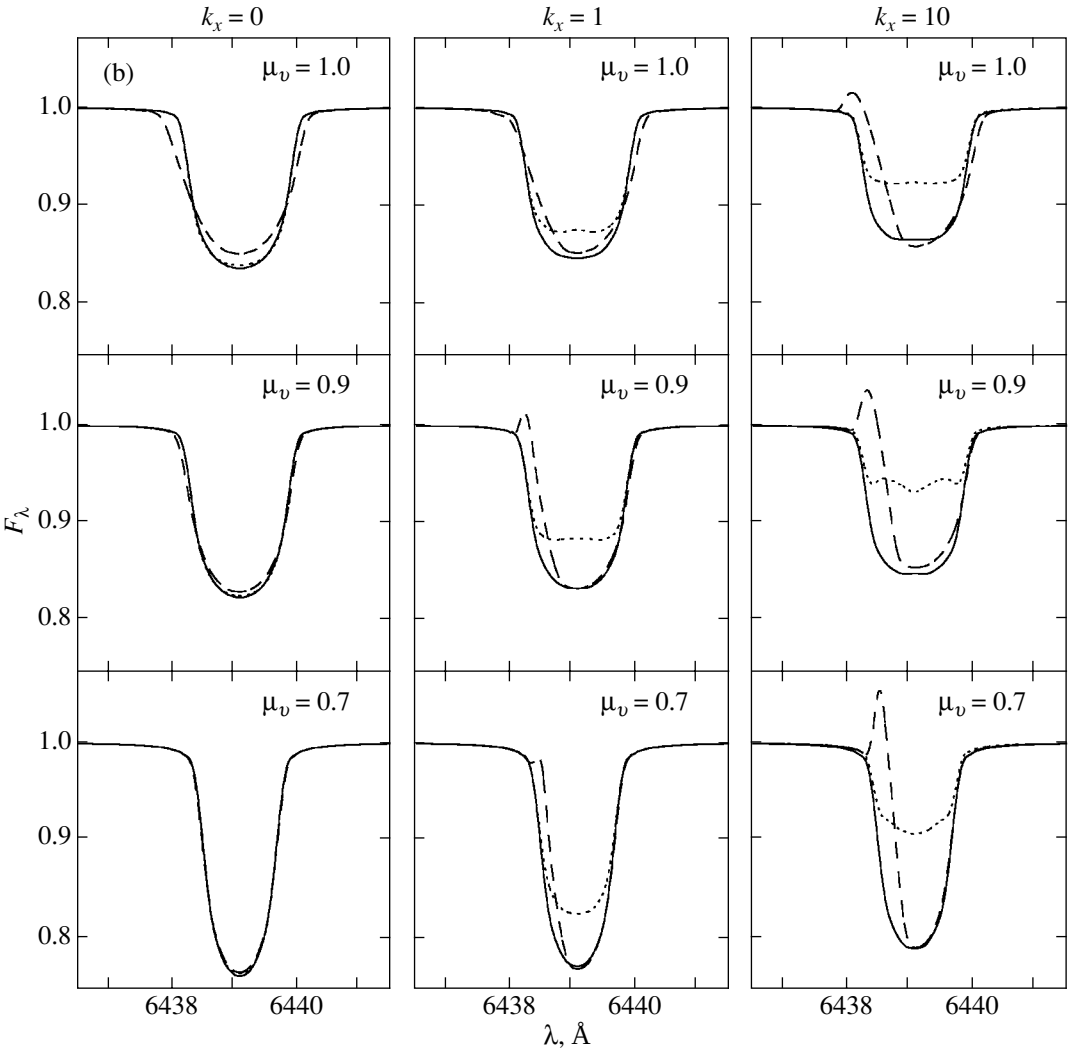

Fig. 5. (Contd.)

star is viewed from the side, since it has its maximum extent along the line connecting the component centers. The X-ray heating results in a more complex temperature distribution over the stellar surface and more complex orbital variability of the line profile due to the formation of the emission component. As a result, if the relative luminosity of the X-ray source is significant, the line profile becomes narrow rather than broader at quadrature.

The line profiles plotted in Fig. 2 show that the behavior of the line is similar for $q = 1$ and $q = 10$, but the depth of the profile increases when q is increased. The emission component of the profile remains fairly prominent when the orbital inclination is decreased from $i = 90°$ (Fig. 2a) to $i = 45°$ (Fig. 2b).

Figures 3–5 show the dependence of the line profiles on the binary parameters q, i, and μ_υ and the parameter k_x characterizing the power of the incident X-ray flux.

The dependence of the theoretical profiles on $q = M_x/M_\upsilon$ and k_x is shown in Fig. 3. The component-mass ratio was varied from 1 to 20, and the value of k_x from 0 (no X-ray heating) to 50 (very strong X-ray heating). The star completely filled its Roche lobe ($\mu_\upsilon = 1$). The orbital inclination was specified to be $i = 90°$ (Fig. 3a) or $i = 45°$ (Fig. 3b). For each set of parameters, the figures show line profiles for three typical orbital phases: $\varphi = 0$ (when the X-ray source is behind the optical star), $\varphi = 0.25$ (quadrature), and $\varphi = 0.5$ (the X-ray source is in front of the optical star). Similarly, Figs. 4 and 5 show line profiles for other sets of system parameters.

The plots in Fig. 3 show that, in the absence of X-ray heating, the width of the absorption profile is nearly the same for different q values, decreasing only very slightly when q is increased from 1 to 20. The increased contribution of the emission component when the X-ray heating is increased from $k_x = 0$ to

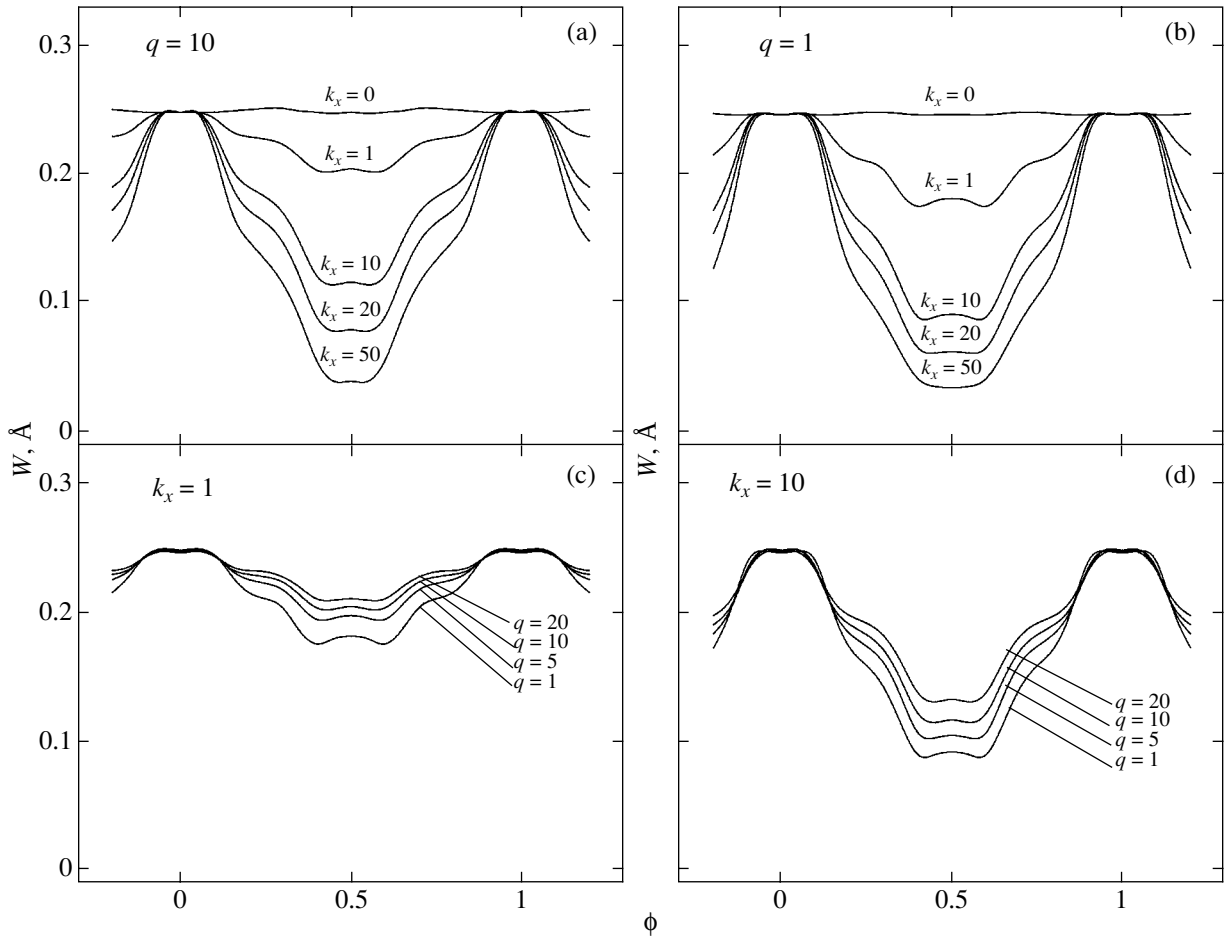

Fig. 6. Orbital-phase variations of the equivalent widths of the CaI λ6439 Å line in the spectrum of the optical star for (a) $k_x = 0{-}50$, $q = 10$, $\mu_v = 1$, and $i = 90°$; (b) the same but with $q = 1$; (c) $q = M_x/M_v = 1{-}20$, $k_x = 1$, $\mu_v = 1$, and $i = 90°$; (d) the same but with $k_x = 10$; (e) $\mu_v = 0.7{-}1$, $k_x = 1$, $q = 10$, and $i = 90°$; (f) the same but with $k_x = 10$; (g) $i = 30°, 60°, 90°$ with $k_x = 1$, $q = 10$, and $\mu_v = 1$; (h) the same but with $k_x = 10$. The temperature of all the models is $T = 5000$ K.

$k_x = 50$ with q constant is clearly visible. The emission component is more prominent for lower q, k_x being the same. This effect is already clearly visible when $k_x = 1$ (compare the profiles for $q = 1$ and $q = 20$); the effect first becomes more pronounced as k_x is increased ($k_x = 10{-}20$), but then weakens. When the X-ray heating is very strong ($k_x = 50$), the differences between the profiles for different q values are small.

Figure 4 shows the dependence of the line profiles on the power of the X-ray heating ($k_x = 0, 1, 10$) and the orbital inclination ($i = 30°, 60°, 90°$). Computations were carried out for the two component-mass ratios $q = 10$ (Fig. 4a) and $q = 1$ (Fig. 4b). We draw the following main conclusions: (1) the width of the profile increases and the depth decreases with increasing i; (2) the profiles vary with orbital phase more strongly when i is larger; (3) the emission component of the line profile that forms as the X-ray heating becomes more powerful is appreciable even at low orbital inclination $i = 30°$; (4) the profiles vary more with orbital phase for $q = 1$ than for $q = 10$, i being the same.

Figure 5 shows the dependence of the line profiles on the size of the star (defined by the Roche-lobe filling coefficient). The rotation of the star is assumed to be synchronous with the orbital motion for both $\mu_v = 1$ and $\mu_v < 1$. Theoretical line profiles are shown for $\mu_v = 0.7, 0.9, 1$ and $k_x = 0, 1, 10$. The data for $i = 90°$ are plotted in Fig. 5a, and those for $i = 45°$ in Fig. 5b. The component-mass ratio was fixed at $q = 10$. We draw the following conclusions: (1) the variability with orbital phase becomes more pronounced when the X-ray heating is increased for all values of μ_v from 0.7 to 1; (2) the profiles become broader when μ_v is increased (due to the increase in the size of the star and, accordingly, the increase in the velocity dispersion at the stellar surface); (3) the

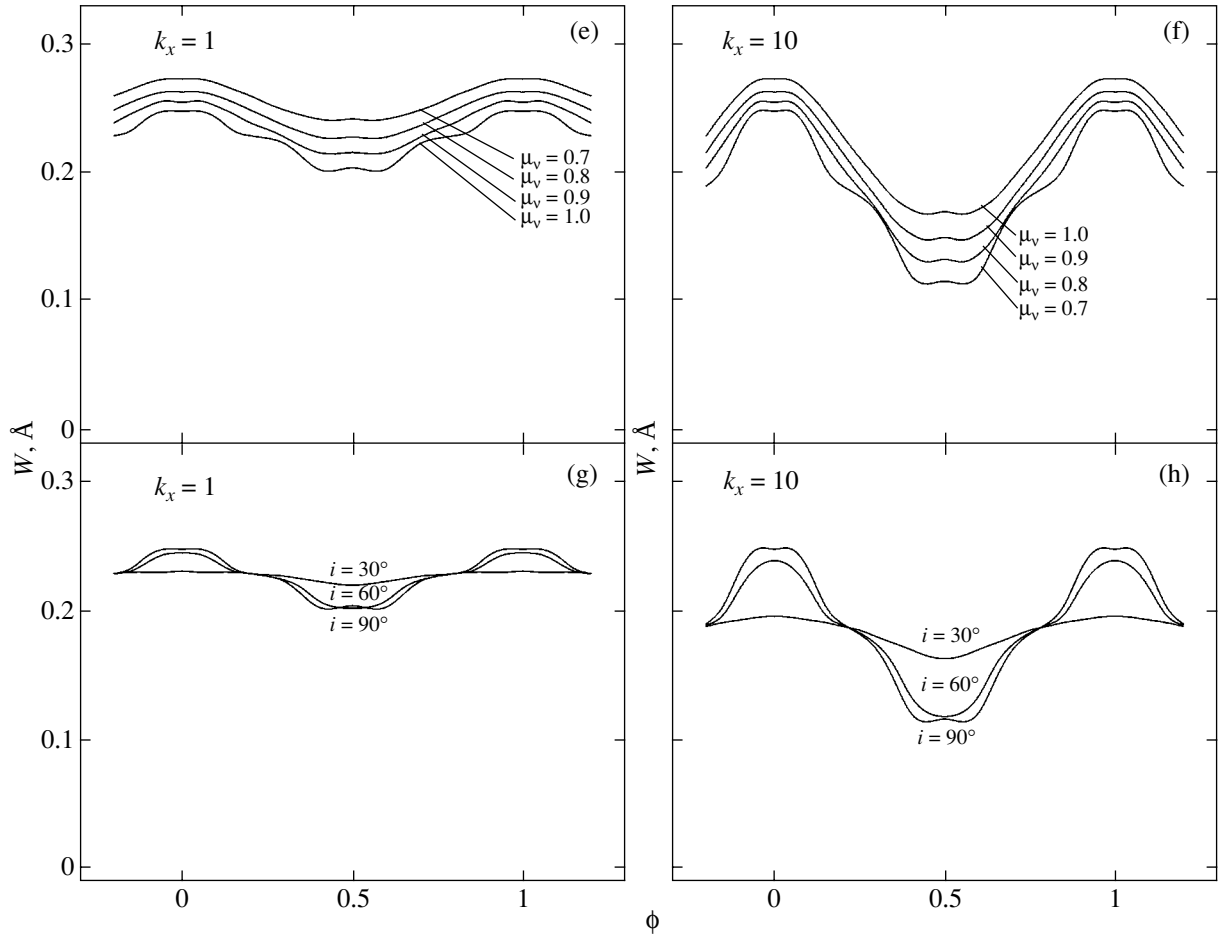

Fig. 6. (Contd.)

intensity of the emission component is higher when the star does not fully fill its Roche lobe. This last effect is due to the relative increase of the fraction of the stellar surface that is heated by the incident X-rays when k_x is constant and μ_v decreases; therefore, the contribution of the heated part of the star to the total radiation increases.

Thus, our modeling of the theoretical CaI λ6439 Å line profiles for various parameters of an X-ray binary system leads to the following main conclusions.

(1) X-ray heating of an optical star with temperature $T = 5000$ K gives rise to an emission component in the CaI λ6439 Å absorption profile. The line profile varies with orbital phase. The intensity of the emission component is higher and its variability with orbital phase more pronounced in the presence of more powerful X-ray heating.

(2) We obtain the following dependence on q. The value of k_x being the same, the emission component is stronger when q is low if the X-ray heating is weak or moderate. In the case of very strong X-ray heating, the differences between the profiles for different q values are small.

(3) We obtain the following dependence on i. The intensity of the emission component becomes higher and its variability with orbital phase more pronounced when the orbital inclination i is increased. The emission component is clearly visible even for small inclinations, $i \sim 30°$.

(4) We obtain the following dependence on the Roche-lobe filling coefficient μ_v. The value of k_x being the same, a star that does not fully fill its Roche lobe has a stronger emission component than a star that fills its Roche lobe.

Note that the theoretical CaI λ6439 Å line profiles were not corrected for the instrumental profile of the detector. The detection of differences between profiles in real spectrograms requires a dispersion of $\sim$0.1 Å per pixel; i.e., a resolution of $R \sim 50\,000$. Spectra with such resolution for 20^m stars (typical for an X-ray nova in quiescence) can be obtained only using the largest (8–10 m diameter) telescopes. However, the

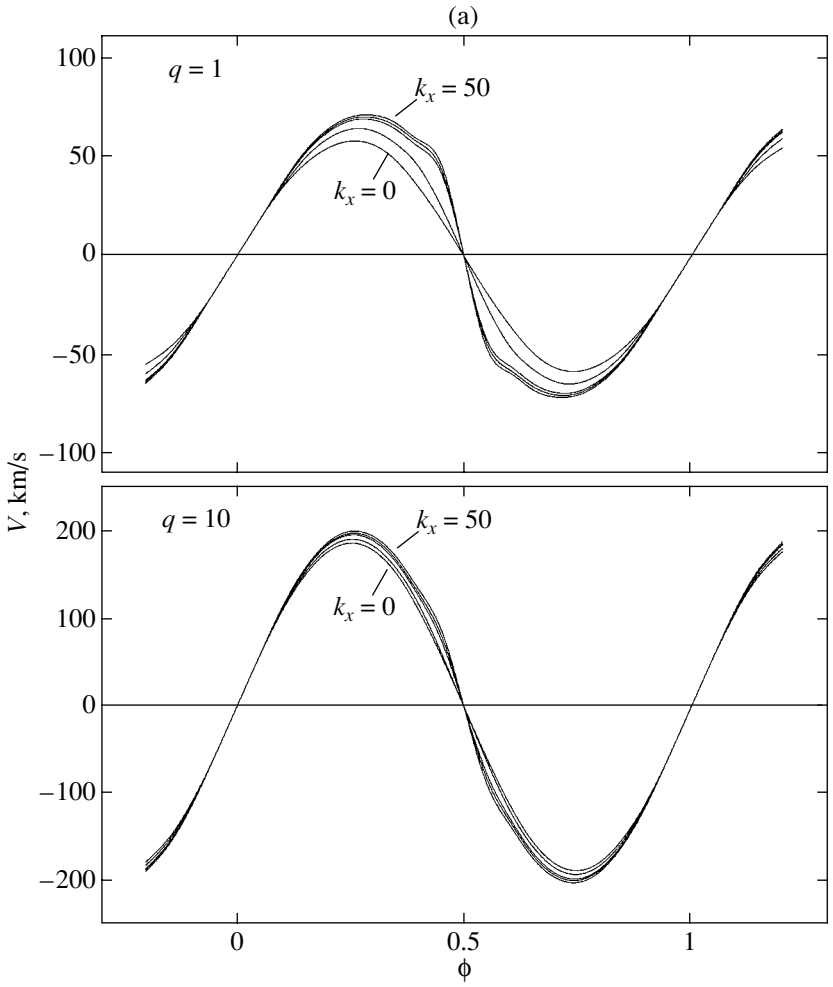

Fig. 7. Dependence of the (a) radial-velocity curves of the optical star and (b) equivalent widths of the CaI λ6439 Å line on orbital phase for $k_x = 0, 1, 10, 20, 50$. Data are shown for the two component-mass ratios $q = 1$ and 10. The amplitude of the radial velocity increases with increasing k_x. The model parameters are $q = 10$, $\mu_v = 1$, $T = 5000$ K, $i = 90°$, and $P = 12^{\rm d}$.

line equivalent widths do not depend on the instrumental profile (only the problem of line blending remains), so the analysis of equivalent widths is possible using lower resolutions of at least $R \sim 10\,000$.

Figure 6 shows the variations of the equivalent width of the CaI λ6439 Å line with orbital phase for various parameters of the X-ray system. The equivalent widths were computed for the entire theoretical profile, including the emission component. The variations of the equivalent widths with the power of the X-ray source ($k_x = 0{-}50$) are plotted for the two component-mass ratios $q = 10$ (Fig. 6a) and $q = 1$ (Fig. 6b). As we already noted above, when q is low, the variability of the line with orbital phase is stronger in the case of weak heating ($k_x = 1$). As k_x is increased, this effect becomes less pronounced, and the orbital variability of the profile is virtually identical for low and high q when the heating is very strong ($k_x = 50$).

The variations of the equivalent widths with the component-mass ratio (for $q = 1{-}20$) are shown for weak ($k_x = 1$) and strong ($k_x = 10$) X-ray heating in Figs. 6c and 6d, respectively. The orbital variability substantially increases in the case of strong heating, and is also higher for lower q.

The differences between the line equivalent widths for different Roche-lobe filling factors μ_v are shown in Fig. 6e for $k_x = 1$ and Fig. 6f for $k_x = 10$. The equivalent widths are larger for smaller μ_v, but the μ_v dependence of the amplitude of their variability relative to the values at phase 0 is weaker.

The dependences of the variability of the line equivalent widths on the orbital inclination ($i = 30°{-}90°$) are shown in Fig. 6g ($k_x = 1$) and Fig. 6h ($k_x = 10$). Variability is present for $i = 30°$, and becomes substantially stronger with increasing i.

The radial-velocity curves as functions of the X-ray heating power k_x are shown in Fig. 7a (for

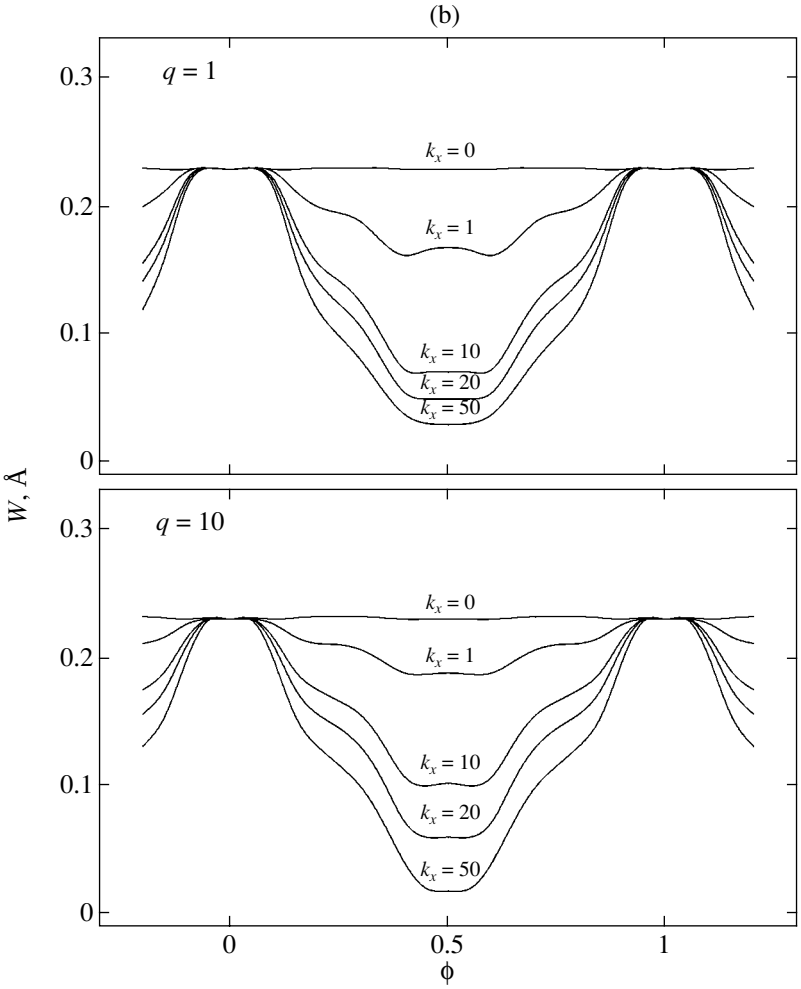

Fig. 7. (Contd.)

$q = 1$ in the upper panel and $q = 10$ in the lower panel). The curves were computed for the CaI λ6439.075 Å line. Figure 7b shows the corresponding variations of the line equivalent widths with orbital phase. The radial velocities were derived as is described in [4] (using three levels: one-third, one-half, and two-thirds of the depth at the line center). The amplitude of the radial velocity grows with k_x, with this effect being more pronounced for $q = 1$ than for $q = 10$.

The growth of the radial-velocity amplitude with k_x is related to the formation of the emission component in the profile. Emission arises in surface elements on the heated side of the star; i.e., in the region with lower radial velocities. Effectively, the absorption profile narrows and the apparent radial velocity increases. The effect is more pronounced for low q (lower masses of the relativistic companion), since the distance between the relativistic object and the surface of the optical star is then lower, so that a relatively larger fraction of the emitted X-ray flux irradiates the surface of the optical star.

Figure 8 shows a three-dimensional plot of the wavelength and orbital-phase dependence of the intensity in the line profile for $k_x = 10$ and $q = 10$. Half of the orbital period is shown. A comparison of this theoretical dependence with the corresponding observed three-dimensional dependence can be used to determine the most important parameters of a close binary: the component masses and orbital inclination.

5. CONCLUSION

Our method for computing absorption-line profiles for X-ray systems, taking into account heating of the stellar atmosphere by external radiation, can be applied to detailed analyses of high-resolution spectra of X-ray binaries. This provides additional opportunities for the reliable estimation of the physical parameters of X-ray binaries, first and foremost, the

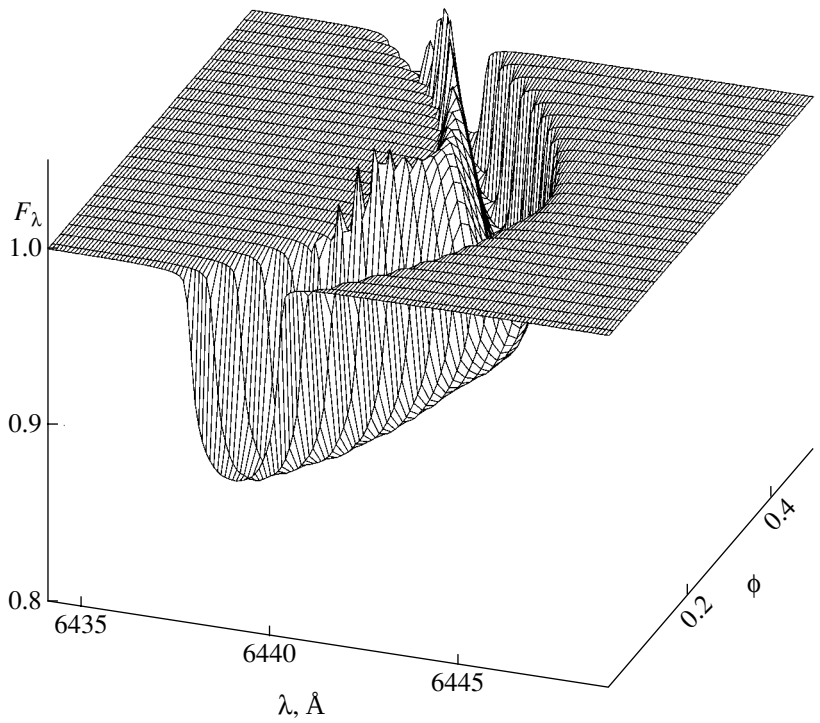

Fig. 8. Three-dimensional dependence of the distribution of the intensity in the CaIλ6439 Å profile on wavelength and orbital phase for $k_x = 10$, $M_v = 1M_\odot$, $M_x = 10M_\odot$, $\mu_v = 1$, $T = 5000$ K, and $i = 90^\circ$.

masses of neutron stars and black holes in such binaries. The realization of these possibilities requires high-resolution ($R \approx 50\,000$) optical spectra of X-ray binaries using modern, large, new-generation telescopes. We hope that applying our method to the interpretation of such spectra will make it possible to obtain more precise estimates of the masses of relativistic objects and reduce the errors in these masses. This is important for verifying the existence of a bimodal distribution for the masses of neutron stars and black holes [31], which is important both for our understanding of the late stages of the evolution of massive stars and the physics of the core collapse in such stars and for testing modern theories of gravitation [32].

ACKNOWLEDGMENTS

This work was supported by the Russian Foundation for Basic Research (project nos. 02-02-17524 and 02-02-17174) and the Program of Support for Leading Scientific Schools of Russia (grants NSh-388.2003.2, and NSh-1789.2003.2). E.A.A. is grateful to Prof. G. Brown for providing the possibility to use computer facilities at Glasgow University (United Kingdom).

REFERENCES

1. E. A. Antokhina and A. M. Cherepashchuk, Pis'ma Astron. Zh. **23**, 889 (1997) [Astron. Lett. **23**, 773 (1997)].
2. T. Shahbaz, Mon. Not. R. Astron. Soc. **298**, 153 (1998).
3. M. K. Abubekerov, E. A. Antokhina, and A. M. Cherepashchuk, Astron. Zh. **81**, 606 (2004) [Astron. Rep. **48**, 550 (2004)].
4. E. A. Antokhina and A. M. Cherepashchuk, Astron. Zh. **71**, 420 (1994) [Astron. Rep. **38**, 367 (1994)].
5. E. A. Antokhina, Astron. Zh. **73**, 532 (1996) [Astron. Rep. **40**, 483 (1996)].
6. R. L. Kurucz, Astrophys. J., Suppl. Ser. **40**, 1 (1979).
7. E. A. Antokhina, A. M. Cherepashchuk, and V. V. Shimanskii, Izv. Akad. Nauk, Ser. Fiz. **67**, 293 (2003).
8. R. E. Wilson, Astrophys. J. **234**, 1034 (1979).
9. H. Von. Zeipel, Mon. Not. R. Astron. Soc. **84**, 684 (1924).
10. L. B. Lucy, Z. Astrophys. **65**, 89 (1967).
11. R. L. Kurucz, SAO CD-ROMs, Cambridge, MA02138, USA (1994).
12. N. A. Sakhibullin and V. V. Shimanskii, Astron. Zh. **73**, 73 (1996) [Astron. Rep. **40**, 62 (1996)].
13. M. Milgrom, Astrophys. J. **206**, 869 (1976).
14. N. A. Sakhibullin and V. V. Shimanskii, Astron. Zh. **73**, 793 (1996) [Astron. Rep. **40**, 723 (1996)].
15. D. G. Yakovlev, L. M. Band, M. B. Trzhaskovskaya, *et al.*, Astron. Astrophys. **237**, 267 (1990).

16. D. V. Ivanova, N. A. Sakhibullin, and V. V. Shimanskii, Astron. Zh. **79**, 433 (2002) [Astron. Rep. **46**, 390 (2002)].
17. V. F. Suleimanov, Pis'ma Astron. Zh. **22**, 107 (1996) [Astron. Lett. **22**, 92 (1996)].
18. R. L. Kurucz, SAO Spec. Rep. **309**, 1 (1970).
19. V. F. Suleymanov, Astron. Astrophys. Trans. **2**, 197 (1992).
20. N. A. Sakhibullin and V. V. Shimanskii, Astron. Zh. **74**, 432 (1997) [Astron. Rep. **41**, 378 (1997)].
21. S. E. Nersisyan, A. V. Shavrina, and A. A. Yaremchuk, Astrofizika **30**, 247 (1989) [Astrophys. **30**, 247 (1989)].
22. H. R. Griem, Astrophys. J. **132**, 883 (1960).
23. M. J. Seaton, C. J. Zeippen, J. A. Tully, *et al.*, Rev. Mex. Astron. Astrofis. **23**, 19 (1992).
24. A. A. Radtsig and B. M. Smirnov, *Atom and Atom Ions Parameters* (Énergoatomizdat, Moscow, 1986) [in Russian].
25. A. J. Barnard, J. Cooper, and L. J. Shamey, Astron. Astrophys. **1**, 28 (1969).
26. D. Mihalas, A. J. Barnard, J. Cooper, *et al.*, Astrophys. J. **190**, 315 (1974).
27. A. Unsold, *Physik der Sternatmospheren* (Springer, Berlin–Gottingen–Heidelberg, 1955).
28. R. L. Kurucz and I. Furenlid, Sample Spectral Atlas for Sirius. SAO Spec. Rep. **387**, 1 (1979).
29. E. Anders and N. Grevesse, Geochim. Cosmochim. Acta **53**, 197 (1989).
30. D. V. Ivanova, N. A. Sakhibullin, and V. V. Shimanskii, Astron. Zh. **81**, 523 (2004).
31. A. M. Cherepashchuk, Usp. Fiz. Nauk **173**, 345 (2003) [Phys. Usp. **46**, 325 (2003)].
32. K. A. Postnov and A. M. Cherepashchuk, Astron. Zh. **80**, 1075 (2003) [Astron. Rep. **47**, 989 (2003)].

Translated by L. Yungel'son

Astronomy Reports, Vol. 49, No. 2, 2005, pp. 127–133. Translated from Astronomicheskiĭ Zhurnal, Vol. 82, No. 2, 2005, pp. 149–156.

Limits on the Flux of Ultrahigh-Energy Neutrinos from Radio Astronomical Observations

A. R. Beresnyak[1], R. D. Dagkesamanskiĭ[1], I. M. Zheleznykh[2], A. V. Kovalenko[1], and V. V. Oreshko[1]

[1] *Pushchino Radio Astronomy Observatory, Astro Space Center, Lebedev Physical Institute, Leninskiĭ pr. 53, Moscow, 117924 Russia*

[2] *Nuclear Research Institute, Moscow, Russia*

Received May 25, 2004; in final form, September 20, 2004

Abstract—We discuss results from current experiments and prospects for future experiments aimed at detecting cosmic ultra-high-energy hadrons and neutrinos using radio astronomical methods proposed earlier by Dagkesamanskiĭ and Zheleznykh. The target for the hadrons and neutrinos is the Moon, and the experiments are designed to detect nanosecond flashes of radio emission from electromagnetic and hadronic cascades produced by high-energy particles in the lunar soil (regolith) using the largest available radio telescopes. We present the results of numerical simulations of the generation of such radio impulses in neutrino reactions, taking into account the requirements for the emergence of the radio emission from the lunar soil. These simulations enable us to correctly relate the detection rate for the radio impulses to the flux of ultra-high-energy neutrinos. The results of the first searches for nanosecond radio flares from the Moon using the 64-m Kalyazin Radio Astronomical Observatory of the Astro Space Center are reported. Experimental limits on the diffuse flux of cosmic neutrinos with energies exceeding 10^{20} eV obtained from these and similar observations carried out in the USA using 70-m and 34-m radio telescopes are compared with theoretical predictions of the neutrino flux for various astrophysical models. Enhancing the sensitivity of such experiments and increasing their duration, especially monitoring the Moon simultaneously with several radio telescopes, could provide important results about the nature of ultra-high-energy cosmic rays in the relatively near future. © *2005 Pleiades Publishing, Inc.*

1. INTRODUCTION

The generation of cosmic rays with high and very high energies is associated with phenomena such as supernovae, gamma-ray bursts, active processes occurring near massive black holes in galactic nuclei, and the decay of relic supermassive particles and/or cosmic strings. These phenomena predict various fluxes of ultra-high-energy (UHE) neutrinos, whose detection would provide an important test of models for the evolution of the Universe.

Results obtained over the last two decades using large-scale detectors of broad air showers, such as Fly's Eye, AGASA, and the Yakutsk installation, have made it possible to collect a database on UHE cosmic rays. For example, the AGASA group has reported 57 broad air showers with energies exceeding 4×10^{19} eV and 8 broad air showers with $E > 10^{20}$ eV [1]. The unexpectedly high flux of protons (and/or heavy nuclei) with energies exceeding the threshold energy for cosmic rays determined by the GKZ effect, $\approx 5 \times 10^{19}$ eV) [2, 3], raises the question of the possible existence of "local" sources of UHE cosmic rays located near the Earth on cosmological scales. The point here is that nucleons with $E > 5 \times 10^{19}$ eV lose energy in processes involving the photocreation of pions when they are scattered on the microwave background radiation (their characteristic mean-free path is $\sim$10 Mpc), while heavy nuclei with such energy will fracture over distances of several Mpc when they are scattered on the microwave background photons. These processes accordingly limit the distances to possible sources of protons and nuclei with extremely high energies ($R < 50-100$ Mpc). In this situation, it is obvious that any experimental evidence for cosmic neutrinos with energies $E > 5 \times 10^{19}$ eV would be of considerable interest, since these particles can arrive at the Earth from arbitrarily large distances; the fluxes of such neutrinos are predicted to exceed the flux of protons by one to two orders of magnitude in a number of models, such as the top–down model [4].

However, studies of the spectrum of cosmic neutrinos with energies up to and even exceeding 10^{20} eV require detectors with target volumes of hundreds or thousands of cubic kilometers (with masses of $10^{11}-10^{12}$ t). The construction of neutrino telescopes on such scales based on the principles of "classical"

1063-7729/05/4902-0127$26.00

optical neutrino telescopes is a complicated and very expensive technical task.

The development of alternative radio-wavelength (radio astronomical) methods for detecting neutrinos with energies 10^{14}–10^{20} eV and higher, and the construction of radio-wavelength (radio astronomical) neutrino telescopes with target masses of 10^9–10^{12} tons, represents one possible way to progress in experimental studies in UHE-neutrino astrophysics [5, 6].

2. A RADIO ASTRONOMICAL METHOD FOR THE DETECTION OF UHE NEUTRINOS

At the beginning of the 1960s, Askar'yan [7, 8] considered the development of an electromagnetic cascade produced by a high-energy particle in a dense medium (dielectric). He showed that, due to the appearance of recoil electrons via Compton processes, the scattering of electrons and positrons on atomic electrons, and annihilations arising in cascades of positrons, the excess of negatively charged particles (electrons) is about 20% of the total number of charged particles, which in turn is proportional to the cascade energy. A pulse of radio emission should be observed in directions close to the Cherenkov angle; this emission will obviously be coherent right to frequencies of the order of $\nu_{max} = c/d$, where c is the speed of light and d is the characteristic transverse size of the cascade (the Askar'yan effect). The coherence of the radio emission due to the "excess" electrons is disrupted at frequencies above ν_{max}.

In 1983, Gusev and Zheleznykh [6] proposed to use large volumes of Antarctic ice as a neutrino target, to attempt to detect radio emission from hadronic and electromagnetic cascades (the Askar'yan effect) producing neutrinos in the ice (the RAMAND project; see also [9]). It was proposed to detect the cascade radio emission using antennas placed on the surface of the ice over an area of ~ 1 km^2. Taking into account the directivity of the Cherenkov emission, such a detector could be used to study interactions between the ice and cosmic neutrinos arriving from the lower hemisphere.

For a cascade in ice, the transverse size d is approximately 10 cm and the frequency ν_{max} is several GHz. Thus, the corresponding Cherenkov radiation is produced at centimeter and short-wave decimeter radio wavelengths. Thanks to the high transparency of the cold Antarctic ice to radio emission at these wavelengths, the effective volume of the target of a RAMAND-type neutrino telescope comprised of a relatively modest number of antennas is of the order of a cubic kilometer for neutrino energies above 10^{14} eV. Preliminary experiments were carried out at the "Vostok" Antarctic station in 1985–1990 by the Nuclear Physics Institute of the Russian Academy of Sciences and the Arctic and Antarctic Scientific Research Institute (St. Petersburg). These studies of the background conditions for the RAMAND and other neutrino telescopes using detectors comprised of three and seven antennas showed that the radio detection of neutrinos in Antarctica was a promising direction of high-energy neutrino astronomy [10, 11]. The financing of the RAMAND project was suspended in the early 1990s after the breakup of the USSR.

Currently, the radio detection of neutrinos in Antarctica is actively being developed by two American projects: RICE [12], with antennas located in chinks on the Amundsen–Scott station, and ANITA [13], with antennas mounted on a balloon, whose flight around the South Pole at an altitude of 40 km is planned for 2006. It has also been proposed to use the Moon as a target for the detection of UHE neutrinos, using the largest available radio telescopes as the detectors [5, 14, 15]. The authors of these studies argue that the fact that the number of particles in a cascade N is proportional to the energy of the primary cosmic particle E_ν and the coherence of the radio emission is proportional to N^2 should appreciably compensate for the large distance of the detectors from the target, and the cosmic scale of the target compensate for the decrease in the particle flux with increasing energy.

However, it is not easy to distinguish short and very rare flashes of radio emission from cascades due to the background noise of the detection apparatus. This task becomes even more complex due to the presence of various types of interference. These problems were considered in [5, 14, 15]. It was recommended to use multichannel receivers with broad bandwidths and a coincidence scheme to enhance the fluctuation sensitivity of the detectors, and to use the characteristic "coloring" of the signal as a result of its passage through the Earth's ionosphere as a means of distinguishing the signal against the background of interference. The dispersional delay of the radio signal in the ionosphere leads to a relative delay in the flashes in the low-frequency compared to the high-frequency channels, which should make the desired signal differ appreciably from the overwhelming majority of local interference. Calculations carried out in the referenced studies showed that, in principle, the sensitivity of already existing large radio telescopes should be sufficient to detect particles with energies of the order of 10^{20} eV using this technique. At the same time, it is easy to understand that realizing this idea required the construction of specialized multichannel equipment, with the initial processing of the signal

carried out in real time so that "suspicious" events could be distinguished. There is no doubt that these very technical difficulties served as one reason why observations of nanosecond flashes from the Moon were not possible at the end of the 1980s and the beginning of the 1990s. However, there was another reason as well: the healthy skepticism of many specialists, who doubted the existence of an appreciable flux of particles with energies of 10^{20} eV or more, and even doubted that the emission mechanism predicted by Askar'yan would operate, and that the parameters of the predicted flashes were estimated sufficiently accurately to search for them.

3. LABORATORY OBSERVATIONS OF THE ASKAR'YAN EFFECT AND THE FIRST ATTEMPTS TO DETECT NANOSECOND RADIO IMPULSES FROM THE MOON

Today, after nearly 15 years, the situation has radically changed. On the one hand, the AGASA results have attracted new attention to the problem of cosmic rays with energies exceeding 10^{20} eV; the neutrino flux measured at either this or lower energies could prove critical for testing many models for possible sources of such particles. On the other hand, accelerator experiments carried out in 2000 confirmed the existence of Cherenkov radio emission from cascades. The most convincing experiment was performed on the Stanford Linear Accelerator (SLAC), and consisted of spraying clumps of high-energy neutral particles—photons—at a target comprised of sand and detecting the resultant radiation [16]. The polarization and spectrum of the radiation and the linear dependence of the amplitude on the total energy of the particle clump corresponded to the values expected for coherent Cherenkov radiation. Thus, the Askar'yan effect was directly confirmed experimentally.

Finally, there have been two attempts to detect UHE neutrinos using radio astronomical methods over the past ten years. The first was undertaken by Hankins *et al.* [17], who observed the Moon using the 64-m Parkes telescope in Australia at 1.4–1.7 GHz over twelve hours. They did not detect a single promising flash with a flux exceeding 4000 Jy, although the use of receivers with broad bandwidths gave these observations a rather high sensitivity. In addition, the continuous measurement of the total electron concentration directly above the observatory made it possible to monitor the dispersion delay between the signals in two frequency channels, and this criterion proved to be very effective at identifying various types of interference. At the same time, the antenna beam was always pointed at the center of the lunar disk, while the accurate estimates of [18–20] have shown that the flashes of emission expected from the interaction of neutrinos with atoms of the lunar regolith should be strongly concentrated toward the limb of the Moon.

The second attempt to detect UHE neutrinos using radio astronomical methods was undertaken with the 70-m and 34-m radio telescopes of the Deep Space Network at Goldstone (USA). The results of the first cycle of such observations were published in [18]. The search for nanosecond flashes of radio emission was carried out at 2.2 GHz. A coincidence scheme was used for the signals received by these two radio telescopes, which are separated by a distance of about 22 km. In addition, to reduce the influence of local interference, a coincidence scheme was implemented, comparing the main signal received by the 70 m radio telescope at 2.2 GHz and the signal received at 1.8 GHz by the same telescope at the same time but 0.5° away from the main beam. In this way, the authors were able to realize a threshold sensitivity of 3000 Jy. No flash with a flux density exceeding this threshold and with the expected parameters of Cherenkov flashes was observed over 30 h of observations near the limb of the Moon [18]. Monitoring by the same group over 120 h likewise did not lead to any detections of Cherenkov flashes [19], although the longer observations made it possible to establish stricter upper limits for the rate of the expected flashes.

4. OBSERVATIONS ON THE 64-m KALYAZIN RADIO TELESCOPE

Our search for radio flashes arising during the interaction of UHE neutrinos with the lunar surface was conducted using the 64-m radio telescope of the Kalyazin Radio Astronomical Observatory of the Astro Space Center of the Lebedev Physical Institute [21]. The receiver system of this fully steerable parabolic reflector is based on a single wide-band horn. This makes it possible to carry out observations at several frequencies within a wide range from 0.6 to 8.3 GHz simultaneously. The observations described here were carried out simultaneously in four frequency channels using radiometers designed for three frequency ranges. 1.4 GHz observations were conducted in two orthogonal circular polarizations (LCP and RCP), while 2.3 GHz observations were carried out only in right-circular polarization (RCP). In addition, to provide additional checking capability, observations were recorded in another channel which obtained the signal from the receiver output at 0.6 GHz (LCP only) or, more rarely, at 4.8 GHz (likewise LCP only). The input low noise amplifiers (LNAs) for the receiver complexes were used in an uncooled regime, since the system noise temperature

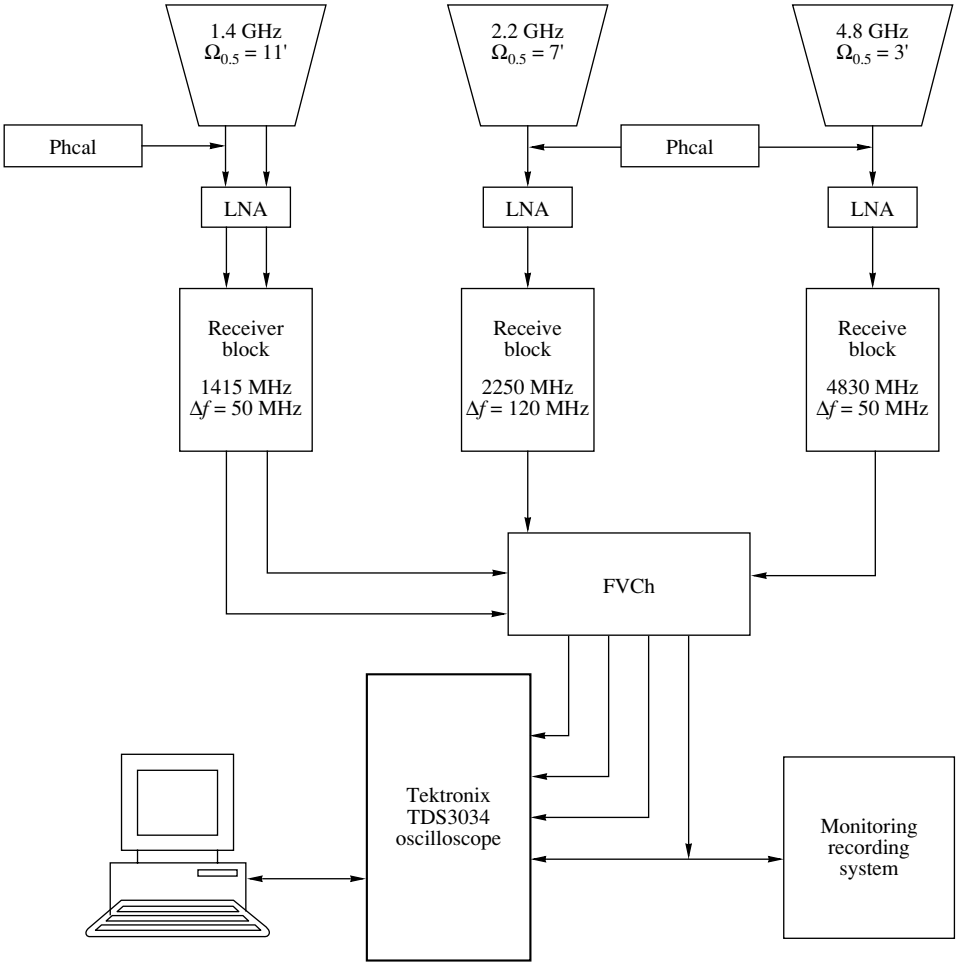

Fig. 1. Scheme for the experiment.

was in any case dominated by the contribution of the radiation of the Moon. The main characteristics of the receiver complexes used for our observations are essentially the received bandwidth and the antenna beam width at a specified frequency. These parameters were 8 MHz and 25′ at 0.6 GHz, 50 MHz and 11′ at 1.4 GHz, 120 MHz and 7′ at 2.3 GHz, and 50 MHz and 3′ at 4.8 GHz. A schematic of the experiment is shown in Fig. 1.

We used a trigger system with a time resolution of 2 ns based on a four-channel Tektronix TDS 3034 digital oscillograph to record the short impulses. This system enabled us to record data for "suspicious" events for subsequent processing and analysis. The electrical axes of the radio telescope, and accordingly the directions of the maxima of the antenna beams, coincided at all four frequencies used; the trigger was set up to operate in the 2.3 GHz channel. The relative differences in the signal propagation times for the different frequencies were measured using a source of pico-second pulses whose signal was sent to the input of the LNAs. The trigger was set up in one channel, and operated if the voltage corresponding to the received signal in this channel exceeded a specified level. During the entire set of observations, the radio telescope was pointed at a point shifted 14′ in elevation from the center of the lunar disk.

The power of the received signal was calibrated via comparison with the response of the radio telescope to the powerful radio source Cygnus A, whose flux density is accurately known at all four frequencies used. The effective time constant of the receiver system was determined using a recording of impulsive signals from a compact source suitable for use as an interferometric phase calibrator (a so-called PhCal source). Note that the responses to the most powerful broadband interference indicated approximately the same time constant.

The trigger level during the observations corresponded in most recordings to a 2.3 GHz flux density of $S_{2.3} \approx 13\,500$ Jy (somewhat lower in some cases). The total pure observation time, corresponding to the waiting time of the oscillograph between triggers, was 31.3 h. The indicated trigger level was chosen as a

compromise, since lowering this level would have led to an appreciable decrease in the efficiency of using the observing time; i.e., to a decrease in the ratio of the pure to the total observational time. "Suspicious" events recorded during the observations were subsequently analyzed for (a) the presence or absence of an impulse in one of the 1.4 GHz channels and its delay relative to the impulse in the 2.3 GHz trigger channel; (b) clustering of triggers due to periodic interference; (c) the shape of the impulse in both channels; and (d) the difference between the impulses in the LCP and RCP channels at 1.4 GHz (since the desired signal should be 100% linearly polarized, these two signals should be the same). As a result of this secondary data reduction, all the "suspicious" events were rejected; i.e., none of the roughly 15 000 recorded events satisfied all these criteria. In most cases, the system was triggered by a series of local interference spikes, with one trigger following another in a small time interval.

5. ESTIMATE OF THE DIFFUSE NEUTRINO FLUX

The spectral power of coherent Cherenkov radiation due to an excess negative charge in a shower neglecting its transverse structure (the so-called one-dimensional approximation) can be written using the Franck–Tamm formula for a finite track [22] modified for the smoothly varying charge density along the shower [20, 23, 24]. More detailed modeling of showers carried out by several independent groups (see, for example, [24, 25]) using Monte Carlo simulations and scaling demonstrates the expected disruption of the coherence between different parts of the cascade at high frequencies. The characteristic coherence-disruption frequency for cascades in the lunar regolith is about 3 GHz.

Due to the growth in the lepton–nucleon interaction cross section expected in most nucleon models and confirmed in experiments on $(e-p)$ scattering, the Moon becomes effectively opaque to neutrinos of the energies considered; the collision length becomes about 70 km for an energy of 10^{21} eV [26].

An interaction via a charged flow ($W^{\pm}$) yields a charged lepton, which, in the case of an electron, gives rise to an electromagnetic shower and a recoil quark, which, in turn, produces a hadronic shower. Because the energy in the hadronic shower is rapidly divided among many particles, it is much less subject to the Landau–Pomeranchuk–Migdal (LPM) effect [27–30]. Thus, a shower from a charged flow can consist of two showers with different longitudinal structures: a comparatively short hadronic shower and a strongly elongated, fluctuating electromagnetic shower that is subject to the LPM effect. The simulations of [20] showed that, although, in many cases, a smaller fraction of the energy of the neutrino goes into the hadronic shower, its role from the point of view of detection is more important, since its Cherenkov peak is broader than that of the electromagnetic shower. An interaction via a neutral flow (Z^0), for which the cross section is approximately a factor of 2.4 smaller, yields only a hadronic shower, with most of the energy usually carried away by the lepton (neutrino).

The material of the lunar surface—the regolith—is relatively transparent to radio waves. The characteristic capture length is about 10 m for radiation at 1 GHz, and is inversely proportional to the frequency. Due to the absorption of neutrinos, nearly all neutrinos arriving from beneath the surface and reaching the upper 10 m of the surface layer travel at small angles to the surface. Since the Cherenkov angle is complementary to the angle for total internal reflection, this strongly suppresses the escape of the radiation, while also leading to an appreciable stretching of the initial solid angle of the radiation due to refraction at angles close to the angle for total internal reflection. The simulations showed that, due to the finite width of the Cherenkov peak, there will also be a small number of events associated with neutrinos penetrating into the regolith in the immediate vicinity of the point where the Cherenkov flash emerges [20]. Thus, it becomes clear from a geometrical consideration that a large fraction of the radio impulses arriving at an observer on Earth will come from regions close to the lunar limb. The suppression of the impulse amplitude and the geometrical selection effect described above lead to the conclusion that the initial estimates of the effective volume of the target made in [5] were too optimistic.

We wrote a program to carry out Monte Carlo simulations of our neutrino experiment, incorporating all available information about the creation of showers and the refraction and detection of the radio pulse. We considered refracted, but not scattered, pulses, since only the former retain the subnanosecond duration and the regular structure of the primary Cherenkov impulse. We also allowed for the fact that the lunar surface can have a random inclination relative to an ideal sphere, with the dispersion in the inclination angle being about 6°. This modeling enabled us to estimate the effective volume of the detector and its dependence on the neutrino energy, as well as the effective aperture.

Together with the fact that no events that could plausibly be interpreted as Cherenkov flashes from cascades were detected in our experiment, the modeling results can be used to derive an upper limit for the flux of UHE neutrinos. If we aim to derive rigorous conclusions, we should adopt a specific slope for the neutrino energy spectrum in the energy interval of

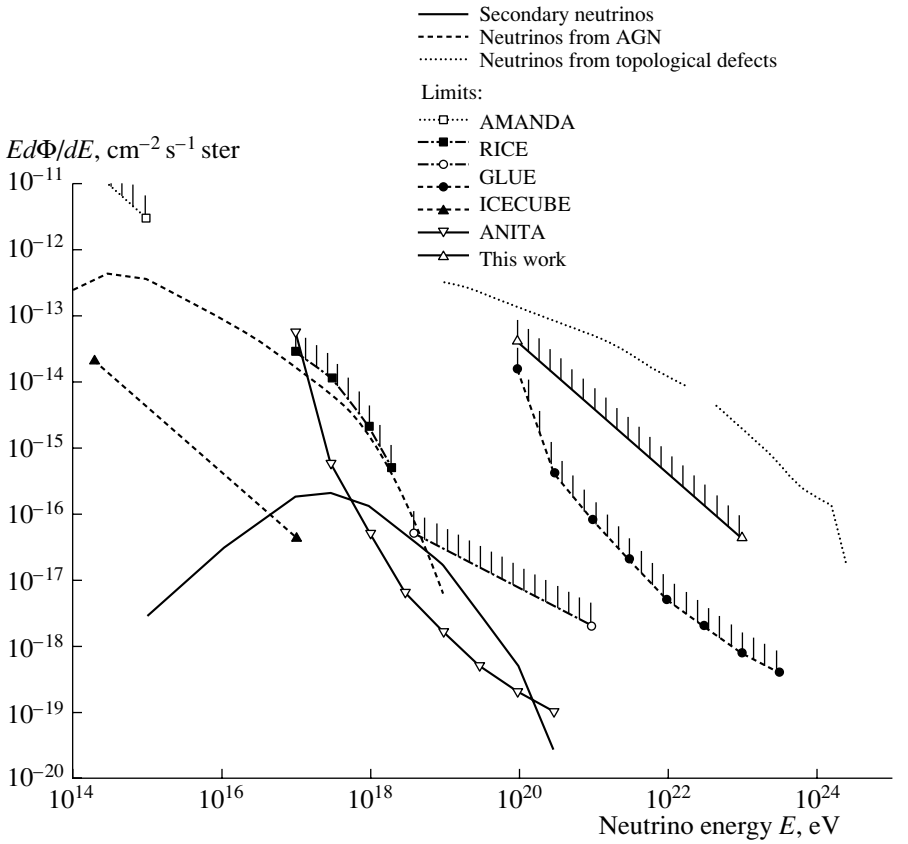

Fig. 2. Theoretically predicted flux of UHE neutrinos and experimentally derived limits on this flux.

interest to us and an isotropic angular distribution for the neutrinos.

Our and other experiments are currently able to exclude only models with the largest UHE-neutrino fluxes. One popular set of such models proposes that the decay of massive relic particles or strings determine the spectrum of both neutrinos and cosmic rays above the GZK cutoff. In this case, the expected neutrino flux should be appreciably higher than the cosmic-ray flux [31]. Such models yield an approximately power-law spectrum with an index close to $n = -2$ right up to the maximum energy, which is determined by the mass of the primary particles involved. Therefore, this model predicts a power-law spectrum with index -2 in the energy interval 10^{20}–10^{23} eV. A spectrum of this type, shown in Fig. 2, can be ruled out at the 95% confidence level based on our observations. For comparison, this same figure shows various theoretical spectra for proposed neutrino sources, as well as the upper limits on the UHE-neutrino flux presented for various experiments in the literature, including the GLUE experiment [19].

6. DISCUSSION AND CONCLUSION

Thus, our observations have given another limit on the flux of UHE neutrinos. The difference between our estimate and the estimate obtained in the GLUE experiment is due, not so much to the different sensitivities of the two experiments, as to the different models used to interpret the direct observational results. Indeed, even the effective target volume (or aperture) depends strongly on the adopted model for the distribution of the inclination angles for the real lunar surface to an ideal sphere. For example, in models with purely refracted impulses, the effective target volume grows by more than an order of magnitude as the dispersion of the inclination-angle distribution grows from 0 to 10° [20]. In addition, it is known that the dispersion of the distribution of inclination angles of the real surface to an ideal spherical surface will be appreciably different in different regions of the Moon; for example, a region with a large number of craters will have a higher inclination-angle dispersion. In our experiment, the position of the beam on the Moon at any time during the observations was known rather accurately. However, the difficulty in taking into account the effect discussed here is that no estimates are available for the dispersion of the inclination angles for regions close to the limb.

Models with partially scattered impulses [19] suffer from an even larger uncertainty, since they require knowledge of the small-scale structure of the surface.

In addition, calculation of the shape and spectrum of the scattered impulse present certain difficulties. The disagreement between the estimates of the effective volume used in [19, 20] are rather large, and require serious consideration. However, the fact that many of the uncertainties that we have discussed have a methodical character provides hope that experiments in the near future can be designed and interpreted in a more correct and consistent fashion. At the same time, possible ways to enhance the sensitivity of radio astronomy observations aimed at detecting UHE particles are already known. Our experiment would be considerably improved by the use of a logical coincidence scheme for the events recorded in two or more channels, which would make it possible to appreciably lower the trigger level. Finally, increasing the total duration of the observations represents another way to increase their overall sensitivity.

If we consider this question in a broader context, the use of several medium-size antennas in such observations is a promising possibility. This would enable a substantial enhancement of the target volume while preserving, or even increasing, the sensitivity (due to the use of a larger number of antennas), since it would then be possible to record flashes from the entire lunar limb, rather than only a small segment of the limb, as was done in the experiments described above. Overall, observations using an array of relatively small telescopes would in many ways be ideal for a lunar neutrino experiment. The antennas could operate either in a coincident mode or as a multi-beam synthesized beam covering the entire lunar limb. Finally, conducting simultaneous observations using several well separated antennas in an array would sharply reduce the number of false events due to local interference, and also provide additional information about the arrival direction of any UHE particles detected.

ACKNOWLEDGMENTS

This work was supported by the Russian Foundation for Basic Research (project no. 02-02-17229), the program of the Presidium of the Russian Academy of Sciences "Nonstationary Phenomena in Astrophysics," and the State Science and Technology Program in Astronomy.

REFERENCES

1. AGASA Collaboration, Astropart. Phys. **19**, 447 (2003).
2. K. Greisen, Phys. Rev. Lett. **16**, 748 (1966).
3. G. T. Zatsepin and V. A. Kuzmin, Pis'ma Zh. Éksp. Teor. Fiz. **4**, 114 (1966) [JETP Lett. **4**, 78 (1966)].
4. G. Sigl, Ann. Phys. **303**, 117 (2003); astro-ph/0210049.
5. R. D. Dagkesamanskii and I. M. Zheleznykh, Pis'ma Zh. Éksp. Teor. Fiz. **50**, 233 (1989) [JETP Lett. **50**, 259 (1989)].
6. G. A. Gusev and I. M. Zheleznykh, Pis'ma Zh. Éksp. Teor. Fiz. **38**, 505 (1983) [JETP Lett. **38**, 611 (1983)].
7. G. A. Askar'yan, Zh. Éksp. Teor. Fiz. **41**, 616 (1961) [Sov. Phys. JETP **14**, 441 (1961)].
8. G. A. Askar'yan, Zh. Éksp. Teor. Fiz. **48**, 988 (1965) [Sov. Phys. JETP **21**, 701 (1965)].
9. M. A. Markov and I. M. Zheleznykh, Nucl Instrum. Methods Phys. Res. A **248**, 242 (1986).
10. A. L. Provorov (for the RAMAND Collaboration), in *Proc. 3rd Int. Workshop on Neutrino Telescopes*, Ed. by Milla Baldo Ceolin (Venice, 1991), p. 337.
11. A. L. Provorov and I. M. Zheleznykh, Astropart. Phys. **4**, 55 (1995).
12. I. Kravchenko *et al.* (RICE Collaboration), Astropart. Phys. **20**, 195 (2003).
13. S. W. Barwick *et al.*, Proc. SPIE **4858**, 265 (2003).
14. I. M. Zheleznykh, *Proc. 13th Intl. Conf. Neutrino Physics and Astrophysics, 1988*, p. 528.
15. R. D. Dagkesamanskii and I. M. Zheleznykh, *Astrophysical Aspects of the Most Energetic Cosmic Rays*, Ed. by M. Nagano and F. Takahara (World Scientific, Singapore, 1992), p. 373.
16. D. Saltzberg, P. W. Gorham, *et al.*, Phys. Rev. Lett. **86**, 2802 (2001).
17. T. H. Hankins, R. D. Ekers, and J. D.O'Sullivan, Mon. Not. R. Astron. Soc. **283**, 1027 (1996).
18. P. W. Gorham *et al.*, Proc. RADHEP-2000 (2001), p. 177.
19. P. W. Gorham, C. L. Hebert, K. M. Liewer, *et al.*, astro-ph/0310232; Phys. Rev Lett. (in press).
20. A. Beresnyak, astro-ph/0310295; Astron. Astrophys. (in press).
21. Yu. P. Ilyasov, B. A. Poperechenko, and V. V. Oreshko, Tr. Fiz. Inst. im. P.N. Lebedeva, Akad. Nauk **229**, 44 (2000).
22. I. E. Tamm, J. Phys. (Moscow) **1**, 439 (1939).
23. E. Zas, F. Halzen, and T. Stanev, Phys. Rev. D **45**, 362 (1992).
24. J. Alvarez-Muniz, R. A. Vazquez, and E. Zas, Phys. Rev. D **62**, 063001 (2000).
25. S. Razzaque, S. Seunarine, D. Z. Besson, D. W. McKay, J. P. Ralston, and D. Seckel, Phys. Rev. D **65**, 103002 (2002).
26. R. Gandhi *et al.*, Phys. Rev. D **58**, 093009 (1998).
27. L. Landau and I. Pomeranchuk, Dokl. Akad. Nauk SSSR **92**, 535 (1953).
28. L. Landau and I. Pomeranchuk, Dokl. Akad. Nauk SSSR **92**, 735 (1953).
29. A. B. Migdal, Phys. Rev. **103**, 1811 (1956).
30. A. B. Migdal, Zh. Éksp. Teor. Fiz. **5**, 527 (1957) [Sov. Phys. JETP **5**, 440 (1957)].
31. S. Yoshida, H. Dai, C. C. H. Jui, and P. Sommers, Astrophys. J. **479**, 547 (1997).

Translated by D. Gabuzda

Astronomy Reports, Vol. 49, No. 2, 2005, pp. 134–143. Translated from Astronomicheskiĭ Zhurnal, Vol. 82, No. 2, 2005, pp. 157–167.

Limits on the Mass of Dark Matter in the Sun from a Model for the Modern Sun and Its Previous Evolution

N. S. Kardashev[1], A. V. Tutukov[2], and A. V. Fedorova[2]

[1] *Astro Space Center, Lebedev Physical Institute, Leninskiĭ pr. 53, Moscow, 117924 Russia*

[2] *Institute of Astronomy, ul. Pyatnitskaya 48, Moscow, 119017 Russia*

Received May 20, 2004; in final form, May 27, 2004

Abstract—The influence of dark gravitating matter on the present-day Sun and its evolution is studied. Numerical simulations show that substantial departures of the main model parameters (luminosity, effective temperature, neutrino flux, and age) from the modern solar parameters would occur if the relative mass of dark matter exceeded 2–5% of the solar gravitational mass. The flux of solar neutrinos is relatively insensitive to the presence of uniformly distributed dark matter. However, a strong concentration of dark matter toward the center of the Sun would increase the neutrino flux beyond the observational limits.

1. INTRODUCTION

Studies of dark matter and its contribution to the evolution of the Universe are of primary importance for astronomy and physics. The first arguments in support of dark matter were presented by Oort [1] in 1932 in connection with the dynamical density in the vicinity of the Sun's Galactic orbit, and by Zwicky [2] in 1937 in connection with the dynamical stability of clusters of galaxies. The estimate obtained in [1] and well known as the Oort limit indicates that the amount of invisible material in the vicinity of the solar system is approximately equal to the amount of visible matter. Zwicky [2] showed that clusters of galaxies would decay over times shorter than the age of the Universe if there were no gravitating matter except for ordinary stars. In fact, there is an almost tenfold increase in the mass-to-luminosity ratio in the transition from galaxies to clusters of galaxies. Later, an increase in the fraction of dark matter with distance from the centers of galaxies was revealed [3]. Massive dark halos or coronas of galaxies, as well as agglomerations of dark matter in the central regions of some galaxies, have been detected in numerous studies [4–8]. It is interesting that most studies of galaxies have associated the excess mass primarily with massive galaxies [9, 10]. In addition, the formation of galaxies requires a considerable amount of nonbaryonic gravitating matter of an unknown nature (dark matter) in order to explain the visible structure of clusters of galaxies [11]. This last consideration probably rules out brown and red dwarfs as possible carriers of dark matter, though the stellar mass function and its relation to star formation remains incompletely understood for stars with masses smaller than a solar mass. A comprehensive analysis of stellar microlensing in the direction of the Large Magellanic Cloud has not indicated any surplus of stellar-mass objects compared to the visible stars [12]. This excludes relict stellar-mass black holes as the origin of the dark matter. Analysis of the microlensing data also rules out compact objects with masses of $(10^{-7}-1)M_\odot$ as possible carriers of dark matter in the Galactic halo [13]. A detailed review of studies of dark matter in the Universe can be found in [14].

Current data on the division of the mean density in the Universe among its various components can be explained by a model in which dark energy (equation of state $p_x = w\rho_x$, where p_x and ρ_x are the pressure and density of the dark energy, respectively, and $w \approx -1$) comprises 70% of the density, "cold" dark matter (equation of state $p = 0$) comprises 25% of the density, and the baryon component, including observable objects (via their electromagnetic radiation), represents about 5% of the density [11, 15–20]. The distribution of the dark energy is probably almost homogeneous.

In turn, the cold dark matter can consist of one or more components, or particles, whose kinetic energy is much lower than the energy corresponding to their rest masses. There have been numerous suggestions about the properties of these particles, though all of them imply a very weak interaction with normal baryonic matter. Possible components of the dark matter include new elementary particles [21–25] whose rest masses range from those of neutrinos to Planck-mass black holes (2×10^{-5} g) or primordial black holes [26, 27] (such particles with masses $> 10^{15}$ g could survive

Hawking evaporation), as well as mirror matter [28–31] (the mirror world provides a complete symmetry between the left and right states of particles, and contains the same set of particles as does our world, but interacts with our world only gravitationally).

It has gradually been elucidated that the matter studied in astronomy probably comprises only 10–20% of the total mass participating in the evolution of the Universe. The nature of the remaining matter remains unknown, except for its gravitational interaction with ordinary matter and its small cross sections for other collisional interactions. The observed increase in the mass-to-luminosity ratio with distance from the centers of galaxies [32] implies that the necessary invisible matter is concentrated primarily in the interstellar media of galaxies and clusters of galaxies. However, some fraction of this matter could be associated with stars, in particular with the Sun.

Hypotheses on the presence of dark matter inside the Sun have been proposed earlier. Periodic pulsations of the solar surface with a period of 159.9660 ± 0.0010 min were revealed via measurements of the wavelengths of spectral lines at the Crimean Astrophysical Observatory in 1974 [33, 34], and were subsequently verified by observations at Stanford University. At a solarphysics meeting in Toulouse in 1978, D.O. Hus proposed that these pulsations could be excited by a planetlike object consisting of dark matter with a mass of $\sim 10^{-7} M_\odot$. Dark matter in the solar system has also been studied (we shall discuss this below in Section 5).

Over the last forty years of intense theoretical studies, the Sun has become a reliable experimental laboratory for verifying a number of physical parameters in the theory of stellar evolution, such as the equation of state, the opacity of the stellar material, and the rates of nuclear reactions (see, for example, [35–38]). The so-called solar-neutrino problem has been solved recently [39]. The nature of the problem was that the detected flux of electron neutrinos emitted in thermonuclear reactions in the solar core was lower by a factor of two to three than the flux predicted by theoretical models of the Sun. The solution was provided by the properties of neutrinos: it was proposed that there were oscillations of neutrinos (transformations of electron neutrinos into tau neutrinos and muon neutrinos) in the solar interior and during the trip from the Sun to the Earth [40]. This hypothesis has been successfully verified. Observations of the Sun using the new generation of neutrino detectors have shown that the total flux of all three types of neutrinos is close to the theoretical flux, namely 7.8 ± 0.6 SNU for a chlorine detector and 120 ± 20 SNU for a gallium detector [39]. (Here and below, the neutrino flux is expressed in commonly used solar neutrino units (SNU); 1 SNU $= 10^{-36}$ neutrino captures per atom of the detector material per second.) This result has demonstrated the trustworthiness of our current theoretical model of the Sun.

The purpose of the current study is to place limits on the presence of invisible matter in the solar interior by estimating the implications for the model of the modern Sun of the gravitation of this matter and the additional energy release associated with it. The main observable parameters used to verify the theory are the radius, luminosity, and age of the Sun, together with the neutrino fluxes measured by gallium and chlorine detectors. An additional parameter of the model is the position of the base of the convective envelope, which has been verified by solar seismology and corresponds to a radius of $R_{conv} = 0.71 \pm 0.01 R_\odot$ [35–37].

2. STANDARD MODEL OF THE SUN

We carried out numerical simulations of the solar evolution using a standard stellar-evolutionary code adjusted during our study using the equation of state and the rates of nuclear reactions in the current standard model of the Sun, together with the observed flux of solar neutrinos [35]. We assume the solar age to be 4.6 billion years, which is close to current estimates [41]. The abundance of heavy elements Z was taken to be 0.02, which is likewise near estimates for the present-day Sun [41]. Since this last quantity is not known precisely [39], we have chosen a certain average value for Z.

To obtain a model for the present-day Sun with the given Z, age, radius, and luminosity, we must chose the free parameters—the initial hydrogen density X and the mixing-length parameter l/H_p (from convection theory). For each set of parameters, we compute the evolution of a solar-mass star, starting from the stage when it is a completely convective protostar on the Hayashi track. The assumed Z and age, together with the selected free parameters, enable us to obtain the observed effective temperature, luminosity, and neutrino flux for the standard solar model, as well as the depth of the convective zone indicated by helioseismology.

Table 1 shows the changes in the solar parameters during the Sun's evolution. Table 2 presents the distribution of the main physical quantities in the model for the present-day Sun.

Our estimates for the flux of solar neutrinos (Table 3), namely 6–7 SNU for chlorine detectors and 102–108 SNU for gallium, do not differ much from other theoretical estimates: 7–8.5 SNU and 123–131 SNU [39]. These fluxes have been verified by observations taking into account neutrino oscillations, demonstrating the trustworthiness of our solar models.

Table 1. Evolution of the solar parameters

t, years	$\log T_{eff}$ (K)	$\log(L/L_\odot)$	$\log(R/R_\odot)$	$\log \rho_c$ (g/cm^3)	$\log T_c$ (K)
6.66×10^4	3.657	0.040	0.231	0.253	6.646
1.79×10^5	3.656	0.025	0.225	0.272	6.652
5.73×10^5	3.655	−0.020	0.205	0.335	6.670
2.14×10^6	3.652	−0.137	0.152	0.530	6.714
5.53×10^6	3.653	−0.261	0.089	0.824	6.772
1.25×10^7	3.672	−0.303	0.030	1.256	6.866
2.05×10^7	3.718	−0.168	0.005	1.658	6.982
2.45×10^7	3.741	−0.085	−0.001	1.788	7.047
2.63×10^7	3.749	−0.062	−0.005	1.824	7.074
2.84×10^7	3.754	−0.064	−0.016	1.851	7.097
3.21×10^7	3.754	−0.107	−0.037	1.868	7.113
4.44×10^7	3.751	−0.151	−0.054	1.872	7.118
9.36×10^7	3.750	−0.154	−0.053	1.871	7.115
2.90×10^8	3.751	−0.148	−0.051	1.877	7.115
5.53×10^8	3.751	−0.141	−0.048	1.888	7.117
1.08×10^9	3.752	−0.125	−0.042	1.913	7.123
2.13×10^9	3.755	−0.092	−0.031	1.969	7.137
4.09×10^9	3.761	−0.019	−0.007	2.092	7.169
4.60×10^9	3.762	0.000	0.000	2.126	7.177

Note: t is the age, $\log T_{eff}$ is the effective temperature, L is the luminosity, and R is the radius of the star, while ρ_c and T_c are the density and temperature at the stellar center.

3. SOLAR MODELS WITH GRAVITATING DARK MATTER

3.1. Distributions of the Dark Matter inside a Star

Here, we assume that the existence of dark matter is manifest only gravitationally, and that dark matter does not contribute to the gas pressure, due to the small cross sections of its collisional interactions. Therefore, the contribution of dark matter to the equation describing the internal stellar structure results in the appearance of a dimensionless coefficient in the standard equation for the mass, radius, and density of the star:

$$dM_r = 4\pi r^2 \rho\, dr(1+\alpha). \quad (1)$$

Here, M_r is the total mass of a sphere with a radius r, ρ is the density of ordinary material corresponding to this radius, and α is the fraction of dark matter in the stellar material at this radius.

We consider four different distributions of dark matter in the star:

(1) the dark matter is distributed uniformly throughout the star and the model uses a single parameter α;

(2) the dark matter is concentrated toward the stellar center, and α decreases linearly toward the surface; the model uses two parameters: the mean parameter α_m and the ratio d of the central α to its mean value;

(3) the dark matter is concentrated toward the stellar surface, and α decreases linearly toward the center, with the model using the same two parameters;

(4) the dark matter is concentrated toward the stellar center and distributed exponentially:

$$\alpha = Ae^{-\beta M_r/M}. \quad (2)$$

Here, M_r is the total mass of a sphere with radius r, M is the total mass of the star, α is the fraction of dark matter in the stellar material at this radius, and β is the index of this distribution. The coefficient A

Table 2. Standard model of the Sun

$M_r/M_\odot$	$\log(r/R_\odot)$	$\log(L_r/L_\odot)$	$\log\rho\,(\mathrm{g/cm^3})$	$\log T\,(\mathrm{K})$	X	∇T	$\log\kappa$	V_{conv}, cm/s
1.000	0.00	0.00	−7.78	3.69	0.697	0.002	−1.58	−
1.000	0.00	0.00	−6.68	3.73	0.697	0.168	−0.58	−
1.000	0.00	0.00	−6.38	3.99	0.697	0.296	1.87	2.28×10^5
1.000	0.00	0.00	−5.20	4.22	0.697	0.127	3.72	8.41×10^4
1.000	0.00	0.00	−3.77	4.51	0.697	0.221	5.04	3.43×10^4
1.000	−0.01	0.00	−2.77	4.98	0.697	0.343	4.49	1.87×10^4
0.999	−0.04	0.00	−1.64	5.68	0.697	0.394	2.48	8.50×10^3
0.970	−0.14	0.00	−0.64	6.34	0.697	0.397	1.39	−
0.961	−0.16	0.00	−0.53	6.41	0.697	0.324	1.25	−
0.959	−0.17	0.00	−0.52	6.42	0.697	0.307	1.23	−
0.921	−0.23	0.00	−0.16	6.53	0.697	0.206	1.02	−
0.725	−0.42	0.00	0.71	6.74	0.696	0.198	0.66	−
0.320	−0.69	−0.03	1.48	6.96	0.673	0.264	0.35	−
0.076	−0.99	−0.34	1.89	7.10	0.532	0.320	0.20	−
0.014	−1.26	−0.96	2.06	7.16	0.404	0.314	0.14	−
0.011	−1.31	−1.08	2.08	7.16	0.391	0.312	0.13	−
0.005	−1.43	−1.43	2.11	7.17	0.365	0.311	0.12	−
0.001	−1.66	−2.08	2.13	7.18	0.350	0.308	0.11	−

Note: M_r is the mass below the radius r, L_r is the luminosity, ρ is the density, T is the temperature, X is the hydrogen density, ∇T is the temperature gradient, κ is the opacity coefficient in $\mathrm{cm^2/g}$, and V_{conv} is the convective velocity in the convective envelope of the Sun.

Table 3. Parameters of the solar models for a linear distribution of dark matter

No.	α	d	X	l/H_p	T_c, 10^7 K	ρ_c, $\mathrm{g/cm^3}$	F(Cl), SNU	F(Ga), SNU	$\log(R/R_\odot)$	$\log(L/L_\odot)$	R_{conv}
1	0.00	−	0.697	1.95	1.505	133.7	6.19	102.3	0.000	0.000	0.721
2	0.02	1.0	0.704	2.55	1.508	134.1	6.49	104.4	0.000	0.000	0.722
3	0.05	1.0	0.714	5.05	1.512	134.7	6.93	107.7	0.001	0.000	0.723
4	0.05	0.5	0.704	10.28	1.511	130.8	6.75	105.7	0.007	−0.002	0.756
5	0.05	1.5	0.724	3.02	1.511	134.8	6.93	108.9	0.000	0.000	0.725
6	0.10	1.0	0.731	20.84	1.509	130.1	6.71	108.3	0.035	−0.012	0.830

Note: No. is the model number, α is the mean fraction of dark matter in the stellar material, d is the ratio of the dark-matter fraction at the stellar center to the mean fraction, X is the initial hydrogen density, l/H_p is the ratio of the mixing length (from convection theory) to the local pressure scale height, T_c and ρ_c are the temperature and density at the stellar center, F(Cl) and F(Ga) are the neutrino fluxes for chlorine and gallium detectors (in SNU), R and L are the radius and luminosity for the corresponding model, and R_{conv} is the radius of the lower boundary of the convective zone.

normalizes the dark matter fraction integrated over the star to its mean value α_m.

Figure 1 shows the dark-matter distributions computed for all the nonstandard models of the modern Sun described below. Distribution (1) is used for models 2, 3, and 6, distribution (3) for model 5, distribution (2) for model 4, and distribution (4) for models 7–11.

3.2. Effects of Dark Matter on the Evolution of a Solar-Mass Star

To demonstrate the effects of dark matter on the evolution of solar-type stars, we first computed tracks

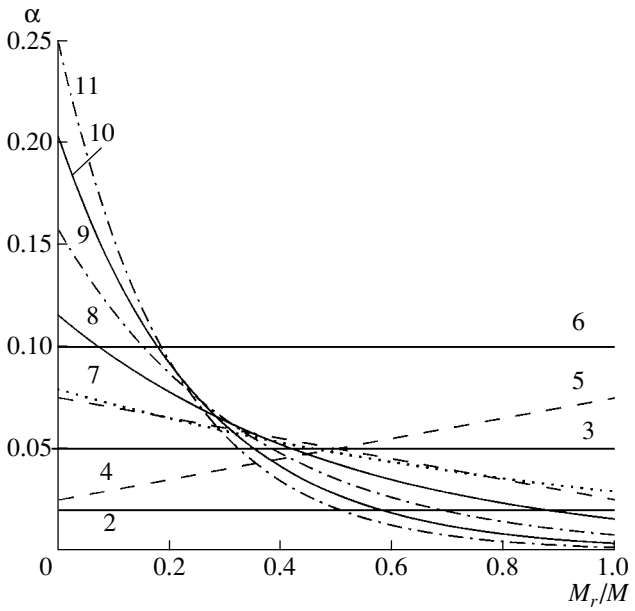

Fig. 1. Distribution of dark matter over the star for the models of the modern Sun containing dark matter, for various fractions α of dark matter inside the star. The model numbers correspond to those in Tables 3–5. In models 2, 3, and 6, the dark matter is homogeneously distributed throughout the star. In models 4 and 5, the distribution is linear with a concentration of dark matter toward the surface and center, respectively. In models 7–11, the distribution is exponential and concentrated toward the center, with the index β equal to 1, 2, 3, 4, and 5, respectively.

for a linear dark-matter distribution and fairly high mean α without initially searching for a model with the parameters of the present-day Sun. The computations started when the protostar was located on the Hayashi boundary and finished when the star reached an age of 4.6 billion years. We took the abundance of heavy elements to be $Z = 0.02$, and used an initial hydrogen abundance of $X = 0.7$ for all the tracks.

We present the results of the computations in Figs. 2 and 3. Figure 2 shows a standard evolutionary track for a solar-mass star and two tracks computed for homogeneous dark-matter distributions with $\alpha = 0.2$ and 0.4. Figure 2 indicates that adding the dark matter significantly shifts the stellar track toward lower effective temperatures and considerably accelerates the star's evolution. We can qualitatively explain this acceleration as an effect of an increase in the luminosity (rate of hydrogen burning) brought about by the decrease in the opacity resulting from the decrease in the abundance of ordinary matter and nuclear energy inside the star. The considerable influence of even a comparatively small amount of dark matter on the models of stars with the solar mass and age is evident.

Figure 3 shows the influence of the dark-matter distribution on the evolution of the Sun when the total fraction of dark matter is $\alpha = 0.2$. The concentration of dark matter toward the center causes the stellar track ($d = 1.9$) to approach the standard track somewhat, since the outer regions of the star experience weaker changes in this case. On the other hand, this concentration significantly accelerates the evolution due to the decrease in the amount of hydrogen in the core, and, therefore, in the opacity of the core material. A concentration of dark matter toward the surface ($d = 0.1$) likewise results in an unacceptable deviation of the solar evolutionary track from the standard track.

3.3. Influence of Dark Matter on Models of the Modern Sun

3.3.1. Linear distributions of dark matter in the solar material. Table 3 presents the computations for the solar models with linear distributions of dark matter in the solar material. Since we did not obtain the solar radius and luminosity for all the models with the indicated age, Table 3 also presents the radii and luminosities for the models that are nearest to the solar values. Model 1 is the standard model of the present-day Sun. In the nonstandard models with dark matter, we took $\alpha = 0.02$, 0.05, and 0.10 (models 2, 3, and 6). To elucidate the effect of the dark-matter distribution in the star, we also computed models with $\alpha_m = 0.05$ and $d = 0.5$ and 1.5 (models 4 and 5). The central α's for the last two models were 0.025 and 0.075, while the surface α's were 0.075 and 0.025.

The results obtained for these nonstandard solar models lead to the following conclusions.

(1) We were not able to obtain models reproducing the modern Sun in the framework of the commonly accepted formalism if the dark-matter fraction exceeds ∼5%, despite the fact that we allowed obviously unrealistic mixing lengths for the convection (models 3, 4, and 6).

(2) We can obtain a model that reproduces the modern Sun only if the dark-matter fraction in the outer part of the Sun does not exceed ∼2%, though the mixing length then considerably exceeds the value for the standard Sun (models 2 and 5). We are not able to reproduce the solar radius and luminosity with models containing a large amount of dark matter (models 4 and 6). In addition, the depth of the convective zone in these models considerably differs from R_{conv} for the standard model.

(3) If the concentration of dark matter toward the center is comparatively low, it does not affect the central solar parameters and neutrino fluxes very much. This can be understood as a consequence of the fact

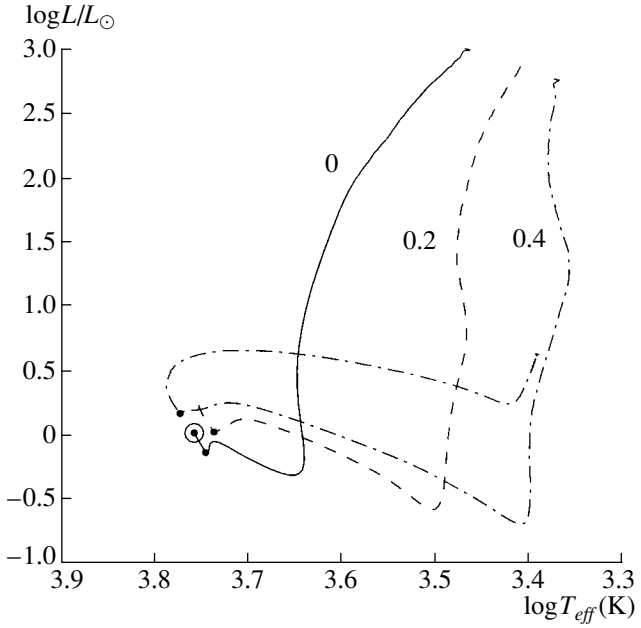

Fig. 2. Tracks in the Hertzsprung–Russell diagram demonstrating the influence of dark matter on the evolution of the Sun. The computations assume a homogeneous distribution of dark matter in the star for various dark-matter fractions α. The solid curve shows the standard track with $\alpha = 0$, while the dashed and dot–dashed curves show the tracks for $\alpha = 0.2$ and $\alpha = 0.4$, respectively. The numbers indicate α. The track with $\alpha = 0.4$ is computed until an age of 4.3 billion years, while the remaining tracks are computed until an age of 4.6 billion years. The filled circles mark the time of the star's arrival at the zero-age main sequence, and the solar symbol indicates the position of the present-day Sun.

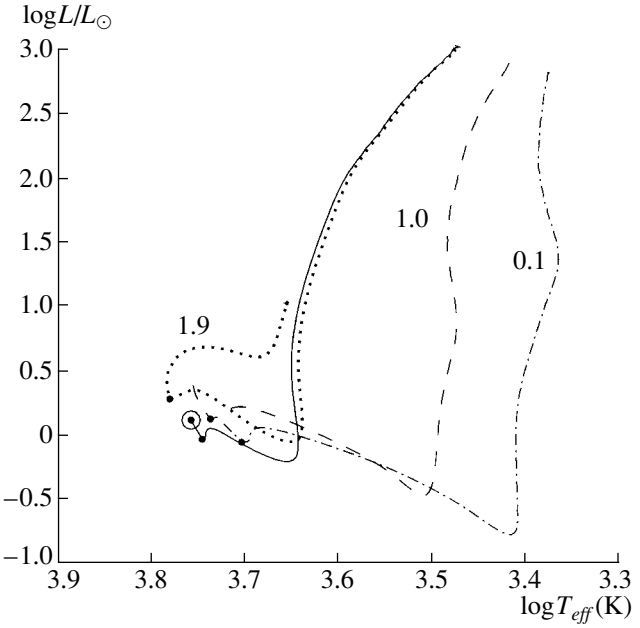

Fig. 3. Tracks in the Hertzsprung–Russell diagram demonstrating the influence of dark matter on the evolution of the Sun. The computations assume linear distributions of dark matter in the star and a mean $\alpha = 0.2$. The solid curve shows the standard track while the dashed curve shows the track computed for a homogeneous distribution of dark matter in the star. The dot–dashed and dotted curves show the tracks for inhomogeneous distributions with the dark matter concentrated toward the surface and center, respectively. The numbers indicate the parameter d (the ratio of the central to the mean α). The tracks are computed until an age of 4.6 billion years. The filled circles mark the time of the star's arrival at the zero-age main sequence, and the solar symbol indicates the position of the present-day Sun.

that the pressure of ordinary matter at the solar center must balance the gravitational force. Since this force is independent of the amount of dark matter for a given total mass, the central temperature and density cannot change appreciably.

3.3.2. Exponential distributions of dark matter in the solar material. To further analyze the effects of the dark-matter distributions on the model parameters for the present-day Sun, we also considered an exponential distribution with dark matter concentrated toward the center of the star. This distribution is described by (2), with the index β being a parameter.

Table 4 presents the computation results for the nonstandard solar models with an exponential distribution of dark matter in the solar material (together with the standard model 1). We computed models for the dark-matter fraction $\alpha_m = 0.05$ and the indices $\beta = 1$, 2, 3, 4, and 5 (models 7, 8, 9, 10, and 11). Despite the comparatively high mean fraction of dark matter, we were able to reproduce the solar radius and luminosity with all these models. We found a considerable increase in l/H_p only for model 7, which has the lowest index, equal to 1, since the structure of the outer stellar layers is strongly changed in this model. However, an increase in the index requires a rapid increase in the central pressure and temperature in order for the pressure to withstand the gravitational force, since the fraction of ordinary matter at the stellar center decreases. Consequently, an increase in β leads to a rapid increase in the solar-neutrino flux. When $\beta > 2$ (models 9, 10, and 11), this flux appreciably exceeds the observed flux (taking into account neutrino oscillations).

Our analysis of these nonstandard solar models leads to the following conclusions.

(1) We can obtain models reproducing the modern Sun with somewhat higher mean fractions of dark matter for an exponential distribution of dark matter concentrated toward the stellar center than for the linear distributions. The contribution of the dark matter can reach ∼5%.

Table 4. Solar models for the exponential dark-matter distributions

No.	α	β	X	l/H_p	T_c, 10^7 K	ρ_c, g/cm^3	F(Cl), SNU	F(Ga), SNU	R_{conv}
1	0.00	–	0.697	1.95	1.505	133.7	6.19	102.3	0.721
7	0.05	1	0.723	3.29	1.513	135.5	7.09	109.6	0.727
8	0.05	2	0.733	2.81	1.518	137.2	7.63	112.4	0.734
9	0.05	3	0.740	2.65	1.523	139.8	8.31	115.5	0.740
10	0.05	4	0.746	2.62	1.531	142.8	9.19	118.9	0.745
11	0.05	5	0.750	2.66	1.539	146.3	10.37	122.8	0.750

Note: No. is the model number and β is the index of the exponential dark-matter distribution. The remaining notation is the same as in Table 3. The radius and luminosity are equal to the solar values for all the models.

(2) When the index of the exponential distribution exceeds ~2, the model neutrino flux appreciably exceeds the observed flux. In addition, the depth of the convective zone for $\beta > 2$ differs appreciably from the depth for the standard model.

3.3.3. Influence of time variations of the dark matter on the nonstandard solar models. To further analyze the possible influence of dark matter on the solar models, we studied the case when the fraction of dark matter grows with time, reaching the specified amounts only when the star's age reaches the age of the present-day Sun. The computations were carried out for homogeneous distributions of dark matter over the star, with $\alpha = 0.02$ and 0.05. Table 5 presents these results together with the results for the same α values but constant fractions of dark matter. A comparison of these models shows that the difference between the nonstandard and standard solar models decreases somewhat when the fraction of dark matter is low in the initial stages of the star's evolution and then grows with time. For example, when $\alpha = 0.05$, we can obtain a model that is close to the modern Sun with $l/H_p \approx 5$ for a constant fraction of dark matter and with $l/H_p \approx 4$ for a fraction of dark matter that grows with time. However, this is not fundamental. In addition, we cannot fit the model radius and luminosity to the solar values in either case.

3.3.4. Role of the mixing length from convection theory. Let us briefly consider the mixing length from convection theory. We use in our computations (as do most theoretical computations of stellar evolution) the classical Bohm–Vitense [42] mixing-length theory. The mixing length is the distance traveled by a convecting element until its material becomes mixed with the surrounding layers. The parameter used in convection theory is l/H_p: the ratio of this distance l to the local pressure scale height H_p (the distance at which the gas pressure decreases by a factor of e). General physical arguments suggest that l/H_p should be close to unity (most stellar-evolution calculations were initially performed with this value). However, a comparison of theoretical stellar models with the observations indicates that l/H_p is instead 1.5–2 (see, for example, [43]). An analysis of the solar model leads to the same conclusion [41].

Note that l/H_p is bounded from above by the condition that the mixing length not exceed the depth of the convective zone $\sim 0.29 R_\odot$, which is well determined from helioseismological data [35–38]. The pressure scale height H_p increases from the surface toward the center, reaching $\sim 10^{10}$ cm (in the model of the modern Sun) at the base of the convective envelope, while the depth of the convective zone is $\sim 2 \times 10^{10}$ cm. Therefore, models admitting $l/H_p > 2$ are not self-consistent, and this parameter must be constrained during the construction of the solar models.

Test computations for models of low-mass main-sequence stars show that increasing l/H_p in the convective envelopes results in an increase in the luminosity (due to the more efficient convective energy transport) and a decrease in the stellar radius. Direct specification of l/H_p is not possible, since this quantity is used to adjust the model of the modern Sun to the observed parameters. To demonstrate the effect of increasing l/H_p on the model parameters, we computed the evolution of a star with the solar mass and chemical composition for model 1 from Table 3 adopting $l/H_p = 5$, 10, and 20. The corresponding radii of the model with an age of 4.6 billion years are 0.88, 0.84, and 0.82 of the solar radius, while the luminosities are 1.08, 1.14, and 1.16 of the solar luminosity. Of course, such variations of the solar parameters are inadmissible departures from the standard parameters.

Table 5. Comparison of solar models with a constant fraction of dark matter and those with the fraction of dark matter growing linearly with time

No.	α	X	l/H_p	T_c, 10^7 K	ρ_c, g/cm^3	F(Cl), SNU	F(Ga), SNU	$\log(R/R_\odot)$	$\log(L/L_\odot)$	R_{conv}
2	0.02	0.704	2.55	1.508	134.1	6.49	104.4	0.000	0.000	0.722
12	0.02	0.701	2.50	1.508	133.5	6.46	104.5	0.000	0.000	0.716
3	0.05	0.714	5.05	1.512	134.7	6.93	107.7	0.001	0.000	0.723
13	0.05	0.712	3.99	1.508	133.0	6.67	107.1	−0.002	0.001	0.750

Note: Notation is the same as for Table 3. The dark matter is distributed homogeneously in all models. In models 2 and 3, the fraction of dark matter is constant, while in models 12 and 13 it grows linearly with time, reaching the indicated amounts only when the star's age reaches 4.6 billion years.

Table 6. Solar models including energy release of the dark matter

No.	δ	X	l/H_p	T_c, 10^7 K	ρ_c, g/cm^3	F(Cl), SNU	F(Ga), SNU	R_{conv}
1	0.00	0.697	1.95	1.505	133.7	6.19	102.3	0.721
14	0.01	0.697	1.95	1.501	132.9	5.87	100.7	0.722
15	0.02	0.697	1.96	1.497	132.3	5.59	99.3	0.722
16	0.03	0.697	1.96	1.492	131.4	5.22	97.4	0.722
17	0.04	0.697	1.96	1.488	130.6	4.92	95.7	0.723
18	0.05	0.697	1.97	1.484	129.9	4.71	94.4	0.723

Note: No. is the number of the model and δ is the ratio of the energy release of the dark matter to the mean solar energy release. The remaining notation is the same as in Table 3. The radii and luminosities of all models are equal to the solar values.

4. INFLUENCE OF ENERGY RELEASE OF NONGRAVITATING DARK MATTER ON THE SOLAR MODELS

We also examined the case when dark matter is manifest via energy released during interactions with ordinary matter (rather than via its gravitation). The mean energy release of the solar material, taken to be the ratio of the solar luminosity and mass, is approximately 2 erg/s. The parameter used in our computations was the ratio δ of the energy release of the dark matter to the mean solar energy release. Thus, we supposed that there was an additional energy release homogeneously distributed over the stellar mass. The presence of an additional energy release must diminish the energy release of the core thermonuclear reactions, since the total energy release of the Sun must be constant and equal to the solar luminosity. Consequently, the central temperature and density of the model must be diminished and the neutrino flux lowered. The models with $\delta = (1–5)\%$ presented in Table 6 together with the standard model demonstrate this effect. Increasing δ to 0.05 diminishes the flux of chlorine neutrinos to unacceptably low levels.

5. ESTIMATES OF DARK MATTER IN THE SOLAR SYSTEM AND DARK MATTER ACCRETED BY THE SUN

For a complete analysis, we must take into account the possible accretion of dark matter in the solar system resulting from an interaction with the Sun. Finally, the main portion of the dark matter could be located outside the Sun itself. Therefore, several attempts were made to place limits on the amount of dark matter in the solar system. One such estimate is based on the precession of the orbits of celestial bodies in the solar system, supposing this precession to be due to a dispersed mass of gravitating bodies instead of point masses [44, 45]. The observed rate of precession of the orbit of the asteroid Icar limits the density of interplanetary space within the Earth's orbit to $\sim 2 \times 10^{-16}$ g/cm^3. The density is estimated within the eccentric orbit of the asteroid, which covers the range 0.2–2 AU. Assuming a constant density within the Earth's orbit, we obtain an upper estimate for the total amount of dark matter of $\sim 10^{-9} M_\odot$. On the other hand, terrestrial seismology provides an upper limit for dark matter in the Earth of $\sim 10^{-8} M_\odot$ [46].

Navigational computations of spacecraft orbits are very promising for the estimation of the amount of dark gravitating matter in the solar system. The additional acceleration due to background material with a constant density can be estimated as $\alpha G M_\odot A^{-2}$, where G is the gravitational constant and A is the semimajor axis of the orbit. The deviation of the spacecraft due to dark matter is $\Delta r \sim 0.5\alpha G M_\odot A^{-2} t^2$. Assuming small deviations ($\Delta r < r$), we obtain the limit $\alpha < 2\, r A^2/GM_\odot t^2$. Then, if we assume the accuracy of the spacecraft position to be one kilometer per year of flight for $A = 1.5 \times 10^{13}$ cm, the limit will be $\alpha < 4 \times 10^{-10}$. Improvements of such estimates for orbits covering a considerable portion of the solar system will enable us to refine these limits.

Measurements of the orbits of the Pioneer-10 and Pioneer-11 spacecraft launched in 1972 and 1973 [47] revealed an additional acceleration of $a_P \sim 8.7 \times 10^{-8}$ cm/s^2 directed toward the Sun at distances of 20–70 AU [48]. Though measurements of this acceleration at shorter distances failed due to masking by other effects, a special spacecraft for further studies is being discussed [49]. If dark matter is responsible for this anomalous acceleration, then $a_P = G\left(M_\odot + \int\limits_0^R 4\pi r^2 \rho(r) dr\right)/R^2$. If a_P does not depend on R, the density of the dark matter is $\rho(R) = a_P/(2\pi G R)$. For $R = 20$ AU, we obtain $\rho = 7 \times 10^{-16}$ g/cm^3. However, note that the density obtained for a continuous distribution of such matter considerably exceeds the required density of dark matter in the Galaxy. This question requires additional studies.

It is important that dark matter inside the Sun probably cannot result from the accretion of dark matter distributed continuously in our Galaxy. Let us estimate the density of this matter if all the mass within the Sun's circular orbit in the Galaxy were dark matter. We obtain the density $\sim 2 \times 10^{-24}$ g/cm^3. Let us suppose the velocity of the dark-matter carriers is 300–1000 km/s, to ensure they are bound by massive galaxies and galaxy clusters. If the Sun accreted all the dark-matter carriers encountering its cross section, the total mass accreted over 4.6 billion years would be $\sim 10^{-10} M_\odot$. Increasing the velocity of the dark-matter carriers to the speed of light will increase the amount of dark matter inside the Sun to only $\sim 3 \times 10^{-8} M_\odot$. Thus, to considerably increase the fraction of dark matter inside the Sun, we must suppose that the carriers are associated with ordinary matter and enter stellar interiors during star formation.

Using the derived density of dark matter, we can estimate the additional energy release in the solar interior corresponding to the radiation of the entire rest mass of the dark matter absorbed by the Sun (assuming the velocity of the dark-matter carriers reaches the speed of light). The additional solar luminosity will be $\sim 10^{-4} L_\odot$. Increasing this luminosity again requires the decay of dark-matter carriers trapped during the formation of the Sun.

6. CONCLUSIONS

The aim of this work is to attempt to place limits on the fraction of dark matter in the Sun by modeling the solar structure and evolution in the framework of standard stellar-evolutionary theory. This theory has proved its worth in the interpretation of modern multiwavelength observations of stars in various stages of their evolution. This theory has also recently been successfully applied to modeling of the evolution of various types of galaxies. The prediction of a solar-neutrino flux that satisfactorily coincides with the observations, brought about via an improved understanding of the properties of neutrinos allowing for neutrino oscillations, is an important achievement of the modern theory of stellar evolution that provides new verification of its self-consistency. The modern model of the Sun is believed to be so reliable that it is planned to apply it to estimate the accuracy of the gravitational constant [50].

The limit of (2–5)% that we have obtained here for the possible fraction of dark matter in the Sun, and probably in other solar-mass stars (which includes, by virtue of the observed stellar-mass function, a large fraction of all stellar material), seems to be a natural consequence of the low density of dark matter and its weak interaction with ordinary matter. These features prevent the collapse of the dark matter during star formation (in contrast to the ordinary matter) and its accretion during the evolution of stars. The dark matter is probably distributed in interstellar space at the peripheries of galaxies and in clusters of galaxies, whose gravitation is sufficient to bind this matter if the velocity of its carriers does not exceed 300–1000 km/s, which is close to the escape velocities of galaxies and galaxy clusters. This last limit results from the fact that the dynamical times for galaxies and galaxy clusters are obviously shorter than the age of the Universe.

Our estimates of the amount of dark matter in the solar system and for the dark matter accreted by the Sun over its lifetime thus far suggest that, if stars contain small amounts of dark matter, they acquired it during their formation.

ACKNOWLEDGMENTS

This work was supported by a Grant of the President of the Russian Federation in Support of Leading Scientific Schools of Russia, the Federal Science and Technology Program in Astronomy, the program of the Russian Academy of Sciences Presidium "Nonstationary Phenomena in Astronomy," and the Russian Foundation for Basic Research (project no. 03-02-16254).

REFERENCES

1. J. H. Oort, Bull. Astron. Inst. Netherlands **6**, 249 (1932).
2. F. Zwicky, Astrophys. J. **86**, 217 (1937).
3. J. Ostriker, P. Peebles, and A. Yahil, Astrophys. J. **193**, L1 (1974).
4. F. Kahn and L. Woltjer, Astrophys. J. **130**, 705 (1959).
5. M. S. Roberts and A. H. Rots, Astron. Astrophys. **26**, 483 (1973).
6. J. Einasto, A. Kaasik, and E. Saar, Nature **250**, 309 (1974).
7. V. C. Rubin, N. Tonnard, and W. K. Ford, Astrophys. J. **225**, L107 (1978).
8. T. Takamiya and Y. Sofue, Astrophys. J. **534**, 670 (2000).
9. J. Gallagher, D. Hunter, and A. Tutukov, Astrophys. J. **284**, 544 (1984).
10. A. Heavens, B. Panter, P. Jimenes, *et al.*, astro-ph/0403293 (2004).
11. M. Rees, astro-ph/0402045 (2004).
12. V. Belokurov, N. Evans, and Y. Du, astro-ph/0404232 (2004).
13. C. Afonso, J. Albert, J. Andersen, *et al.*, Astron. Astrophys. **400**, 951 (2003).
14. J. Einasto, astro-ph/0401341 (2004).
15. D. N. Spergel, L. Vedre, H. V. Persis, *et al.*, Astrophys. J., Suppl. Ser. **148**, 175 (2003).
16. W. A. Chiu, X. Fan, and J. Ostriker, Astrophys. J. **599**, 759 (2003).
17. M. Tegmark, M. A. Stauss, M. R. Blanton, *et al.*, astro-ph/0310723 (2003).
18. S. Nesseris and L. Perivolaropoulos, astro-ph/0401556 (2004).
19. Y. Wang and M. Tegmark, astro-ph/0403292 (2004).
20. B. J. Barris, J. L. Tonry, S. Blondin, *et al.*, Astrophys. J. **602**, 571 (2004).
21. M. A. Markov, Prog. Theor. Phys. Suppl. **85** (1965).
22. M. A. Markov, Zh. Éksp. Teor. Fiz. **51**, 878 (1966) [Sov. Phys. JETP **24**, 584 (1967)].
23. S. W. Hawking, Commun. Math. Phys. **55**, 133 (1977).
24. E. M. Drobyshevski, astro-ph/0402367 (2004).
25. C. Munoz, Astrophys. J. **594**, L71 (2003).
26. N. Afshordi, P. McDonald, and D. N. Spergel, astro-ph/0302035 (2003).
27. B. J. Carr, astro-ph/0310838 (2003).
28. I. Yu. Kobzarev, L. B. Okun', and I. Ya. Pomeranchyuk, Yad. Fiz. **3**, 1154 (1966) [Sov. J. Nucl. Phys. **3**, 837 (1966)].
29. M. Yu. Khlopov, G. M. Beskin, N. G. Bochkarev, and L. A. Pustil'nik, Astron. Zh. **68**, 42 (1991) [Sov. Astron. **35**, 21 (1991)].
30. R. Foot and Z. K. Salagadze, astro-ph/0104251 (2001).
31. R. Foot, astro-ph/0403043 (2004).
32. T. Takamiya and Y. Sofue, Astrophys. J. **534**, 670 (2000).
33. A. B. Severny, V. A. Kotov, and T. T. Tsap, Nature **259**, 89 (1976).
34. V. A. Kotov, V. I. Khaneichuk, and T. T. Tsap, Kinemat. Fiz. Neb. Tel **16**, 49 (2000).
35. A. V. Tutukov and A. V. Fedorova, Astron. Zh. **79**, 281 (2002) [Astron. Rep. **46**, 255 (2002)].
36. A. V. Kosovichev and A. V. Fedorova, Astron. Zh. **68**, 1015 (1991) [Sov. Astron. **35**, 507 (1991)].
37. J. Bahcall, A. Serenelli, and M. Pinsonneault, astro-ph/0403604 (2004).
38. S. Basu and H. Antia, astro-ph/0403485 (2004).
39. J. Bahcall and M. Pinsonneault, astro-ph/0402114 (2004).
40. S. P. Mikheev and A. Yu. Smirnov, Usp. Fiz. Nauk **153**, 3 (1987) [Sov. Phys. Usp. **30**, 759 (1987)].
41. J. N. Bahcall, *Neutrino Astrophysics* (Cambridge Univ. Press, Cambridge, 1998; Mir, Moscow, 1993).
42. E. Bohm-Vitense, Z. Astrophys. **46**, 108 (1958).
43. D. A. Van den Berg and T. J. Bridges, Astrophys. J. **278**, 679 (1984).
44. L. Bracci and G. Fiorentini, Nuovo Cimento C, Ser. 1 **12C**, 121 (1989).
45. O. Gron and H. Soleng, Astrophys. J. **456**, 445 (1996).
46. A. Inatiev and R. Volkas, Phys. Rev. D **62**, 023508 (2000).
47. J. D. Anderson, Ph. A. Laing, E. L. Lau, *et al.*, Phys. Rev. D **65**, 082004 (2002).
48. R. Foot and R. Volkas, Phys. Lett. B **517**, 13 (2001).
49. M. M. Nieto and S. G. Turyshev, gr-qc/0308017 v3 (2004).
50. I. P. Lopes and J. Silk, Mon. Not. R. Astron. Soc. **341**, 721 (2003).

Translated by V. Badin

Astronomy Reports, Vol. 49, No. 2, 2005, pp. 144–154. Translated from Astronomicheskiĭ Zhurnal, Vol. 82, No. 2, 2005, pp. 168–179.

The Nature of Decimeter-Wave Microburst Emission

V. M. Bogod[1] and L. V. Yasnov[2]

[1]*St. Petersburg Branch of the Special Astrophysical Observatory, Russian Academy of Sciences, Pulkovo, St. Petersburg, 196140 Russia*

[2]*Research Institute of Radiophysics, St. Petersburg State University, Ul'yanovskaya ul. 1, Staryĭ Peterhof, St. Petersburg, 198504 Russia*

Received February 22, 2004; in final form, September 20, 2004

Abstract—New observations of solar microbursts are reported. The spectra of microbursts can contain narrow features ($\Delta f/f \leq 0.03$). Possible mechanisms for the generation of the microburst radio emission are analyzed, focusing on mechanisms that preferentially generate ordinary waves. Together with the well-known generation of radio emission at the fundamental plasma frequency, mechanisms associated with upper-hybrid waves and resonant-transition radiation are considered. The radio emission at the upper-hybrid frequency always corresponds to ordinary waves. Ordinary waves can also dominate in resonant-transition radiation, but the presence of well-developed small-scale turbulence in the emission region is required. Possible mechanisms for the generation of this turbulence include thermal fluctuations, Langmuir turbulence, quasi-stationary structures created by plasma waves, and ion-acoustic waves. Probable origins of the quasi-periodicity of microbursts are analyzed. © *2005 Pleiades Publishing, Inc.*

1. INTRODUCTION

Prolonged decimeter-wavelength microbursts were detected in strip scans in total and polarized intensity with a sensitivity of about 10–12 Jy derived from observations with the RATAN-600 radio telescope at several wavelengths simultaneously. The degree of polarization of microbursts reaches 100%, and corresponds to an ordinary wave. The microbursts have fluxes of 0.001–0.1 sfu, and are present over several days, appearing at sites of prolonged energy release. The region where the microbursts are generated is located at a height of about 15 000 km. The duration of an individual microburst is about 1–2 s. Earlier, we discussed a model for the generation of radio waves at the first harmonic of the plasma frequency [1]. We analyzed the correlation between microbursts observed with RATAN-600 at 1 GHz and type I bursts observed at 233 and 164 MHz with the Nançay radio heliograph. Pulses of emission at 164 and 233 MHz arise after the appearance of microbursts at 1000 MHz. The mean time delay is 7–8 s between 1000 and 164 MHz and 3–5 s between 1000 and 233 MHz. The durations of microbursts at decimeter wavelengths are virtually identical with the durations of the corresponding pulses at meter waves (about 1–2 s); the periods with which they appear are 3–5 s [1–3]. In intervals when microbursts are present, the continuum radio emission of the active region could be nonthermal [4].

Below we present new observations of microbursts and analyze possible mechanisms for the generation of microburst radio emission.

2. NEW OBSERVATIONS OF MICROBURSTS

The radio fluxes of microbursts are very small, making microbursts extremely difficult to detect. Therefore, there are few available data on microbursts, and each case of microburst detection is of interest. The horizontal beam size of RATAN-600 at decimeter wavelengths is about 4′, so that the broad beam of the radio telescope covers an entire active region during approximately 40 s. Fast impulsive processes, such as microbursts, which have durations of about 1 s (15″–22″ in angular measure), may occur during the transit time. We have discussed the reality of the observed microbursts earlier in [1–4], where we pointed out the correlation between these bursts and type I bursts. Here, we present observations of microbursts in an active region at the eastern limb of the Sun.

In limb observations at centimeter wavelengths using the southern sector and a flat reflector, there is a ~0.5% [5] relative instrumental error in the circular-polarization channels, which resembles a large-scale structure with a size of half of the solar-disk radius, which is much larger than the horizontal beam size. This error is due to the finite vertical size of the beam and the deviation of the beam center from the hour circle passing through the center of the solar disk. At a wavelength of 4 cm, the vertical beam is the

1063-7729/05/4902-0144$26.00

same size as the solar disk, and this error vanishes at longer wavelengths. The fact that the horizontal beam is larger than the typical sizes of microbursts additionally decreases the instrumental errors. Therefore, in decimeter-wavelength observations, this error is negligible for the problem at hand.

Another type of error—a cross-polarization signal due to the shift of the phase centers of the horizontal beams for the right-circular and left-circular polarizations—is absent from observations on the southern sector with the Periscope. The main limitation on the detection of such events is the noise in the receiving system. This allows us to record weak microbursts and their polarization with limiting sensitivities as high as 0.01–0.1 sfu for simultaneous observations at several wavelengths over long time periods (more than two hours).

Some results from new observations of microbursts are presented below.

2.1. Microbursts before and after the Powerful Flare of March 29, 2001

Figure 1 shows scans of the solar disk at 31.41, 30.46, 29.56, and 28.71 cm derived from multi-azimuth RATAN-600 observations on the southern sector with the Periscope [6]. The active region NOAA 9393 was in the western part of the disk, and it was the only powerful object at that time. In the time interval considered, this region produced a powerful M2.7 X-ray flare on March 29 at $10^{h}06^{m}$ UT (GOES satellite data). Microbursts appeared in this active region one and a half hours before the flare and ended half an hour after its completion. Figure 1 presents radio observations obtained before and after the flare. On that day, observations were carried out every eight minutes over $2^{h}40^{m}$. The observations showed strong temporal variability and a high correlation of the polarized signal at all wavelengths. We can also see from Fig. 1 that the circularly polarized emission of this region (Stokes parameter V in the left-hand column of the graphs) contains continuous and pulsed components [3]; the total intensity (Stokes parameter I) for the same wavelengths and times is shown in the right-hand column. To more clearly display the weak signals of the pulsed component in the polarized emission of the active region, we smoothed the observed curve using a Gaussian filter, then subtracted the smoothed curve from the initial data. We chose the parameters of the Gaussian filter so that the pulse amplitudes did not change by more than 10%.

2.2. Microbursts in the Active Region NOAA 9415 on April 4, 2001

Figure 2 shows another example of microbursts associated with the flare-producing active region NOAA 9415. This region was observed on RATAN-600 from the time it rose to the time it set; its centimeter-wavelength emission is described in detail in [7]. It was recorded at the three decimeter wavelengths 30.46, 29.56, and 28.71 cm over $2^{h}40^{m}$. Figure 2 presents scans of the polarized emission at these wavelengths for the time interval from $9^{h}08^{m}35^{s}$ to $10^{h}20^{m}47^{s}$. This figure demonstrates the dynamics of the microbursts.

At $9^{h}40^{m}40^{s}$, the microburst intensity is at a maximum at all wavelengths, whereas, e.g., at $10^{h}04^{m}44^{s}$, the microburst intensity is low, and we can see that there are no instrumental errors with the size of the studied microbursts at the eastern limb; this is also visible at $9^{h}08^{m}35^{s}$, $9^{h}16^{m}36^{s}$, etc.

The microbursts in Fig. 3 have parameters (flux, duration, quasi-periodicity) close to those obtained earlier [1–3]. However, we also note some new features of the microbursts related to their sharp frequency structure. For instance, three microbursts are clearly distinguishable at 29.56 cm near the solar limb. The two outer ones are clearly visible at 30.46 and 29.56 cm, but are virtually absent at 28.71 cm. On the contrary, the middle microburst is prominent at 28.71 and 29.56 cm and is virtually absent at 30.46 cm. The microburst in the right-hand part of the figure is present only at 29.56 cm, and is barely detectable at the other wavelengths. These observations indicate that microbursts either have a sharp frequency limit or are narrow-band features. In both cases, $\Delta f/f \leq 0.03$.

3. POSSIBLE MECHANISMS FOR MICROBURSTS

As mentioned above and in [1–4], the microburst emission displays ordinary polarization, and all models must include this important fact. Earlier, we considered a plasma mechanism for radiation at the fundamental harmonic of the Langmuir frequency [1]. In addition, we will analyze below two possible mechanisms associated with the generation of upper-hybrid waves and resonant transition radiation (RTR). An important problem in the latter mechanism was finding a source of small-scale inhomogeneities and determining the conditions at which the RTR dominates over plasma and gyrosynchrotron radiation.

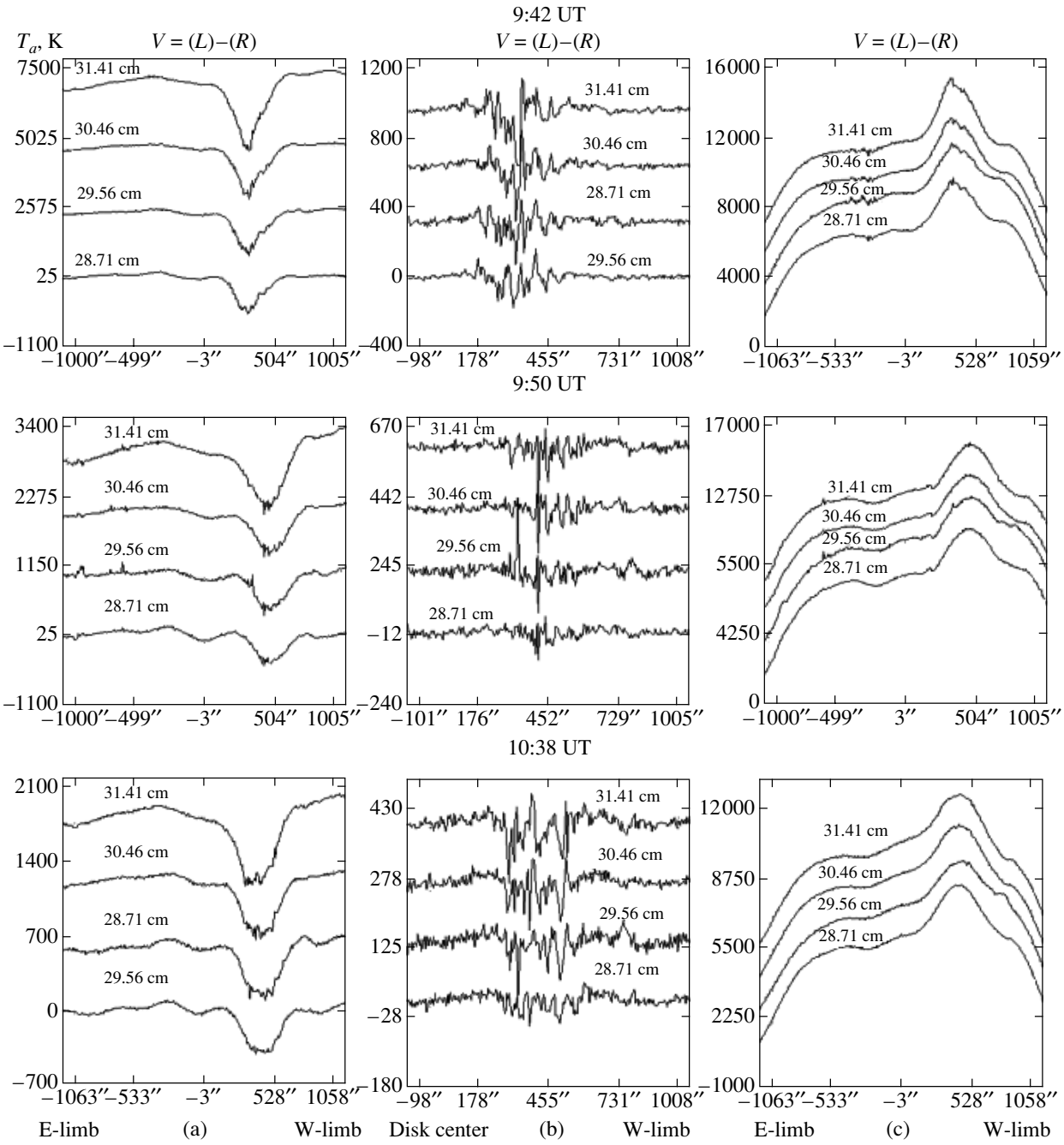

Fig. 1. Strip scans of the solar disk obtained on RATAN-600 at several wavelengths from 28.71 to 31.41 cm for three observation times on March 29, 2001. The left column shows the circularly polarized emission (Stokes parameter $V = I(L) - I(R)$), the right panel shows the total intensity (Stokes parameter $I = I(L) + I(R)$), and the middle panel shows the pulsed component, obtained via the subtraction of large-scale structures.

3.1. Radiation at the First Harmonic of the Plasma Frequency

Let us calculate the flux of the plasma radiation at the fundamental harmonic, since the ordinary emission can dominate in this case. The reasons for this are known and were described earlier (see, e.g., [8]). If the well-known inequality [8]

$$\frac{f_p^2}{f^2} > 1 - \frac{f_b|\cos\theta|}{f} \qquad (1)$$

is satisfied in the emission region, the radiation will be completely polarized in the ordinary mode. Here, f is the frequency of the radiation, f_p and f_b are the plasma frequency and gyrofrequency, and θ is the

angle between the direction in which the radiation propagates and the magnetic field. If we use the following relationship for the plasma radiation

$$f^2 = f_p^2\left(1 + \frac{3v_t^2}{v_p^2}\right), \qquad (2)$$

where v_t is the thermal velocity of the electrons and v_p is the phase velocity of the Langmuir waves (L waves), inequality (1) becomes

$$\frac{f_b|\cos\theta|}{f} > \frac{3v_t^2}{v_p^2}. \qquad (3)$$

Hence, we can find a lower limit for the magnetic-field intensity in the source. For $f = 1000$ MHz, $T_e = 2\times10^6$ K, $v_p = 0.3$ s, and $\cos\theta = 1$, we find $B > 4$ G.

If upper-hybrid waves are generated, whose frequency $f_{UH} = \sqrt{f_p^2 + f_b^2}$ and $f_{UH} = af_b$, where a is some number greater than unity, the emission at frequency $f = f_{UH}$ will be ordinary-polarized when

$$|\cos\theta|a - 1 > 0. \qquad (4)$$

This condition is readily satisfied when the radiation propagates roughly along the field, especially since the increment of the upper-hybrid waves grows when a becomes close to an integer and is increasing [9, 10].

We will estimate the radiation flux using the formulas for the mechanism for emission at the first harmonic of the plasma frequency presented in [11]. We also took into account thermal bremsstrahlung absorption of the radio emission, which can also be important at the second harmonic of the plasma frequency. We assumed that the Langmuir waves (L waves) are in resonance with an electron beam and have phase velocities close to the beam velocity. The velocity of electrons was taken to be $0.3c$. The line-of-sight size of the source for emission at a fixed frequency was everywhere taken to be the size of the region along the path of the radio-wave propagation, for which the electron density can be assumed constant: $l = 3Hv_t^2/v_p^2$ (see, e.g., [12]). Here, H is the electron-density scale height.

As was shown in [1], the radiation flux in sfu in this case can be estimated as

$$F = \frac{1.7fsT_e^{3/2}v_p^2w}{10^{49}\ln(4.3\times10^6T_e^{2/3}f^{-2/3})}, \qquad (5)$$

where f is the frequency in Hz, T_e is the electron temperature in Kelvin, v_p is the phase velocity of the L waves in cm/s, w is the ratio of the energy of the L waves to the thermal energy of the plasma, $n_ek_bT_e$ (k_b is Boltzmann's constant), s is the source area in cm^2, and n_e is the electron density.

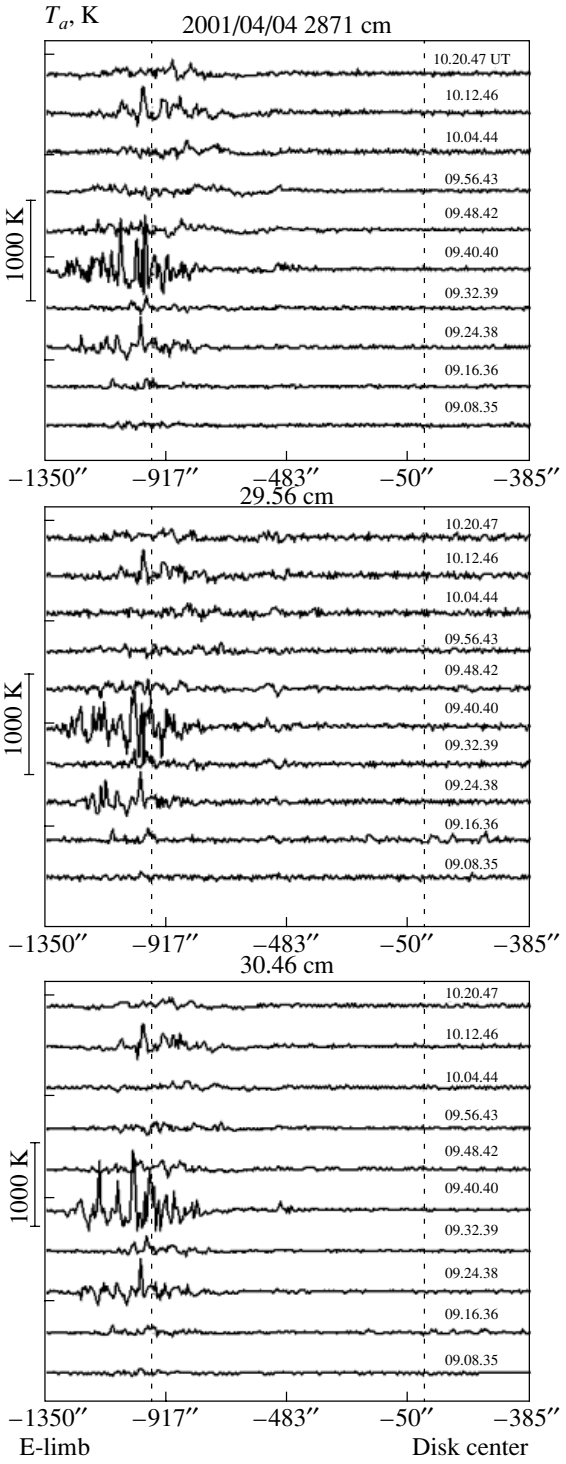

Fig. 2. Microbursts in the polarized emission of the active region NOAA 9415.

If we assume that $s = l^2$, we find

$$F = \frac{3.8fH^2T_e^{7/2}w}{10^{26}v_p^2\ln(4.3\times10^6T_e^{2/3}f^{-2/3})}, \qquad (6)$$

where H is the electron-density scale height in cm.

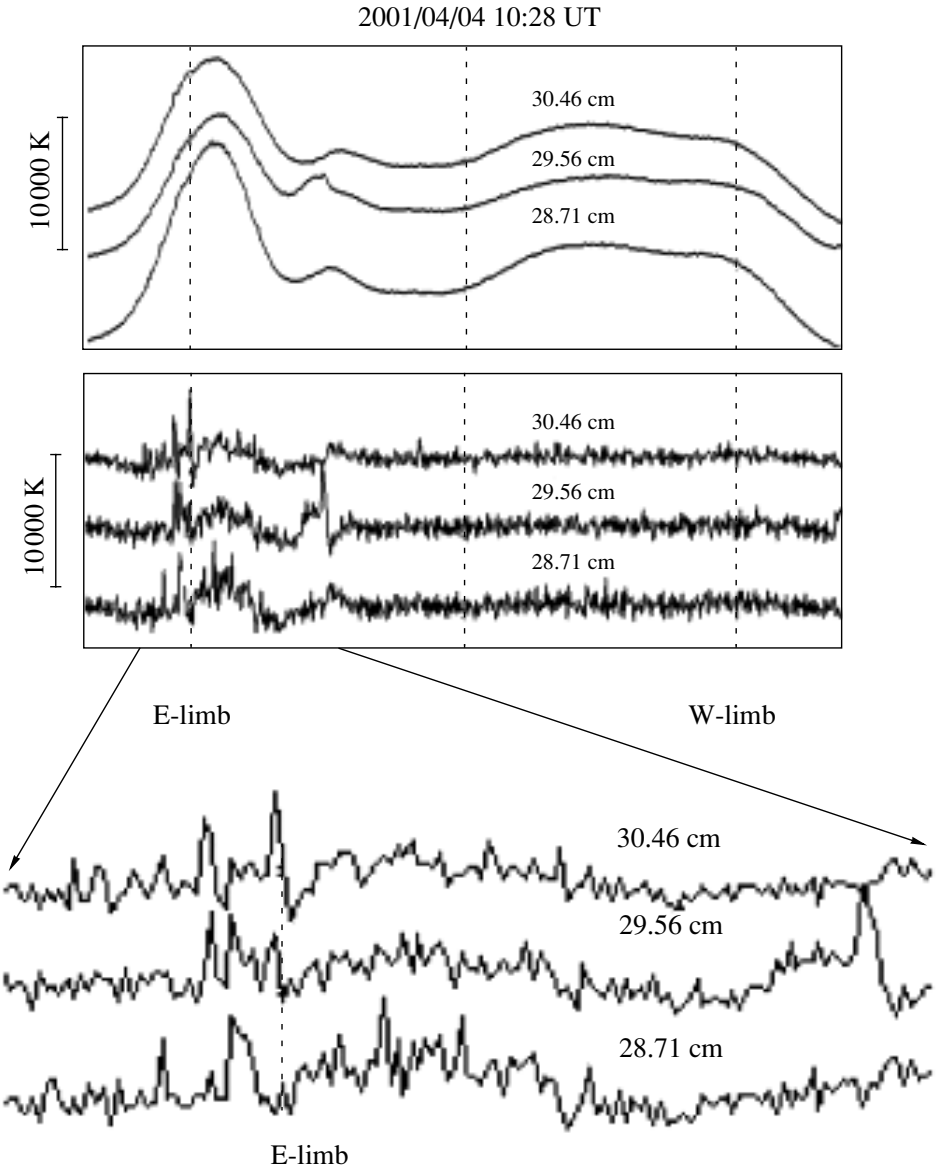

Fig. 3. Micorbursts of the active region NOAA 9415B in the total-intensity channel without and with subtraction of the continuous component. The bottom plot shows a segment with microbursts on a larger scale.

Adopting as above $T_e = 2 \times 10^6$ K, $v_p = 0.3c$, and $H = 10^{10}$ cm, we obtain the estimated energy of the L waves for $f = 10^9$ Hz:

$$F = 4.8 \times 10^4 w. \quad (7)$$

Thus, we have for a tenth of a solar flux unit (a typical maximum microburst flux at decimeter wavelengths) $w = 2 \times 10^{-6}$.

The main difficulty in interpreting microbursts as radio emission at the fundamental plasma frequency is associated with the high directivity of this radiation, which implies a low probability for detecting it at the Earth. The mechanism of radio emission at frequency $f = f_{UH}$ is free of this drawback.

3.2. Radiation at the Second Harmonic of the Plasma Frequency

Upper-hybrid waves are generated most efficiently under the conditions present in magnetic loops, when energetic electrons are captured in a magnetic trap. Zaĭtsev and Stepanov [11] have shown that radiation at the second harmonic arising from the nonlinear interaction of two upper-hybrid waves is more intense than radiation at the fundamental harmonic if the level of high-frequency turbulence $w < 10^{-4}$. The dominance of ordinary waves in the radiation at the second harmonic is possible due to the strong cyclotron absorption of extraordinary waves in the upper layers of the solar atmosphere at gyrolevels with $s \leq 3$ [13, 14].

Thus, the condition

$$f = 2f_{UH} \leq 3f_b, \tag{8}$$

should be satisfied, where the frequency of the upper-hybrid waves $f_{UH} = \sqrt{f_p^2 + f_b^2}$.

Electrostatic instability is possible at $f_p > f_b$. We then find that the magnetic-field intensity in the generation region is $H = 120$–126 G, while the electron density is $n = (1.4$–$1.9) \times 10^9$ cm^{-3}.

In this case, the radiation flux for $s = l^2$ is [1]

$$F = \frac{6.03 f^2 H^3 T_e^4 w^2}{10^{48} \upsilon_p}. \tag{9}$$

If $T_e = 2 \times 10^6$ K, $\upsilon_p = 0.3c$, and $H = 10^{10}$ cm (typical for the corona), we obtain an estimate for the energy of the L waves for $f = 10^9$ Hz:

$$F = 1.07 \times 10^{16} w^2. \tag{10}$$

Supposing $F = 0.1$ sfu, we obtain $w = 3 \times 10^{-9}$. However, in this case, we must take into account the fact that the increment of the upper-hybrid waves at frequency $f_{UH}/f_b \leq 3/2$ is more than three orders of magnitude lower than, for example, at a frequency of about $f_{UH}/f_b = 6$ [10].

3.3. Transition Radiation

Transition radiation is the term given to that part of the radiation that does not vanish during the constant motion of a charge, but disappears in the limit of a uniform medium. It follows from electrodynamics that radiation will arise in a vacuum if the speed of a charge (namely, υ/c) is changing. In the presence of a medium, the determining parameter for the generation of radiation is the ratio υ/υ_p, where υ_p is the phase velocity of the electromagnetic waves. In the case of a constant velocity, υ/υ_p can vary with changes in υ_p, as takes place in an inhomogeneous medium. It is such changes that give rise to transition radiation. If a fast particle passes through small-scale macroscopic inhomogeneities, coherent radiation of the electrons associated with the inhomogeneities arises, resulting in enhanced radiation, namely, transition radiation.

The most intense transition radiation arises at frequencies close to $f_p(1 + f_B^2/f_P^2)$ and in inhomogeneities with sizes smaller than $l_o < c/f_p$ [15]. This radiation is called resonant transition radiation (RTR).

RTR is most efficient in the conditions of the solar atmosphere. When estimating this efficiency, we must take into account the gyrotropic character of the medium. The presence of a magnetic field will suppress RTR. To calculate the RTR, we must know the energy spectrum of the fast particles (e.g., the spectral index ξ) and the spatial spectrum of the inhomogeneities. The inhomogeneity spectrum is usually represented

$$|\delta N|^2_{k_1} = \frac{\nu - 1}{4\pi} \frac{k_o^{\nu-1} \langle \Delta N^2 \rangle}{k_1^{\nu+2}}, \tag{11}$$

where $l_o = 2\pi/k_o$ is the main scale and $\langle \Delta N^2 \rangle$ is the mean square of the density of the inhomogeneities. Under astrophysical conditions, the fast-particle spectrum is usually represented

$$dN_e = (\xi - 1) N_e (x > x_o) \frac{x_o^{\xi-1} dx}{x^\xi}, \tag{12}$$

where $x = p/mc$ is the dimensionless momentum of a particle.

The magnetic field affects the motion of particles, the emission of electromagnetic waves, and the dispersion of the medium. Below, we consider the case of weak magnetic fields:

$$\frac{\omega_p}{\omega_B} \gg 1. \tag{13}$$

The effect of the magnetic field becomes important when [15]

$$\beta = \frac{\omega_B^2}{3\omega_p^2} \left(\frac{\upsilon}{\upsilon_T} \right)^2 > 2 \times 3^{1/2} \upsilon_T / c, \tag{14}$$

and will become especially important when $\beta \gg 1$. Here, υ is the velocity of the fast particle. The emission of ordinary and extraordinary waves takes place differently in the presence of a magnetic field due to their different indices of refraction.

Accordingly, if the cutoff frequency (i.e., the frequency at which the index of refraction becomes zero) for the extraordinary waves exceeds the peak frequency of the emission, the RTR of extraordinary waves will be strongly suppressed compared to the RTR of ordinary waves. Thus, we have the same situation as for the plasma radiation at frequency $\omega = \omega_p$ in the presence of a magnetic field.

The degree of polarization of the waves grows considerably with increasing ω_B/ω_P, and corresponds to the sign of ordinary waves. The degree of polarization becomes close to 100% if

$$\frac{\omega_B}{3\omega_P} \left(\frac{\upsilon}{\upsilon_T} \right)^2 > 1. \tag{15}$$

In sources of solar decimeter- and centimeter-wave bursts, the relationship

$$\frac{\upsilon_T}{c} < \frac{\omega_B}{\omega_P} < \left(\frac{\upsilon_T}{c} \right)^{1/2}$$

is usually satisfied.

It is natural to assume that the inhomogeneity spectrum is described by a Kolmogorov dependence, i.e., $\nu = 1.7$. If this condition is satisfied, or even if

$$\frac{v_T}{c} < \frac{\omega_B}{\omega_P} < 1, \qquad (16)$$

the polarized radiation typical for microbursts (i.e., with the dominance of ordinary radiation), arises when

$$\xi < \nu + 2 = 3.7.$$

Let us assume that the distribution of the plasma frequency in the radiation region can be described by a power law:

$$F(\omega_P) = (\lambda - 1)\frac{\omega_{Po}^{\lambda-1}}{\omega_P^{\lambda}}, \quad \omega_P > \omega_{Po}, \qquad (17)$$

where ω_{Po} is the smallest value of the plasma frequency in the source. We then have for the flux of ordinary radiation in sfu [15]:

$$F_f^o = 3.45 \times 10^5 C_o (1 + \cos^2\theta)\frac{f_P}{1\ \mathrm{GHz}} x_o^{\xi-1} \qquad (18)$$
$$\times \frac{V N_e}{10^{33}} \frac{\langle \Delta N^2 \rangle}{N^2} \left(\frac{k_o c}{\omega_P}\right)^{\nu-1} \left(\frac{\omega_P}{\omega_B}\right)^{1/2} \frac{c}{v_T} \left(\frac{\omega_P}{\omega}\right)^{\alpha},$$

where

$$C_o = \frac{\pi^2(\lambda-1)(\nu-1)(\xi-1)\Gamma[(\xi-1)/2]\Gamma[(\nu-\xi+2.5)/2]}{36\sqrt{6}(\nu+2)\Gamma[\nu/2+3/4]},$$

V is the volume of the source, and x_o is the minimum dimensionless momentum of the fast electrons. The spectral index α is determined by the dependence of the quantities in (18) on the local plasma frequency. For instance, if

$$\frac{\langle \Delta N^2 \rangle}{N^2} = \mathrm{const}, \quad \frac{k_o c}{\omega_P} = \mathrm{const}, \quad \frac{\omega_P}{\omega_B} = \mathrm{const}, \qquad (19)$$

then $\alpha = \lambda - 1$. The exact value of α is not important, since $\omega \cong \omega_P$.

Let the minimum energy of the electrons be 10 keV, the temperature of the background plasma be $T_e = 2 \times 10^6$ K, $\theta = 45°$, and $f \cong f_P = 1$ GHz. The condition (16) is then satisfied, and the RTR flux is

$$F^o \cong 2 \times 10^{-21} V N_e B^{-1/2} \frac{\langle \Delta N^2 \rangle}{N^2}. \qquad (20)$$

Note that variations of ξ, ν, and λ within reasonable limits result in changes of the coefficient by no more than a factor of two.

By virtue of the Razin effect (the suppression of the radiation of mildly relativistic electrons when $f < f_R = f_P^2/f_B$ [16]) and the condition (13), gyrosynchrotron radiation by fast electrons will not contribute to the emission at 1 GHz. However, radiation from these electrons can appear at higher frequencies. We calculated the gyrosynchrotron emission of fast electrons with the same spectral distribution ($\xi = 3.5$) using the formulas from [17] and the index of the electron energy spectrum δ, which is related to ξ in the nonrelativistic case as $\xi = 2\delta - 1$. Let us compare the flux of the transition radiation at the frequency of the radio emission $f \cong f_P = 1$ GHz and the flux of gyrosynchrotron radiation at frequency $f \cong f_R$. Note that, for the given values of l and ξ, the optical depth to the gyrosynchrotron radiation is less than unity over a broad range of N_e and B. We then obtain for the boundary value of the magnetic-field intensity

$$B_{\mathrm{bound}} = 6100 \left(\frac{\langle \Delta N^2 \rangle}{N^2}\right)^{0.32}. \qquad (21)$$

If this value is exceeded, the region yields more intense gyrosynchrotron radiation at $f \cong f_R$ than transition radiation at $f \cong f_P$. Figure 4 shows this dependence.

Thus, if, for example, $B = 25$ G in the radiation region, 100% polarized RTR will be more intense if

$$\frac{\langle \Delta N^2 \rangle}{N^2} > 3 \times 10^{-8}. \qquad (22)$$

Note, however, that the widely used formulas of [17] neglect the effect of the background plasma on the radiation. As was shown in [18], increasing the density and temperature of the background electrons leads to an appreciable decrease in the gyrosynchrotron radiation. Therefore, the estimated boundary value of the magnetic field, B_{bound} (and all the estimates of B_{bound} given below), should be treated as lower limits. This means that, when the background plasma is taken into account, the RTR at $f \cong f_P$ can be more intense than the gyrosynchrotron radiation

(and appear at a higher magnetic-field intensity than $B_{\rm bound}$). A similar conclusion is derived if the fast-particle spectrum has a break at high energies.

3.4. Probable Origins of Electron-Density Fluctuations

3.4.1. Thermal fluctuations. Thermal fluctuations have the spectrum

$$|\Delta N|_k^2 = \frac{n_i}{(2\pi)^3(1+k^2d^2)^2}. \quad (23)$$

Let us integrate this over the sizes of the fluctuations, from the Debye screening distance $d = v_T/\omega_P$ to the plasma radiation wavelength $2\pi c/\omega_P$, adopt $n_i = N$, and divide the result by N^2. This yields for thermal fluctuations with sizes <30 cm and for a coronal temperature of 2×10^6 K

$$\frac{\langle\Delta N^2\rangle}{N^2} \cong \frac{1}{N}.$$

For a density corresponding to $f_p = 1$ GHz, $N = 1.23\times10^{10}$ cm^{-3}, we obtain

$$\frac{\langle\Delta N^2\rangle}{N^2} = 0.8\times10^{-10}. \quad (24)$$

Thus, explaining the bursts as resonant transition radiation in regions with $B = 25$ G requires density fluctuations two to three orders of magnitude larger than thermal fluctuations [cf. (22)]. However, when $B < 3.5$ G, weak bursts can appear, whose RTR will be more intense than their gyrosynchrotron radiation. Using (20) and (24), we obtain for the flux of such bursts

$$F^o > 8\times10^{-32}slN_e = 24\times10^{-32}sHN_e\frac{v_t^2}{v_p^2}. \quad (25)$$

When $T_e = 2\times10^6$ K, $v_p = 0.3c$, $H = 10^{10}$ cm, and $s = 10^8$ cm^2, we find that a flux of $F = 0.1$ sfu is achieved for $N_e = 10^4$ cm^{-3}. These estimates are only approximate, since the spectra (23) and (11) are considerably different. However, with this quantity of fast particles, radio emission will also arise from plasma waves generated by these particles.

3.4.2. Density fluctuations in a plasma (Langmuir) wave. Let us now consider the density fluctuations created during the generation of plasma waves with energy w by fast electrons. The energy of a wave (kinetic and electromagnetic) averaged over the oscillation period can be expressed in terms of the permittivity ε [19]:

$$\bar{W} = \frac{\bar{E}^2}{8\pi}\frac{\partial}{\partial\omega}(\omega\varepsilon). \quad (26)$$

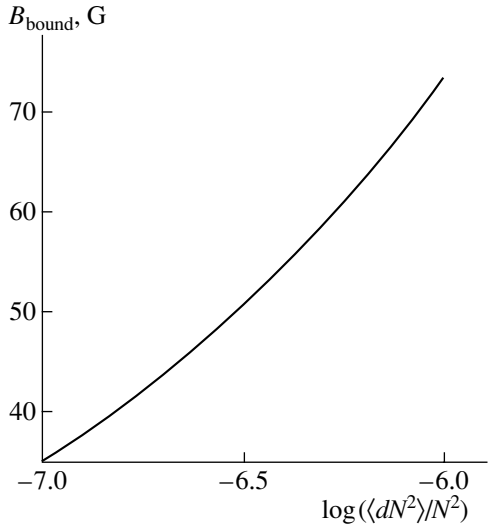

Fig. 4. Boundary value of the magnetic-field intensity $B_{\rm bound}$ as a function of $\langle\Delta N^2\rangle/N^2$.

Here, we have assumed that the wave is electrostatic, with E being the electric field of the wave. The relationship between the electric field of a plane wave and the fluctuations of the electron density is represented by the Poisson equation:

$$ikE = -4\pi e\Delta N. \quad (27)$$

The plasma permittivity is

$$\varepsilon = 1 - \frac{\omega_p^2}{\omega^2}\frac{1}{1-3k^2v_t^2/\omega^2}. \quad (28)$$

We obtain for the plasma-wave frequency (2)

$$W_p = \frac{\Delta N^2}{N^2}\frac{\pi m_e^2 v_p^2 f^2}{e^2}. \quad (29)$$

Comparing this energy with the thermal energy of the plasma and substituting numeric values for some quantities, we obtain

$$w_p = 6.6\times10^{-12}\frac{\Delta N^2}{N^2}\frac{v_p^2 f^2}{T_e f_p^2}. \quad (30)$$

Supposing as above $T_e = 2\times10^6$ K, $v_p = 0.3c$, and $f \cong f_p$, we find that the energy of the wave, $w = 2\times10^{-6}$ [cf. the estimate (7)] corresponds to the electron-density fluctuations

$$\frac{\langle\Delta N^2\rangle}{N^2} = 7.5\times10^{-9}. \quad (31)$$

Thus, comparing (21) and (31), we conclude that the electron-density fluctuations generated by a plasma wave with energy $w = 2\times10^{-6}$ yield less intense RTR than gyrosynchrotron radiation if $B > 15$ G in the emission region.

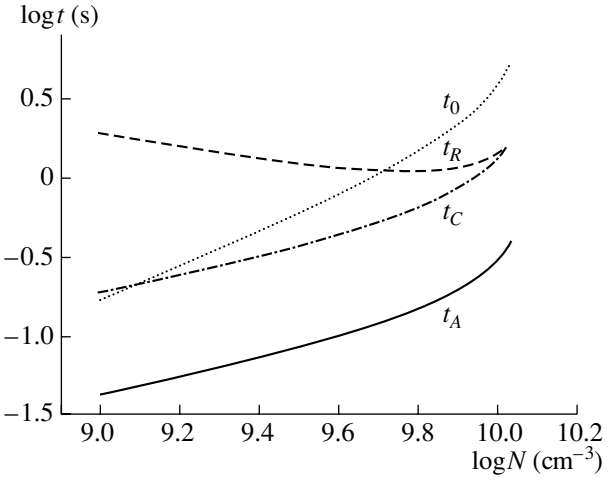

Fig. 5. Pulsation periods calculated for $f = 1$ GHz. The period t_R is given for $T_e = 8 \times 10^6$ K, the period t_0 for $dn = 100$, and the period t_C for $L = 10^{10}$ cm, $L_\perp = 10^8$ cm.

3.4.3. Density fluctuations in an ion-acoustic wave. If the electron temperature in an active region is much higher than the ion temperature, then, due to the Buneman instability, ion-acoustic waves are generated at $\omega = kv_s$, where v_s is the sound speed. In this case, anisotropic turbulence arises with wave numbers of up to $k \cong 1/d$, where the increment takes on its greatest value. Using (25), we can write the energy of these ion-acoustic waves as

$$\bar{W}_s = 2\left(1 + \frac{1}{k^2 d^2}\right)\frac{\bar{E}^2}{8\pi}. \qquad (32)$$

Taking $k \cong 1/d$, where the increment is the largest, and using (27), we obtain for the relative energy of the ion-acoustic waves

$$w_s = 2\frac{\langle \Delta N^2 \rangle}{N^2}. \qquad (33)$$

We have from (20)

$$F^o \approx 10^{-21} V N_e B^{-1/2} w_s. \qquad (34)$$

Thus, for example, for $B = 25$ G, the RTR will be more intense [see (21)] than the gyrosynchrotron radiation if $w_s > 6 \times 10^{-8}$.

3.5. Transition Radiation in Quasi-Stationary Structures Produced by the Plasma Waves Themselves

A mechanism for the formation of quasi-stationary plasma structures was proposed in [20]. Its main basis is that any two plasma-turbulence waves with similar phases and identical scalar wave vectors (i.e., they have the same polar angle relative to the magnetic field, but different azimuthal angles) will form a stationary structure across the magnetic field. The damping of plasma waves on electrons of the background plasma heats electrons at the antinodes and draws them toward the nodes of the stationary structure. This heating, in turn, by virtue of the conservation of pressure in the completely ionized plasma, amplifies the electron-density perturbations. The field-aligned scale of such a structure (the scale of inhomogeneities of the source of plasma waves) in the case of a low level of plasma turbulence (when nonlinear effects can be neglected) is $L_P \approx 2v/f_c$. The dispersion of the relative density inhomogeneities is $\langle \Delta N^2 \rangle / N^2 = 4\pi (v/v_t)^2 w \sqrt{5 d_e / L_P}$. For coronal plasma with $T_e = 2 \times 10^6$ K, $v = 0.3c$, and $f \cong f_P = 1$ GHz, we have $\langle \Delta N^2 \rangle / N^2 = 0.27w$. For $w = 2 \times 10^{-6}$, the dispersion of the electron-density inhomogeneities is higher for this mechanism than for fluctuations in a plasma wave by almost two orders of magnitude [cf. (31)]. Examining Fig. 4, we find that the RTR at $f \cong f_P$ will dominate over gyrosynchrotron radiation at $f \cong f_R$ in this model if $B < 60$ G.

As was shown in [19], when they interact with plasma turbulence, such quasi-stationary structures will also yield narrow-band burst emission. However, this requires that the energy level of the plasma turbulence not be too high ($w < 2 \times 10^{-6}$); otherwise, the continuum brightness temperature will exceed the burst brightness temperature, and it would be impossible to detect the burst component against the background of the continuum. In addition, earlier estimates have shown that the brightness temperatures of microbursts are much higher than the brightness temperature of the continuum emission.

3.6. Microburst Durations and the Period of Microburst Appearance

Radio emission can be modulated for a number of reasons [21]:

1. Modulation of background plasma and/or of fast electrons by low-frequency MHD waves.

The resonance conditions of a flux tube with frozen-in ends determine the period of a standing MHD mode, $t_A \approx L_\perp / V_A$ [22], which depends on the transverse size of the tube $L_\perp$ and the Alfvén velocity V_A. As is shown above, one mechanism yielding predominantly ordinary waves is the plasma mechanism for the generation of longitudinal waves at the upper-hybrid frequency. In this case, taking into account that

$$f^2 = (f_p^2 + f_b^2), \qquad (35)$$

we have:

$$t_A = \frac{1.3 \times 10^{-5} L_\perp \sqrt{N}}{\sqrt{f^2 - s^2 e^2 N/\pi m_e}}. \quad (36)$$

2. Periodic injection of fast electrons due to the dynamic reconnection of the magnetic field in a current sheet.

The time interval between the main spikes of reconnection processes is $t_R = kl/V_A$ [23], where l is the mean free path for an electron and k is a numerical factor (≈ 13). With (35), we obtain

$$t_R = \frac{6.34 \times 10^{-13} T_e^2}{\sqrt{\pi f^2 m_e N - e^2 N^2}\log(10^4 T_e^{2/3} N^{-1/3})}. \quad (37)$$

3. Nonlinear interaction of plasma waves among themselves and between waves and particles of a plasma [21, 22].

In this case, the oscillation period is $t_O = A/\gamma_{max}$ ($A \approx \ln 10^7$). The maximum increment of the quasi-longitudinal upper-hybrid waves for the range of reasonable physical parameters for the active solar corona reaches $\gamma_{max} = dN_e/N2\pi f_B$, $d \approx (0.5\text{–}5) \times 10^{-2}$ [10]. Again using (35), we then obtain

$$t_O = \frac{AN}{dN_e\sqrt{f^2 - e^2 N/\pi m_e}}. \quad (37)$$

4. Oscillations of a magnetic loop as an equivalent electric circuit.

The oscillation period is [24]:

$$t_C = \frac{2\pi\sqrt{\Lambda m_i N} c L_\perp^2}{I_z}\left(1 + \frac{c^2 L_\perp^2 B_z^2}{4 I_z^2}\right)^{-1/2}, \quad (38)$$

where $\Lambda = \ln\left(\frac{4L}{\pi r}\right) - \frac{7}{4}$, L is the loop length, I_z is the electric current along the loop, and B_z is the magnetic-field component along the loop axis. Assuming $I_z = cL_\perp B_z/2$ and using (35), we obtain

$$t_C = \frac{L_\perp\sqrt{2\pi e^2 N\Lambda}}{c\sqrt{\pi m_e f^2 - e^2 N}}\sqrt{\frac{m_i}{m_e}}.$$

Some results of calculations based on these models are presented in Fig. 5. We can see that three mechanisms for the generation of pulsations imply a fairly strong dependence of the period on the electron density in the emission region. The period t_R (dynamic reconnection) is more stable, and its calculated value is close to the observed period; however, here, too, we must take into account the strong dependence of the period on the electron temperature ($\propto T_e^2$). Therefore, the problem of sufficient stability of the pulsation period, both in our and other observations of microbursts, remains.

The duration of the microburst radiation can be determined either by the travel time of a single electron across a region with thickness l

$$t = l/v, \quad (38)$$

or by the duration of the interval in which fast electrons are generated. The duration of the radiation generation interval calculated with (38) is considerably shorter than the microburst duration; therefore, in this case, it must be determined by the duration of the fast-electron generation interval.

The duration of this interval can be estimated from the theory of the decay of current sheets due to the development of a sequence of plasma instabilities. The duration of the fast-electron generation interval is determined by the velocity with which the magnetic-flux reconnection region propagates along the current sheet. It was shown in [25] that the rate of decay of a current sheet is equal to the Alfvén velocity, in which case the effective length of the region of energy gain by the electrons is equal to the size L of inhomogeneities of the magnetic field [26]. Thus, the duration of the electron-generation interval is of the order of the ratio L/v_a. In this case, fast magnetoacoustic waves can trigger the excitation of current sheets and the corresponding generation of fast particles.

4. CONCLUSION

We have considered the nature of microbursts with sharp frequency structure having an equivalent bandwidth of about $\Delta f/f \leq 0.03$. While it was pointed out earlier [1] that microbursts can arise together with noise storms, the microbursts detected in our new observations were related to a flare, appearing 1.5 h before its onset. We have detected microbursts for the first time with degrees of polarization less than unity (from 0 to 0.16).

We have considered mechanisms associated with upper-hybrid waves and resonant transition radiation. The radio emission at the upper-hybrid-wave frequency always corresponds to ordinary waves. The radio emission at the second harmonic of the upper-hybrid frequency can also be polarized in the ordinary mode, but the probability of this occurring is lower than for the emission at the first harmonic.

Ordinary waves can also dominate in resonant transition radiation, but this requires the presence of well developed small-scale turbulence in the emission region. Electron density fluctuations due to the passage of a plasma wave yield less intense transition radiation than the direct conversion of plasma waves into electromagnetic waves. The generation of resonant transition radiation in quasi-stationary

structures produced by plasma waves themselves and on density fluctuations created by ion-acoustic waves is most likely. Determining the conditions for which the RTR intensity exceeds the intensity of gyrosynchrotron radiation at higher frequencies enables us to estimate the maximum magnetic-field intensity in the region in which the radio emission is generated. We have presented formulas for the RTR intensity for a given energy of plasma turbulences of various types.

Our analysis of possible mechanisms for the quasi-periodicity of the microburst radiation shows that the dynamic reconnection of a current sheet yields the most stable period, and its calculated value is close to the observed periods.

ACKNOWLEDGMENTS

The authors are grateful to G.D. Fleĭshman for helpful comments. This work was supported by the Russian Foundation for Basic Research (project nos. 02-02-17733 and 02-02-16430).

REFERENCES

1. V. M. Bogod and L. V. Yasnov, Astron. Zh. **78**, 743 (2001) [Astron. Rep. **45**, 643 (2001)].
2. V. Bogod, Q. Fu, and L. Yasnov, in *Proceeedings of the 9th Symposium of European Physical Society* (1999), p. 1041.
3. V. M. Bogod, C. Mercier, and L. V. Yasnov, J. Geophys. Res. **106** (A11), 25353 (2001).
4. L. V. Yasnov, V. M. Bogod, Q. Fu, *et al.*, Solar Phys. **215**, 343 (2003).
5. V. M. Bogod, G. N. Zhekanis, M. G. Mingaliev, *et al.*, Izv. Vyssh. Uchebn. Zaved., Radiofiz., No. 4 (2004, in press).
6. Sh. B. Akhmedov, V. M. Bogod, V. N. Borovik, *et al.*, Izv. Spets. Astrofiz. Obs. **25**, 105 (1987).
7. V. M. Bogod, G. B. Gelfreikh, F. Ch. Drago, *et al.*, astro-ph/0309444.
8. V. V. Zheleznyakov, *Radiation in Astrophysical Plasmas* (Kluwer, Dordrecht, 1996).
9. R. M. Winglee and G. A. Dulk, Astrophys. J. **307,** 808 (1986).
10. A. V. Stepanov, B. Kliem, A. Kruger, *et al.*, Astrophys. J. **524**, 961 (1999).
11. V. V. Zaitsev and A. V. Stepanov, Solar Phys. **88**, 297 (1983).
12. N. Gopalswamy, Astrophys. J. **402**, 326 (1993).
13. J. Hildebrandt and A. Kruger, in *Proc. 7th European Meeting on Solar Physics*, Ed. by G. Belvedere *et al.* (Catania Observatory, Catania, 1994), p. 181.
14. A. V. Stepanov, B. Kliem, A. Kruger, *et al.*, Solar Phys. **176**, 147 (1997).
15. K. Yu. Platonov and G. D. Fléishman, Usp. Fiz. Nauk **172**, 241 (2002) [Phys. Usp. **45**, 235 (2002)].
16. G. A. Dulk, Annu. Rev. Astron. Astrophys. **23**, 169 (1985).
17. G. A. Dulk and K. A. Marsh, Astrophys. J. **259**, 350 (1982).
18. A. G. Stupishin and L. V. Yasnov, *Achievements and Problems of Solar Radio Astronomy* (St. Peterburg State Univ., St. Petersburg, 1998), p. 118 [in Russian].
19. L. D. Landau and E. M. Lifshitz, *Electrodynamics of Continuous Media* (Gostekhizdat, Moscow, 1957; Pergamon, Oxford, 1960).
20. L. G. Genkin, L. M. Erukhimov, and B. I. Levitan, Pis'ma Astron. Zh. **15**, 167 (1989) [Sov. Astron. Lett. **15**, 71 (1989)].
21. M. J. Aschwanden, Solar Phys. **111**, 113 (1987).
22. E. R. Priest, *Solar Magnetohydrodynamics* (Reidel, Dordrecht, 1987).
23. B. Kliem, M. Karlicky, and A. O. Benz, Astron. Astrophys. **360**, 715 (2000).
24. V. V. Zaitsev, A. V. Stepanov, S. Urpo, and S. Pohjolainen, Astron. Astrophys. **337**, 887 (1998).
25. S. V. Bulanov and P. V. Sasorov, Fiz. Plazmy **4**, 746 (1978) [Sov. J. Plasma Phys. **4**, 418 (1978)].
26. S. V. Bulanov and P. V. Sasorov, Astron. Zh. **52**, 763 (1975) [Sov. Astron. **19**, 464 (1975)].

Translated by G. Rudnitskiĭ

Astronomy Reports, Vol. 49, No. 2, 2005, pp. 155–166. Translated from Astronomicheskiĭ Zhurnal, Vol. 82, No. 2, 2005, pp. 180–192.

Large-Scale Activity in Solar Eruptive Events of October–November 2003 Observed from SOHO/EIT Data

I. M. Chertok[1] and V. V. Grechnev[2]

[1] *Institute of Terrestrial Magnetism, Ionosphere and Radio Wave Propagation, Troitsk, 142190 Russia*

[2] *Institute of Solar-Terrestrial Physics, Irkutsk, 664033 Russia*

Received June 30, 2004; in final form, July 15, 2004

Abstract—Large-scale solar disturbances associated with powerful flares and coronal mass ejections (CMEs) during two passages of a grand system of three active regions in October–November 2003 are analyzed using data obtained with the SOHO/EIT EUV telescope. Dimmings (transient coronal holes) and, to a lesser extent, coronal waves (traveling emitting fronts) are studied using fixed-difference derotated images, in which a correction for the solar rotation is applied and a single heliogram preceding the event is subtracted from all subsequent heliograms. This method allows us to study difference heliograms in both the 195 Å line (with an interval of 12 min) and the various-temperature channels of 171, 195, 284, and 304 Å (with an interval of six hours). Our analysis shows, in particular, that the disturbances associated with CMEs demonstrated a global character and occupied almost the entire southern half of the disk in virtually all eruptive events during the two solar rotations. At the same time, the northern half of the disk, which had a large coronal hole, was only slightly disturbed. The dominant dimmings were observed on the disk as narrow, long features stretched mainly between three main, well-separated regions of the system and as long structures located along lines of solar latitude in the south polar sector. For repetitive events with intervals between them being not so long, the dominant dimmings demonstrated a clear homology in their forms and locations. During the very powerful event of October 28, one homologous global set of dimmings changed to another set. Many dimmings were observed to be identical or very similar in the three coronal channels and the transition-region line. It follows from the analysis that rapidly recovering global structures in the corona and transition region were involved in the eruption of running CMEs and the corresponding reconstruction of the large-scale magnetic fields. © *2005 Pleiades Publishing, Inc.*

1. INTRODUCTION

For the decay phase of the 11-year cycle, the solar activity in October–November 2003 was unprecedentedly high. A series of eleven powerful flares from X1 to X28 was recorded by the GOES satellites over fifteen days during the first passage of a system of three large active regions over the solar disk. Over two solar rotations, the white light SOHO/LASCO coronagraph detected dozens of large coronal mass ejections (CMEs), including sixteen halo CMEs with emission observed around all or nearly all of the occulting disk [1]. These eruptive events were accompanied by extreme interplanetary disturbances; a number of proton flux enhancements, in one of which the >10 MeV intensity reached 29 500 cm^{-2} s^{-1} sr^{-1} near the Earth; geomagnetic storms with $D_{st} \approx -401$ and -465 nT during the first and second rotations, respectively; deep Forbush decreases in the Galactic cosmic rays; and other associated phenomena (see the Preliminary Report and Forecast of Solar Geophysical Data at http://www.sel.noaa.gov/weekly.html and Solar-Geophysical Data at http://sgd.ngdc.noaa.gov/sgd/jsp/solarindex.jsp, as well as [2]).

This activity is of considerable interest for a variety of studies. The present work is devoted to the analysis of manifestations of solar activity on spatial scales comparable to the solar radius or even the diameter of the visible disk, mainly using data from the SOHO/EIT EUV telescope [3]. In particular, we analyze dimmings and, to a lesser extent, coronal waves associated with CMEs. Recall that dimmings, or transient coronal holes [4–13], are regions of reduced soft X-ray and EUV intensity with lifetimes varying from several hours to a day. These regions are formed after CMEs in the vicinity of eruption centers, for example, on the periphery of pre-eruptive sigmoidal structures, and can cover a significant part of the solar disk. Analysis of Yohkoh/SXT [14] and SOHO/EIT heliograms indicates provides a reason for interpretation of dimmings mainly as a result of complete or partial opening of coronal magnetic fields within these structures in the course of a CME pro-

cess, resulting in evacuation of material and a corresponding decrease of the emission intensity.

Coronal waves are emitting fronts observed ahead of developing dimmings, and can propagate with velocities of several hundred km/s [6, 15–21]. Such a wave is considered as an MHD disturbance or a shock wave, being a coronal analog for the chromospheric Moreton wave observed in Hα [22], or the result of plasma compression at the propagating boundary of a dimming, i.e., at the boundary of the region of open magnetic-field lines [23, 24].

Data and the method of their analysis are addressed in Section 2. Characteristics of large-scale activity are demonstrated in Section 3 for several major events occurred during the first and second passages of the activity complex. The results are discussed in Section 4.

2. DATA AND THE METHOD OF THEIR ANALYSIS

SOHO/EIT observations were performed routinely during the period under study. Heliograms of 1024×1024 pixels with a pixel size of $2.6''$ and a field of view of $45' \times 45'$ were recorded each 12 min in the priority 195 Å EIT channel, which is sensitive to coronal plasma with temperatures of $T_e \approx 1.5$ MK. Four times per day (near 01^h, 07^h, 13^h, and 19^h UT), heliograms were also recorded in two other coronal channels of 171 and 284 Å ($T_e \approx 1.2$ and 2.0 MK, respectively) and in 304 Å channel, which observes the HeII transition-region line ($T_e \approx 0.02$–0.08 MK) [3, 25]. The corresponding FITS files are available at http://umbra.nascom.nasa.gov/eit/eit-catalog.html.

Similarly to [26–28], we use finite-difference derotated images formed in two steps for our analysis. In the first step, the solar rotation is compensated for all heliograms observed during an event using the "rotation" to the time of a pre-selected background heliogram recorded before the event. The derotation was applied to the visible hemisphere by rotating a spherical surface at a heliocentric distance of $r \approx 1R_\odot$. In the second step, the background image was subtracted from all the subsequent derotated heliograms. Such difference images show real changes in the brightness, location, and structure of sources observed during the events. In these images, dimmings appear as dark features of decreased brightness, and a coronal wave appears as a narrow emitting front propagating from the eruption center. As an auxiliary representation, we also use running-difference images formed by subtracting each previous heliogram from the current one. Such images emphasize changes between two running heliograms, but they contain artifacts produced in formation of these images.

To distinguish dimmings and coronal waves from other structures, we constructed the difference images with a limited range of intensities, so that the brightest sources, in particular, those emitting during flares and in post-eruptive phases, usually become saturated.

The derotation method enables us to use the heliograms with six- and twelve-hour intervals to construct and analyze difference images at 195 Å and in all four EIT channels (171, 195, 284, and 304 Å) corresponding to various temperatures [27].

We analyze in this paper both powerful X-ray flares and other major eruptive events that included large CMEs and were accompanied by considerable structural changes on the visible disk. The required information and detailed data on 34 such events (22 and 12 events during the first and second rotations of the active regions, respectively) are presented at the Web-site http://helios.izmiran.troitsk.ru/lars/Chertok/0310_11/index.html. The Web site is arranged as a table containing the date, time, importance, time profiles of soft X-ray emission, and coordinates for each flare. The Web site also contains JAVASCRIPT movies of SOHO/LASCO data along with movies of original (non-subtracted) SOHO/EIT 195 Å images, fixed-difference images, and running-difference images produced from SOHO/EIT 195 Å data as well. In addition, difference images in the 171, 195, 284, and 304 Å channels, as well as Hα movies, are presented for many events. There are summary pictures for groups of events illustrating running CMEs and related large-scale activities on the disk, as well as associated space-weather disturbances in the form of proton-flux enhancements, geomagnetic storms, and Forbush decreases of the Galactic cosmic rays.

3. ANALYSIS OF ERUPTIVE EVENTS

Figure 1 presents a number of heliograms for October 28 illustrating the general situation on the disk. The SOHO/MDI continuum (Fig. 1a) and magnetogram (Fig. 1b) images show that three large active regions dominated on the disk: the western active region AR 484 (Carrington longitude $L = 354$), located slightly to the north from the solar equator at latitude N04, and AR 486 and AR 488, located $60°$–$70°$ to the east ($L = 283$ and 291) at latitudes S15 and N08, respectively.

The southern active region AR 486 had the largest area and most complex structure, and was most active in flare production. The flares with the most

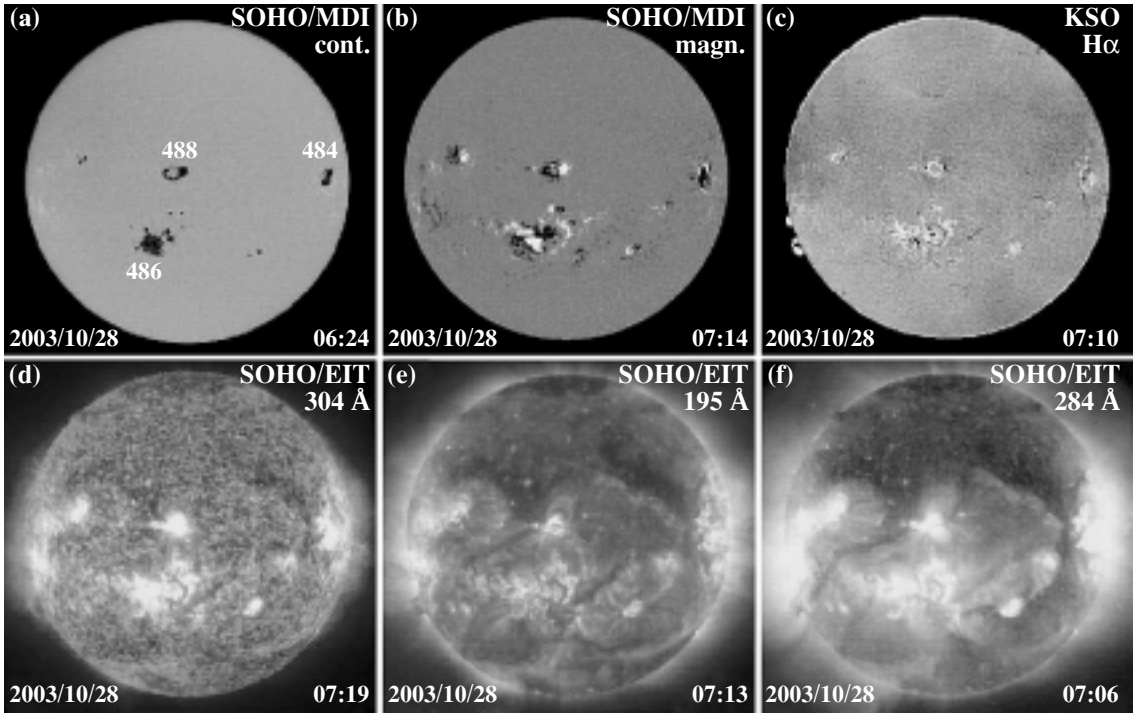

Fig. 1. Images illustrating the situation preceding the event of October 28, 2003. (a) Solar disk in white light; (b) SOHO/MDI magnetogram; (c) KSO Hα heliogram; (d) 304 Å; (e) 195 Å; and (f) 284 Å SOHO/EIT EUV heliograms. The UT is indicated at the bottom right.

powerful X-ray fluxes occurred just in this region. We shall see below that other regions located near and between the three indicated above participated in the events considered, as well as two distant regions located near the eastern limb on October 28. Despite the fact that these regions were well separated in longitude and located on opposite sides of the equator, they were connected to each other by large-scale magnetic fields and constituted one huge activity complex. The Hα heliogram (Fig. 1c) shows dark filaments mainly in and near the active regions, while there were no large filaments in the remainder of the disk.

The SOHO/EIT heliograms in the 304 Å transition-region line (Fig. 1d) and the 195 Å (Fig. 1e) and 284 Å (Fig. 1f) coronal channels also indicate a concentration of active regions in the southern hemisphere and in the near-equatorial zone of the northern hemisphere. According to the high-temperature 284 Å image (Fig. 1f), the dominant visible portion of the northern hemisphere situated to the east of the meridian of AR 484 was occupied by a large coronal hole with numerous coronal bright points and other emitting patches. Narrow extended emitting structures interchanged with sites of decreased EUV emission can be seen at 195 Å in the visible part of the southern hemisphere (Fig. 1e), especially in the polar sector.

3.1. Events during the First Rotation

Figure 2 presents SOHO/EIT difference images at 195 Å illustrating the advanced phases of large-scale disturbances for the twelve most significant eruptive events during the first rotation of the active complex. One of the first events of this type occurred in AR 484 (coordinates N08 E58) on October 19, when the other two large active regions were behind the eastern limb. This event included a 1N/X1.1 flare with its maximum at ~16:50 UT and a partial-halo CME with looplike structures mainly located above the northeastern limb. The difference movies presented at the web site referenced in Section 2 show large-scale disturbances in the form of shallow propagating dimmings and a weak coronal wave occupying almost the entire eastern half of the disk in the interval 16:43–17:22 UT. These disturbances were also observed above the eastern limb. The deepest (darkest) dimmings formed around the bright posteruptive arcade 4 and existed for several hours (Fig. 2a). In addition to the northern dimming 4–1, there was a southern transequatorial dimming 4–2 in the meridional direction. Toward the west,

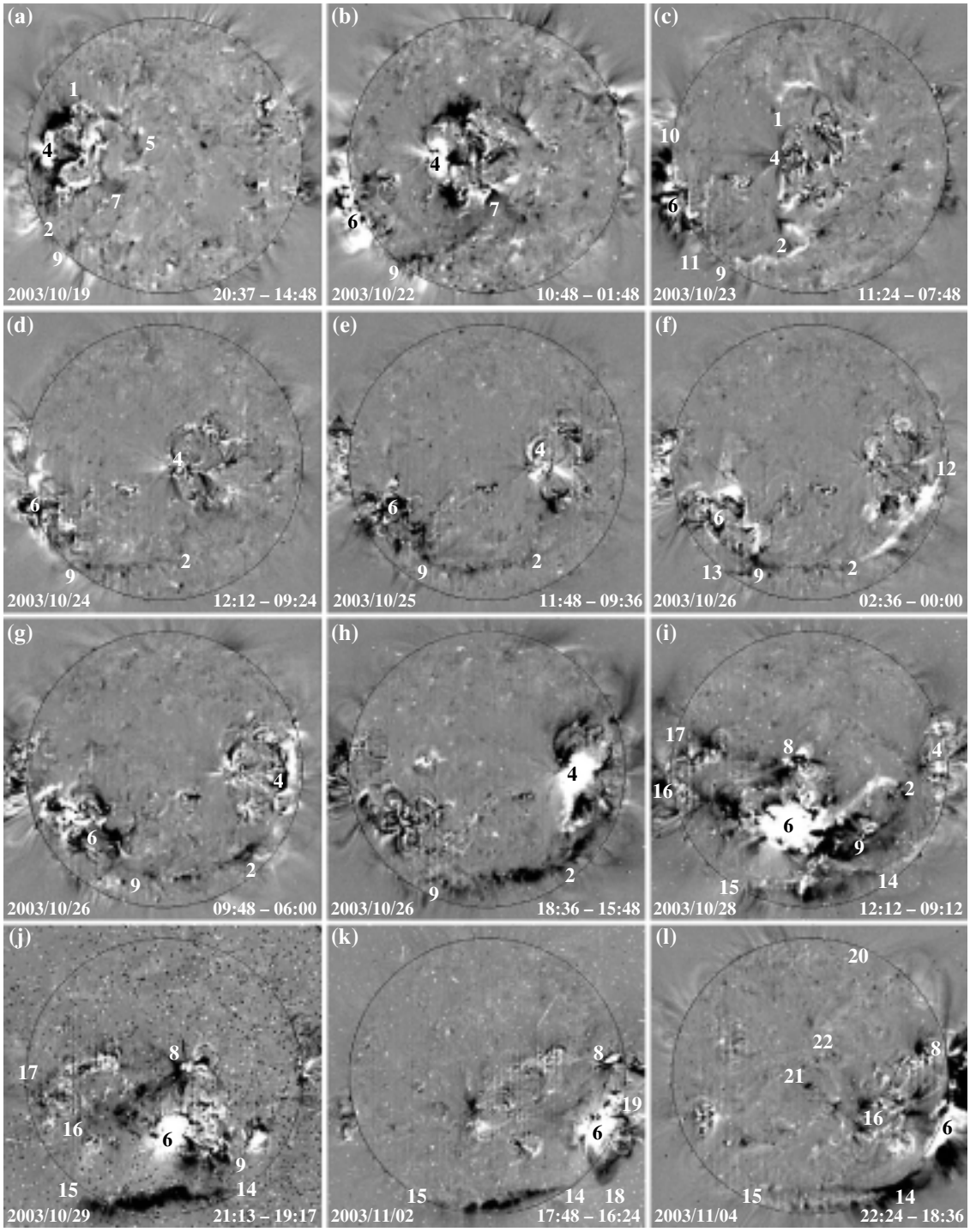

Fig. 2. Derotated SOHO/EIT fixed-difference heliograms at 195 Å showing large-scale disturbances, in particular, dimmings (dark structures), in eruptive events during the first rotation, which occurred between October 19 and November 4, 2003. The date for each event and the UTs for the studied and subtracted images are indicated at the bottom.

the dimming branches went around another large brightening to the points 5 and 7. The narrow dimming structure 7–9 extending toward the southeastern limb was already visible then; this structure played an important role in subsequent events.

A similar dimming structure arose after several eruptive events in AR 484 (N04 E24) on October 22 during the first twelve hours and in AR 496 (S21 $E >$ 90) as it rose from behind the eastern limb. An M1.7 flare at 08:30 UT and a large CME above the north-

ern, southern, and western sectors of the limb were most significant among these events. The compact central (4) and extended southeastern near-limb (6) posteruptive arcades are clearly visible in the difference image of 10:48 UT (Fig. 2b) relative to the background heliogram for 01:48 UT. The main dimmings are observed to the north, south and west of the first arcade corresponding to the CME. A narrow dimming channel 7–9 extending from the intersection of the southwestern brightening and the dimming branch directed toward the southeastern limb becomes clearly visible in this event. Among the other disturbances, this structure was also manifest after the first significant flare detected in AR 486 on October 22 (20:07 UT, M9.9, S21 E90), which was associated with a large CME.

Another powerful near-limb event including a 1B/X5.4 flare and an asymmetric, looplike CME occurred above AR 486 (S12 E88) on October 23 after 08:24 UT (Fig. 2c). This event was first accompanied by a coronal wave propagating along the eastern limb and then by a clear dimming and extended posteruptive arcade located above the large segment of the southeastern limb 10–6–11. Disturbances and various manifestations of activity also occupied the entire southeastern quadrant and the vicinity of AR 484, which was already at the center of the disk. We can see here a narrow meridional dimming 1–4–2 with a branch directed toward the southeastern limb 9 along the same structure that is clearly visible in Fig. 2b. This structure was also displayed by the broken emitting chain 9–2–4 adjacent to the dimming. There were several collimated jets and dimmings directed along the line 4–10, from the center of AR 484 toward the east. The major portion of the northeastern quadrant occupied by the coronal hole was free of significant disturbances, while the northwestern sector of the disk contained a number of dimmings and emitting elements.

Following another near-limb 1N/X1.1 flare on October 23 (20:04 UT, S17 E84) and a second CME, there was similar sympathetic activity in two well-separated regions with similar large-scale disturbances between them.

The events of October 24, when moderate C5.7 and M7.6 X-ray flares and eruptive phenomena occurred alternately in AR 484 and AR 486, clearly show that the southeastern structure indicated above represents a connection between these two regions. In particular, the EIT heliogram in Fig. 2d shows this structure as the narrow dimming 4–2–9–6 containing a segment elongated in latitude in the southeastern high-latitude sector of the disk.

The connection between AR 484 and AR 486 shown by the structure indicated above became even clearer after the eruptive events of October 25, when M1.2–M1.7 flares and a looplike CME were observed during ~05–11 UT in both the western and eastern regions. Figure 2e shows that the deepest and longest dimming, 4–2–9–6, is also well pronounced in this event and appears as a narrow arc with a length comparable to the disk diameter and with its bulge facing the high latitudes of the southern hemisphere. The distant AR 484 and AR 486 are also connected by the weaker, straight, fragmented dimming 4–6. Several additional dimmings extend from the eastern region toward the south and east.

The events of October 26 started with the eruption of a filament located to the south of AR 484. The erupted filament was clearly visible during 00:36–01:25 UT, in the form of a large loop rising above the southwestern limb in the 195 Å EIT movies, which becomes a structured CME in the LASCO coronograph data. The extended posteruptive arcade 2–12 originated at the location of the filament immediately after the eruption (Fig. 2f). It is important that this arcade was an extension of the same arc-shaped dimming 2–9–6 directed toward AR 486, which displayed appreciable activity similar to that of AR 484 during and after the eruption of the filament. The narrow dimming branch 9–13 reached the southeastern limb.

That same day, October 26, there were two more eruptive events with flares with the same classes (X1.2) and X-ray durations and with powerful halo CMEs. The first flare, with optical class 3B, occurred in the eastern active region AR 486 (S15 E44) at ~06:54 UT. However, considerable activity was observed at the same time in the western region AR 484 as well, while the extended arc-shaped southern dimming 6–9–2–4 was developing between these two regions as before (Fig 2g). The corresponding movies show the coronal wave propagating from the center of the eruption to the edge of the northeastern quadrant of the disk.

The second flare of October 26, of optical class 1N, occurred in the western region AR 484 (N02 W38) at ~18:19 UT. During this event, the dimming arc 4–2–9 became clearer and broader, in particular due to numerous dark elements directed toward high latitudes in the southern hemisphere (Fig. 2h). AR 484 displayed the bright posteruptive arcade 4. This time, significant disturbances and large-scale dimmings were also detected to the west and north of the arcade. As a whole, these structures occupied large near-limb and over-limb zones extending from the eastern limb through the southern polar sector and from the western limb toward the northern pole. At the same time, the northern part of the central zone remained almost quiet. This event was the first that was accompanied by a strong proton-flux enhancement near the Earth and "snow" in the EIT and LASCO images, due to

the impacts of energetic particles on the detectors of these instruments.

On October 27, the largest flares had classes of 2F/M2.7 and SF/M5.0, and occurred in the western and eastern regions AR 484 and AR 486, respectively, separated by less than 1 h (at 08:33 UT and 09:27 UT).

The most prominent global disturbances taking the form of large-scale dimmings and a coronal wave occurred on October 28 after 11:10 UT. These were associated with an extremely powerful flare in AR 486, which was located in the central zone of the disk at that time (S16 E08) and had an optical class of 4B and an X-ray flux exceeding X17.2—the limiting level for the GOES detectors. One of the fastest CMEs (2125 km/s in the plane of the sky), which had the form of a complete halo with uniform ring-shaped emission around the entire occulting disk, was observed during this event. It was responsible for the strongest geomagnetic storm during the first rotation. Significant flare brightenings started at approximately 10:00 UT in AR 486, also encompassing AR 488, which was located at a neighboring longitude but somewhat to the north from the solar equator (N08 E03), thus preceding the main event (see the Web-site, Fig. 1, and Fig. 2i). The brightenings in these regions were accompanied by a transequatorial dimming between them and by disturbances propagating toward the east. The coronal wave and comparatively shallow traveling dimmings, which occupied the entire northern hemisphere despite the coronal hole observed there, followed the main energy release, which occurred in AR 486 at 11:10 UT. The deepest and longest dimmings occurred throughout the southern hemisphere (Fig. 2i). The southern dimming that earlier connected AR 484 and AR 486 was transformed into the long dimming structure 6–9–2–4, which was appreciably broadened near the bright posteruptive arcade and shifted somewhat toward the north from its previous position. Another narrow dimming 6–14 originating from the eruption center reached the southern subpolar zone, where it was transformed into the high-latitude east–west dimming 14–15 which would dominate in subsequent events. During 11:24–12:12 UT, the luminous material 6–2, shown in Fig. 2i as a structure reaching the central portion of the dimming 6–9–2–4, was ejected from the arcade toward the northwest.

The northwestern and northeastern ends of the posteruptive arcade 6 were connected with the northern near-equatorial region AR 488 by transequatorial dimmings. Global disturbances in the southern hemisphere were accompanied by the two dimming strips 6–16 and 8–17 extending from both central regions toward the eastern limb.

Another powerful event with a 2B/X10 flare and very similar symmetric halo CME occurred in AR 486 (S15 W02) on the following day, October 29, at approximately 20:49 UT. In this case (Fig. 2j), the southern polar dimming 14–15 formed during the previous event dominates in the heliograms covered by "snow" due to the intense flux of accelerated particles. The western dimming adjacent to the bright posteruptive arcade is visible only in the segment 6–9. Its eastern portion is connected with the western sector of the southern polar dimming 14–15 by several meridional elements. A chain of fragmented dimmings extends along 6–16, to the east of the posteruptive arcade. The connection between the two central active regions AR 486 and AR 488 is indicated by the transequatorial dimming 6–8. The diagonal dimming 8–16 originates from the northern region, as well as the fragmented dimming structure 8–17 extending to the eastern limb.

The next three days were comparatively quiet: there were only two marked eruptive events related to flares in AR 486 on October 31 (17:20 UT, SF/C5.3, S20 W28) and November 1 (22:38 UT, 1N/M3.2, S12 W50). Appreciable, though not such large-scale, CMEs and dimmings were observed to the west of AR 486 in both cases.

The activity recommenced in the southwestern region AR 486 (S14 W56) on November 2 at ~17:25 UT, taking the form of a 2B/X8.3 flare and large CME above the western limb with an angular size of ~180°. Similarly to the event of October 29 (Fig. 2j), the southern polar dimming 14–15 along with the posteruptive arcade 6 dominated in the difference EUV heliograms (Fig. 2k). The limb dimming 18–19 was located directly above the arcade. In addition, disturbances occupied the vicinity of the northern near-equatorial region AR 488 and the entire disk sector between this region and the central meridian. To the north of AR 488, traveling disturbances similar to a coronal wave were observed near the flare maximum.

The events of November 3 were associated with activity in the northern, near-equatorial region AR 488 (N09 W80), where two flares of classes 2B/X2.7 and 2F/X3.9 occurred at 01:30 and 09:55 UT, respectively. The corresponding CMEs were observed mainly above the northwestern limb. In both cases, the EUV heliograms and CME images displayed so much snow due to energetic particles that large-scale disturbances were almost indiscernible.

An extremely powerful X-ray flare (whose class exceeded the limiting level X17.2, reaching an estimated maximum of X28) occurred on November 4 in AR 486 at ~19:53 UT, when it was situated near the

southwestern limb (S19 W83). During this event, a clear dimming was observed around the pronounced posteruptive arcade 6 above the entire southwestern limb (Fig. 2l). The looplike dimming 8–20 originating from AR 488 was observed above the northwestern limb. The angular size of the large CME corresponds to the range of position angles for near-limb dimmings. The southern subpolar dimming 14–15, split here into two extended strips, is again clearly visible. Its western end 14 approaches the main dimming above the southwestern limb, forming a single global dimming structure. Similar to the event of November 2 (Fig. 2k), disturbances occupy the entire southwestern quadrant, where two dimming channels 16–21 and 16–22 reaching the central zone of the disk can be seen.

So far we have considered the SOHO/EIT images at 195 Å. The derotation technique also enables us to construct and analyze difference heliograms in the remaining channels at 171, 284, and 304 Å using the data taken at six-hour intervals. With this interval between heliograms, we cannot assume that all events are isolated. In addition, the heliograms became full of snow due to accelerated particles one to two hours after the powerful western events that began from October 28. Allowing for these limitations, the EIT website indicated above does not present simultaneous difference images in the four lines for every event of this series.

Figure 3 shows such heliograms for two events during the first rotation. For the first of these, which occurred in the evening of October 26 (see Figs. 3a–3d, and also Fig. 2h), the difference heliograms in the three coronal channels (Figs. 3b–3d) demonstrate dimming structures that are similar in form and location; namely, the extended southern arc 4–2–9 noted above and the dimming 4–23 located to the north of the posteruptive arcade. In the transition-region line (Fig. 3a), the dimming arc displays only faint fragments, while the northern dimming shows only a portion adjacent to the eruptive center 4. The northern base 24 of the large-scale loop above the northwestern limb is a dimming in the coronal lines corresponding to low (171 Å) and moderate (195 Å) temperatures, while its southern base 25 is visible in the coronal lines corresponding to moderate and high (284 Å) temperatures. The dominant portion of the northwestern over-limb loop is observed at 284 Å. Distinct dimmings are also visible above the southwestern limb in the same channel.

Figures 3e–3h show difference heliograms for the second event on November 4 (see Fig. 4l) in the four channels for the time interval from 19^h UT on November 4 to 01^h UT on November 5. The heliograms at 171 Å (Fig. 3f) and 195 Å (Fig. 3g) display the single dimming 14–15 extended in latitude in the southern polar sector. Only the western part of this dimming is visible in the 304 Å transition-region line (Fig. 3e), while the dimming is almost invisible in the 284 Å coronal high-temperature line (Fig. 3h). However, here, and to a lesser extent at 195 Å, a large dimming is clearly visible around the posteruptive arcade 6 above the southwestern limb. The southern fragment of this dimming is also visible at 304 Å (Fig. 3e). As a whole, the over-limb dimming and the dimming extended in latitude on the disk form a single global dimming structure.

3.2. Events during the Second Rotation

The considerable activity appears to have continued when the active regions were in the invisible hemisphere, as is demonstrated by the presence of numerous large CMEs, including five halo CMEs (without corresponding effects on the visible disk), detected by the LASCO coronograph between November 6–12. The leading northern near-equatorial region AR 501 (N03, $L = 002$), which was numbered AR 484 in the first rotation, was most active during the first half of the second rotation, from November 13–20. Of the two following regions of the first rotation (AR 488 and AR 486), the northern region AR 507 (N10, $L = 295$) manifested itself on November 20, while the southern region AR 508 (S20, $L = 286$), which was near the western limb, gave rise to large events on November 27 and December 2. In general, the events observed during the second passage of the active regions were not as prominent as those during the first rotation, in terms of both flares and CMEs and accompanying phenomena in the EUV. This conclusion is supported, in particular, by Fig. 4, which presents the derotated SOHO/EIT difference heliograms at 195 Å for the developed phase of the largest eruptive events during the second rotation, analogous to Fig. 2.

Two eruptive events occurred on November 13, when the first region (AR 501) reached the eastern limb. The largest event was related to a prolonged M1.4 flare (09:29 UT, N04 E90) and a partial-halo CME containing a bright looplike front above the eastern limb. The angular size of this CME was about 180°, which corresponds to the size of the near-limb zone occupied by disturbances visible in the EUV heliogram (Fig. 4a). Large dimmings and individual emittive structures developed around the extended posteruptive arcade 1 above the limb. On the disk, large-scale disturbances in the form of fragments of a coronal wave and dimmings (for example, 1–2–3 and 1–4) adjacent to the eastern limb were observed within an arc-shaped sector, which reached the central meridian in the southern and northern polar zones.

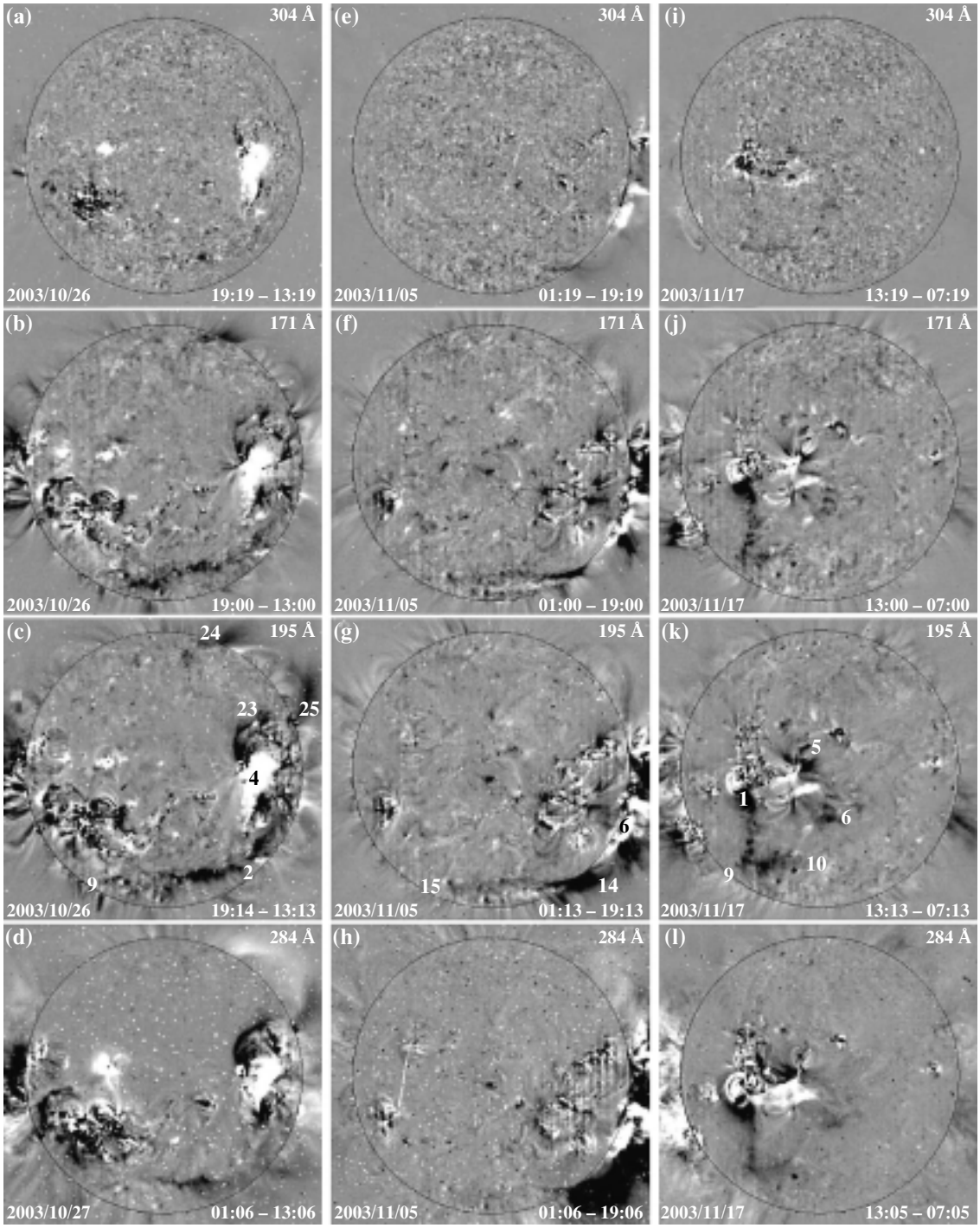

Fig. 3. Derotated SOHO/EIT difference heliograms at intervals of six hours in the four channels at 304, 171, 195, and 204 Å demonstrating dimmings in lines of various temperatures for two events during the first and one event during the second rotations: (a–d) October 28; (e–h) November 4; (i–l) November 17, 2003. Image (d) shows a difference image obtained an interval of twelve hours, since the 284 Å heliogram for October 26 19^h UT is absent.

The next marked event, which was associated with a 1N/M4.2 flare and another southeastern partial-halo CME, also occurred in AR 501 (S01 E33), on November 17 at 09:05 UT. We can see a number of additional luminous strips and arcs surrounded by the dimmings 5 and 6 located to the west of the main flare source 1 in the EUV heliogram (Fig. 4b). The main extended dimming first developed toward the

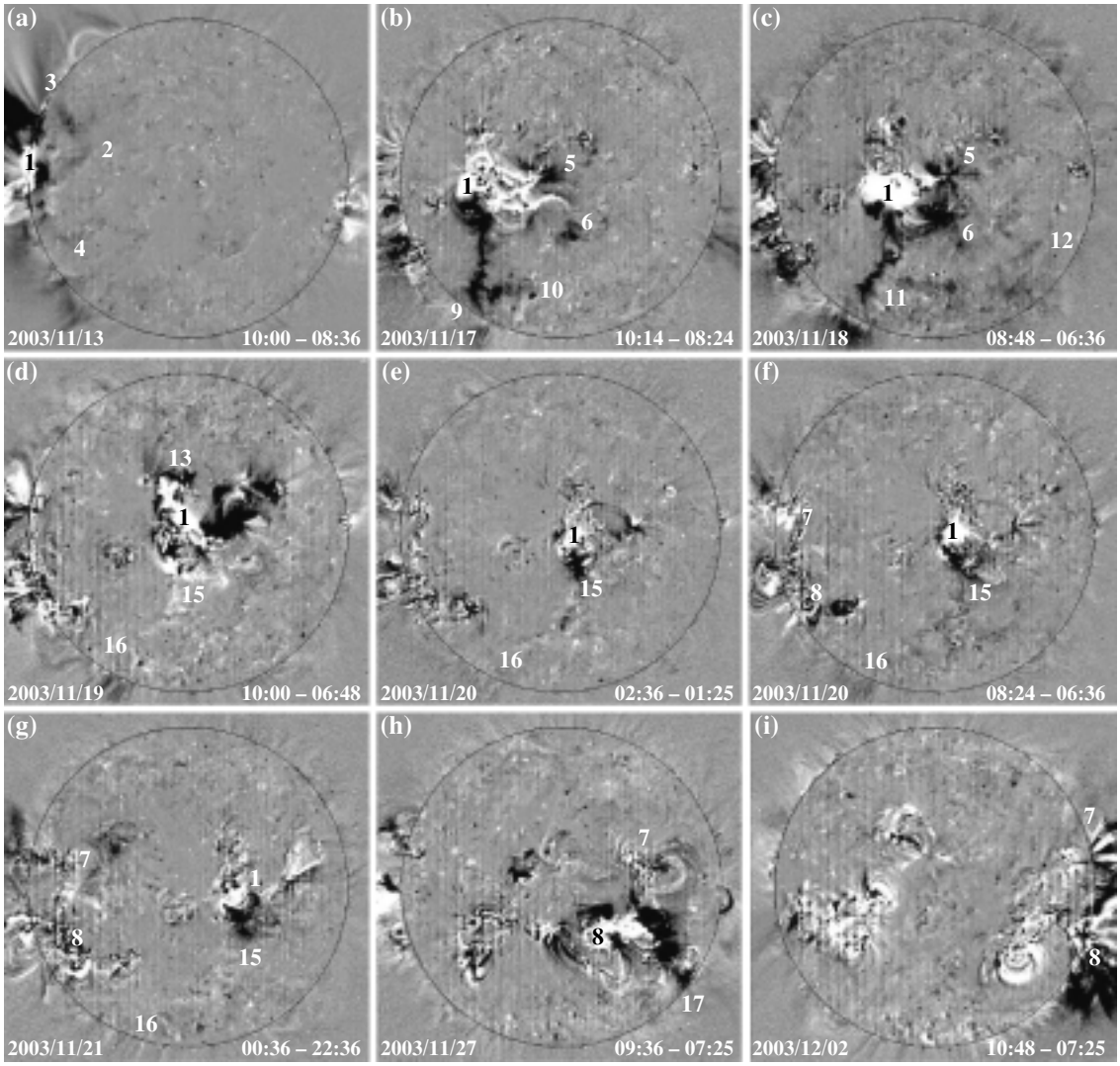

Fig. 4. Derotated SOHO/EIT difference heliograms at 195 Å displaying dimmings in eruptive events during the second rotation, observed between November 13 and December 2, 2003.

south (1–9), then was supplemented with a western branch 9–10. The corresponding movies show comparatively weak disturbances similar to coronal waves in a large zone reaching the southwestern limb. It was the western edge rather than the leading front that was brightest in this CME, probably because the western edge is an extension of the main southern dimming 1–9–10, which ejected most of the material.

The most interest is aroused by a prolonged, class 2N optical flare occurring in AR 501 (N08 E18) on November 18, which was accompanied by two M3.2 and M3.9 X-ray bursts at 07:52 and 08:31 UT, respectively; a third M4.5 X-ray burst whose maximum was observed at 10:11 UT is attributed to activity on the eastern limb. The corresponding CME also had multiple components. First, a comparatively weak CME whose brightest part was its western front, as for the CME of November 17, was observed above the southeastern limb. Then, a much brighter, faster, and larger-scale partial-halo CME developed above the southern and southwestern limb after ~08:40 UT. Despite the moderate magnitude of this flare, this event gave rise to a very strong geomagnetic storm with $D_{st} \approx -465$ nT on November 20. The CME eruption was accompanied by considerable EUV disturbances occupying almost the entire southern hemisphere (Fig. 4c). Similar to the event of November 17, the deep dimmings 5 and 6 occurred in the vicinity of the western part of the eruptive center 1. However, the main extended dimming 1–9 corresponding to the first CME was extended toward the south/southwestern limb as before. A complex set of disturbances, both stationary and traveling from the eruptive center, was observed throughout

the southeastern quadrant during several tens of minutes before the second powerful CME. Some of the fragmented and concentric arc-shaped dimmings formed here (for example 11–12) can be seen in Fig. 4c, while the coronal wave is much more visible in the movie of the running-difference images (see the website). The third large CME observed above the southeastern limb after 09:26 UT can probably be attributed to activity in an adjacent sector of the invisible hemisphere, some manifestations of which can be seen above the limb in the EIT heliograms.

In contrast to the preceding events, a 1F/C8.8 flare occurred on November 19 at 08:17 UT in the northern but not the southern part of AR 501 (N08 E01 in Fig. 4d). Accordingly, the extended posteruptive arcade 1, dimmings 13 and 14 adjacent to the arcade ends, accompanying disturbances, and a comparatively small looplike CME were observed mainly to the north of the solar equator, in the northwestern sector and above the northwestern limb. The southern hemisphere was affected only slightly, via the southeastern structure 15–16, whose position coincides with the main extended southern dimming observed in many events of the first rotation.

The same structure 1–15–16, extending from the eruptive center toward the southeastern limb and probably farther toward the southern region AR 508, which had appeared on the disk, was indicated in the form of comparatively faint, fragmented dimmings in several weak events on November 20–21 (Figs. 4e–4g). The main dimmings in these events were observed in the vicinity of the southern part of the central region AR 501 (N03 W10), where some short X-ray flares with classes between C8.8 and M9.6 occurred, together with small CMEs and weak disturbances in the southwestern sector.

One more substantial event with a C8.6 flare was observed in the northern region AR 507 (N09 E58) on November 20 at 19:29 UT. This event was accompanied by disturbances developing around this region, including transequatorial dimmings located between AR 507 and AR 508.

Two last large events of this series occurred in the southern region AR 508 only in the approach toward the southwestern limb. The first (Fig. 4h) occurred on November 27 at 08:20 UT after a prolonged SF/C9.6 flare (S14 W37) and a southwestern CME that was comparatively small in angular size. The corresponding dimmings formed around the posteruptive arcade 8, extended toward the northern region 7, and ultimately reached the southwestern limb 17.

The last event of December 2 occurred at 09:48 UT (Fig. 4i); this was a limb event (S14 W90) including a C7.2 flare with a prolonged burst of soft X-rays and a large southwestern CME. In this case, the dimmings were mainly observed above the limb, and occupied the same angular sector as the CME, extending from the northern region 7 to the southern polar zone. Against these dimmings, narrow luminous structures emerged from the vicinities of the two limb regions 7 and 8.

We can examine the dimming features of the event of November 17 (Fig. 4b) in various lines using the difference heliograms at intervals of six hours presented in Figs. 3i–3l. The main meridional dimming 1–9 and its western branch 9–10, as well as the dimmings 5 and 6 adjacent to the ribbons of emission near the eruptive center, are manifest in the same way in the three coronal channels at 171, 195, and 284 Å (Figs. 4j–4l). Moreover, comparatively faint analogs of these dimmings (in particular, of the main dimming 1–9–10) can be seen in the 304 Å heliogram (Fig. 4i).

4. DISCUSSION AND CONCLUSIONS

Analysis of SOHO/EIT EUV heliograms using compensation of the solar rotation and formation of fixed-difference derotated images has enabled us to reveal some characteristic features of the large-scale activity in a series of powerful eruptive events in October–November 2003. The main features are the global character of the activity occurring in a single system containing three large sunspot groups, and the homology of the dimmings accompanying the eruptions of numerous halo CMEs.

The global character of the activity was manifested, in particular, by the fact that the disturbances associated with the CMEs in many events occupied appreciable portions of the solar magnetosphere. Some dimmings whose spatial sizes were comparable to the radius or even the diameter of the solar disk occupied almost the entire southern hemisphere, and took the form of extended structures connecting distant active regions, including those located on opposite sides of the solar equator. The southern arc-shaped structure 4–2–9–6 (Fig. 2) was the most significant of such dimmings. These dimmings indicate that there was a magnetic connection between the regions participating in the active system observed. In addition, some events were accompanied by coronal waves, which, in contrast to dimmings, propagated mainly through the northern half of the disk. In general, the entire visible part of the global solar magnetosphere frequently became involved in the eruption of a CME.

The behavior that we call large-scale homology includes prominent dimmings formed in the same magnetic structures with considerable spatial sizes during repeated eruptive events. Homologous dimmings in transequatorial loops associated with flares and CMEs that occurred at the beginning of May

1998 were analyzed in [29]. Homologous large-scale disturbances (dimmings and coronal waves) associated with a single active region in a series of eruptive events at the end of November 2000 were described in [30]. An important feature of the series of events observed during the first rotation of the three active regions considered here is the much larger spatial size of the dimmings and their reconstruction from one set of homologous dimmings to another observed on October 28 (see Fig. 2; this reconstruction is also clearly visible in the movie presented at the EIT web site). Whereas the extended dimming arc 4–2–9–6 dominated in a number of events preceding the reconstruction, the southern subpolar dimming 14–15 elongated in latitude clearly dominated in succeeding events. During the second rotation, when the activity was not as powerful, the southern meridional dimmings 1–9 observed on November 17 and 18 (Fig. 4) can probably be considered homologous. The existence of large-scale, homologous dimmings occurring in repeated events indicates, first, that the eruption of running CMEs involves the same structures of the global solar magnetosphere and, second, that these structures have time to recover their EUV luminosity over the ten to fifteen hours between running CMEs.

Our analysis shows that, in many events, the main dimmings appear essentially identical or very similar in the three coronal lines at 171, 195, and 284 Å and the 304 Å transition-region line (compare with [27]). Here, we must take account of the fact that dimmings observed at 304 Å in the immediate vicinity of eruptive centers (active regions) may be due partially to the weakening of the emission in the coronal Si XI line, which is also in the 304 Å channel [3, 25]. A coincidence of dimmings in lines with various excitation temperatures is usually considered as a support of the idea [6, 7, 10] that such dimmings result from the outflow of plasma during a partial or complete opening of the magnetic-field structures occurring in association with CMEs. Direct evidence for an outflow of material from dimmings located near an eruptive center was found in [12] via an analysis of the Doppler shifts of several lines detected with the SOHO/CDS spectrometer [31]. However, in order to conclude that the opening of magnetic-field lines plays a dominant role, we require additional evidence, since the observations (including those discussed here) show that structures subject to dimmings frequently remain visible in emission after the CMEs, although they are much weaker. In addition, it is not entirely clear how the partial or complete opening of the magnetic-field lines in dimmings can be reconciled with the rather rapid recovery of their luminosity in homologous events. Along with coincident dimmings, there are also dimmings that differ in the different coronal lines and transition-region line [27]. This indicates that a weakening of the EUV intensities in some lines combined with the absence of such weakening or even some strengthening in other lines can be initiated by changes in the plasma temperature, for example, due to heating or MHD disturbances associated with CMEs. The formation of dimmings is probably associated with various factors, including deformations of magnetic structures, variations in the flow of chromospheric material into the coronal loops under CMEs, etc., as well as the opening of magnetic-field lines and temperature variations.

The general behavior of the activity in the events of October–November 2003 shows that we observed an unprecedented powerful global burst of activity that demonstrated a simultaneous emergence of three powerful magnetic fluxes from the photosphere and the formation of three large sunspot groups that were well-separated but connected to each other. The evolution of the local and large-scale magnetic fields of this global system gave rise to a series of analogous powerful flares and prominent CMEs, which were accompanied by homologous large-scale disturbances in the solar atmosphere. The causes of such strong fluctuations in the decay phase of the 11-year activity cycle remains unknown.

ACKNOWLEDGMENTS

The authors are grateful to the SOHO/EIT team for the data used. This work was supported by the Russian Foundation for Basic Research (project nos. 03-02-16049 and 03-02-16591), the Russian Ministry for Education and Science (Program for the Support of Leading Scientific Schools of Russia, projects NSh-477.2003.2 and NSh-1445.2003.2), and the program of the Russian Academy of Sciences "Nonstationary Processes in Astronomy."

REFERENCES

1. G. E. Brueckner, R. A. Howard, M. J. Koomen, *et al.*, Solar Phys. **162**, 357 (1995).
2. I. S. Veselovskiĭ *et al.*, Kosmich. Issled. **42**, 453 (2004) [Space Res. **35**, 433 (2004)].
3. J.-P. Delaboudinière, G. E. Artzner, J. Brunaud, *et al.*, Solar Phys. **162**, 291 (1995).
4. A. C. Sterling and H. S. Hudson, Astrophys. J. **491**, L55 (1997).
5. H. S. Hudson and D. F. Webb, in *Coronal Mass Ejections*, Ed. by N. Crooker, J. Joselyn, and J. Feynman, AGU Geophysical Monograph Series, No. 99, 27 (1997).
6. B. J. Thompson, S. P. Plunkett, J. B. Gurman, *et al.*, Geophys. Res. Lett. **25**, 2465 (1998).
7. D. M. Zarro, A. C. Sterling, B. J. Thompson, *et al.*, Astrophys. J. **520**, L139 (1999).

8. D. F. Webb, J. Atmos. Solar-Terr. Phys. **62**, 1415 (2000).
9. A. S. Sterling, J. Atmos. Solar-Terr. Phys. **62**, 1427 (2000).
10. N. Gopalswamy and B. J. Thompson, J. Atmos. Solar-Terr. Phys. **62**, 1458 (2000).
11. H. S. Hudson and E. W. Cliver, J. Geophys. Res. **106**, 25199 (2001).
12. L. K. Harra and A. C. Sterling, Astrophys. J. **561**, L215 (2001).
13. S. W. Kahler and H. S. Hudson, J. Geophys. Res. **106**, 29239 (2001).
14. S. Tsuneta, L. Acton, M. Bruner, *et al.*, Solar Phys. **136**, 37 (1991).
15. B. J. Thompson, J. B. Gurman, W. M. Neupert, *et al.*, Astrophys. J. **517**, L151 (1999).
16. A. Klassen, H. Aurass, G. Mann, *et al.*, Astron. Astrophys. **141**, 357 (2000).
17. B. J. Thompson, B. Reynolds, H. Aurass, *et al.*, Solar Phys. **193**, 161 (2000).
18. A. Warmuth, B. Vršnak, H. Aurass, *et al.*, Astrophys. J. **560**, L105 (2001).
19. D. A. Biesecker, D. C. Myers, B. J. Thompson, *et al.*, Astrophys. J. **569**, 1009 (2002).
20. N. Narukage, H. S. Hudson, T. Morimoto, *et al.*, Astrophys. J. **572**, L109 (2002).
21. J. L. Khan and H. Aurass, Astron. Astrophys. **383**, 1018 (2002).
22. G. E. Moreton and H. E. Ramsey, Publ. Astron. Soc. Pac. **72**, 357 (1960).
23. C. Delannée and G. Aulanier, Solar Phys. **190**, 107 (1999).
24. C. Delannée, Astrophys. J. **545**, 512 (2000).
25. D. Moses, F. Clette, J.-P. Delaboudinière, *et al.*, Solar Phys. **175**, 571 (1997).
26. I. M. Chertok and V. V. Grechnev, Astron. Zh. **80**, 162 (2003) [Astron. Rep. **47**, 139 (2003)].
27. I. M. Chertok and V. V. Grechnev, Astron. Zh. **80**, 1013 (2003) [Astron. Rep. **47**, 934 (2003)].
28. I. M. Chertok and V. V. Grechnev, Solar Phys. (2004, in press).
29. J. I. Khan and H. S. Hudson, Geophys. Res. Lett. **27**, 1083 (2000).
30. I. M. Chertok, V. V. Grechnev, H. S. Hudson, and N. V. Nitta, J. Geophys. Res. **109**, A02112 (2004).
31. R. A. Harrison, E. C. Sawyer, and M. K. Carter, Solar Phys. **162**, 233 (1995).

Translated by V. Badin

Astronomy Reports, Vol. 49, No. 2, 2005, pp. 79–88. Translated from Astronomicheskiĭ Zhurnal, Vol. 82, No. 2, 2005, pp. 99–109.

Interpretation of the Light Curves of "Quiescent" X-Ray Novae in a Model with a Noncollisional Interaction between the Flow and Disk. The XTE J1118+480 System

T. S. Khruzina[1], A. M. Cherepashchuk[1], D. V. Bisikalo[2], A. A. Boyarchuk[2], and O. A. Kuznetsov[2,3]

[1] *Sternberg Astronomical Institute, Universitetskiĭ pr. 13, Moscow, 119992 Russia*

[2] *Institute of Astronomy, ul. Pyatnitskaya 48, Moscow, 119017 Russia*

[3] *Keldysh Institute of Applied Mathematics, Russian Academy of Sciences, Miusskaya pl. 4, Moscow, 125047 Russia*

Received May 20, 2004; in final form, September 20, 2004

Abstract—We have analyzed the orbital light curve of the X-ray nova XTE J1118+480 in a "disk + hot line" model based on three-dimensional gas-dynamical computations of gas flows in interacting binary systems. As a result, we have been able to derive reliable parameters for the system: $i = 80^{+1}_{-4}$ degrees, $M_{BH} = 7.1^{+0.5}_{-0.1} M_\odot$, $M_{opt} = 0.39^{+0.15}_{-0.07} M_\odot$. © *2005 Pleiades Publishing, Inc.*

1. INTRODUCTION

Low-mass X-ray binaries constitute a considerable fraction of all X-ray objects in our Galaxy. The components of a low-mass X-ray binary are a relativistic primary (neutron star or probable black hole) and a late-type secondary with a mass less than $1.3 M_\odot$ (possibly a red-dwarf main-sequence star, or even a red giant). The mass transfer in such systems is usually due to Roche-lobe filling by the normal component, this star's evolutionary expansion, or a decrease of the system's orbital radius (thus leading to a decrease in the size of the secondary's Roche lobe). The stream of matter forms a fairly flat, rotating accretion disk around the compact object and, upon reaching the inner orbits of the disk, is gradually accreted onto the compact object.

X-ray novae (see, for example, [1, 2]) are a comparatively rare subtype of low-mass X-ray binary whose relativistic objects are in an unstable accretion regime. An X-ray nova usually remains in quiescence for several years, with its X-ray luminosity being $L_x \leq 10^{32}-10^{33}$ erg/s in this period. In outburst, the object's X-ray luminosity increases to $10^{37}-10^{39}$ erg/s within several days, then falls to the original level characteristic of quiescence over several months, usually following an exponential law.

The X-ray outbursts are accompanied by optical flares due to X-ray heating of the accretion disk and optical star, enabling confident identification of X-ray novae. During the system's inactive stage, absorption lines from the optical star are observed in the optical spectrum, which can be used to measure the mass function and estimate the relativistic object's mass (see, for example, the reviews [3, 4]). Masses have been measured for 18 stellar-mass black holes: 14 are in X-ray novae, while 4 are in quasi-stationary, massive X-ray binaries with OB companions [5].

The main aspects of our current understanding of the physical processes occurring in X-ray novae are described in [6–10]. More than 40 X-ray novae are known [2, 8], and two or three new objects are found each year.

Due to the optical star's comparatively low luminosity, the contribution of radiation emitted by the accretion disk to the total optical luminosity of the system in quiescence can be as high as 50–60% in the visible and near-infrared. Therefore, fitting of optical light curves of X-ray novae in quiescence should take into account both the ellipsoidal shape of the optical star [11] and the contribution of the accretion disk to the optical light of the system, as well as variability due to the radiation flux from the region where the disk interacts with the gas flow. Until recently, this interaction region was described in hot-spot models [12, 13], with energy being released during the collision of the flow with the outer edge of the disk. However, recent three-dimensional gas-dynamical computations of gas flows in interacting binary systems [14–17] have demonstrated that, in

1063-7729/05/4902-0079$26.00

self-consistent flow models, the gas flow and disk form a single morphological structure and interact without collisions. Thus, the hot-spot model should be replaced with a "hot-line" model. The hot line is an elongated hot region along the gaseous stream of matter being transferred, formed during the interaction between the flow and the matter in the circumstellar envelope. When applied to the interpretation of optical and infrared light curves of dwarf novae [18–20], the hot-line model shows certain advantages over the hot-spot model.

Application of the hot-line model to the available light curves of the X-ray nova GU Mus [21] demonstrated that this model is able to adequately describe the whole range of features of this X-ray nova's optical and IR orbital variability in quiescence, including the abnormal increase of the system's luminosity at phase $\varphi \sim 0.25$. The hot-spot model cannot reproduce the unusual shape of the light curve of GU Mus or, in some cases, the quiescent amplitude of the orbital light curves.

The current paper presents the results of our modeling of the light curve of another X-ray nova in quiescence, XTE J1118+480, using the hot-line model.

2. GENERAL PARAMETERS OF THE XTE J1118+480 SYSTEM

The X-ray nova XTE J1118+480 was discovered by the Rossi X-ray Timing Explorer All-Sky Monitor mission on March 29, 2000 [22]. The system's optical component became brighter by $\sim 6^m$, to $V = 12.9^m$, during this outburst [23]; earlier, there was a star with $V \sim 18.8^m$ at the position of the brightened object. The object has a high latitude for an X-ray nova ($b = +62.3°$). The heating of the star's atmosphere by the radiation from the compact object during the outburst was not as strong as for other soft transients: the ratio of the X-ray (~39 mCrab at 2–12 keV) and optical ($V \sim 13^m$) fluxes was ~5, two orders of magnitude below the typical value, ~500. The spectrum was rather hard during the outburst, with a photon index of $\simeq 1.8$ up to 30 keV. The object exhibited fast X-ray flashes, but no regular pulsations were detected. Later X-ray observations demonstrated the presence of strong quasi-periodic oscillations with a frequency of 0.085 Hz [24]. The shape of the spectrum suggested that the object was a transient containing a black hole. These data were confirmed by observations obtained by the ASCA satellite [25].

Cook *et al.* [26] revealed a photometric modulation with a 4.1-hour period and an amplitude of 0.055^m, which was later confirmed [27–29]. The shape and period of this modulation varied and, similar to SU UMa variables, it was attributed to superhumps developing in the system [23]. Similar phenomena have also been observed for some other low-mass X-ray binaries [30]. If we observe a normal superhump, the orbital period should be shorter than the superhump period by several percent. Earlier recording from the ASM satellite showed that the source had experienced another, more moderate, outburst in January 2000 [22]. Kuulkers [31] showed that the properties of these two outbursts were similar to those of superoutbursts in SU UMa systems, where a normal outburst immediately precedes a superoutburst that is a factor of five to ten times longer, with the time scales of the events differing by almost a factor of ~15. The first outburst of XTE J1118+480 was relatively short (~1 month), but the second was a factor of ~5 longer. A modulation with the characteristic features of a superhump was observed in the light curve during the second outburst [26]. The time interval between the two outbursts was about a month, and was longer in the X-ray than in the optical; no double outbursts of this type have been observed for other soft X-ray transients. Kuulkers [31] also showed that the time of appearance of the XTE J1118+480 superhump agreed with the time predicted, assuming that the mechanism for this modulation was activated during the first outburst.

The first optical spectroscopy of XTE J1118+480 [32] demonstrated that the spectrum was typical of soft X-ray transient sources in outburst: the Hα, Hβ, and HeII λ4686 Å emission lines were very broad and fairly weak (FWHM > 2000 km/s), with Balmer absorption lines also present. As part of his joint analysis of data from the infrared to the hard X-ray, Hynes *et al.* [33] showed that the infrared spectrum and the observations in the near-ultraviolet could be explained by emission from an optically thick disk and another, unknown source with a flat spectrum (possibly of synchrotron nature), whereas the far-ultraviolet and X-ray observations showed a power-law spectrum, as is typical of Galactic X-ray novae in quiescence.

The system returned to its preoutburst brightness ($V \simeq 19.0^m$) by the end of August 2000. Spectroscopy at that time [34, 35] yielded the system's orbital period ($P = 0.169930(4)^{\rm d}$) and a reliable radial-velocity curve whose parameters ($\gamma = -15 \pm 10$ km/s, $K_2 = 701 \pm 10$ km/s, $a_2 \sin i = 2.35(5) R_\odot$, $f_{opt}(M) = 6.1 \pm 0.3 M_\odot$, $d = 1.8(3)$ kpc) ultimately confirmed that the primary is a black hole.

The secondary's spectral type is (K7–M0)V. The red dwarf contributed 26–38% of the total flux at 5900 Å determined spectrophotometrically on various observing dates, being on average $32 \pm 6\%$. The system's quiescent spectrum displays strong and broad (FWHM ~2300–2900 km/s) Balmer emission lines

from the accretion disk, with overlapped absorption lines or bands (Mg λ5175 Å, D Na, TiO).

The optical light curve was first modeled assuming an ellipsoidal shape for the secondary [34]. The contribution from the disk was assumed to be constant and equal to 66% of the total flux. The orbital variability amplitude was best described with $i = 80°$.

Wagner *et al.* [35] constructed the system's light curve using 68 R (λ6500 Å) CCD observations. They fit the photometric light curve using a classical model consisting of a secondary that completely fills its Roche lobe and an accretion disk around the primary. Their solution yielded the orbital inclination $i = 81 \pm 2°$, disk radius in units of the distance to the inner Lagrangian point $R_d = 0.8R_{L_1}$, and temperature at the outer edge of the disk $T_d = 3906$ K. The disk contributed 76% of the total flux. Wagner *et al.* [35] attributed the narrow minimum at phase ~0.0 to a partial eclipse of the disk by the body of the red dwarf. Like McClintock *et al.* [36], they detected a small phase shift ($\Delta\varphi \sim 0.02 \pm 0.04$) between the photometric light curve and the spectroscopic data, attributing it to asymmetric radiation of the disk component.

3. THE MODEL FOR THE SYSTEM

As in the case of GU Mus, we fit the light curve of XTE J1118+480 using two different models for the propagation of the X-ray and hard ultraviolet radiation from the inner parts of the accretion disk, as is described in [37]. The first model assumes an anisotropic angular distribution for the X-ray flux, as is characteristic of black holes [38]; this radiation will lead to only insignificant heating of the secondary. The second model assumes symmetric propagation of the X-ray and hard ultraviolet radiation from the inner parts of the disk. Bochkarev *et al.* [37] demonstrated that, in the case of disk accretion onto a rotating neutron star, the radiation of the central source propagates isotropically and thus will not be reduced in the orbital plane of the system. No such central source is present in the case of a black hole, and the radiation flux from the flat accretion-disk surface is considerably anisotropic, reducing the heating of the companion. However, due to a number of instabilities that appear for high accretion rates [39], the inner regions of the disk around a black hole can become more spherical, making the accretion-disk radiation more isotropic. A model with symmetric propagation of the radiation from the inner parts of the disk provided a better fit to the light curves of the X-ray nova GU Mus, whose primary has a mass of $M_x = (6.7{-}7.6)M_\odot$ and is a reliable black-hole candidate [21].

We synthesized the theoretical light curve and solved for the parameters of the X-ray nova using a mathematical model that includes the contribution of the radiation from the shock wave outside the accretion disk. The radiation from this shock is strongest at phases $\varphi \sim 0.25$, but, depending on the conditions for its emission, it may also be observed at phases $\varphi \sim 0.75$. This model is described in detail in [23, 40], and we summarize here only its main features.

(1) The donor (secondary) fills its Roche lobe completely.

(2) The tidal deformation of the secondary is taken into account.

(3) The surface of the secondary is subdivided into 648 area elements, and the radiation intensity toward the observer is computed for each, taking into account gravitational darkening and limb darkening (using a nonlinear limb-darkening law). We take into account eclipses of the area elements on the star by the body of the star itself, as well as by the bodies of all other components in the system. Two models (isotropic and anisotropic angular distribution of the flux) are used when calculating the heating of the star's surface by hot radiation from inner parts of the disk.

(4) The primary (black hole) is spherical and located at a focus of the elliptical accretion disk. In our analysis of the light curves of X-ray novae, due to the compact object's small size, we assume that its optical and infrared luminosities are negligible and do not contribute to the total flux from the system.

(5) The elliptical accretion disk (eccentricity e) can be represented with a figure formed in the following way. The disk's lateral surface is represented by an ellipsoid with semiaxes a, b, and c. The semiaxes a and b are in the orbital plane, with $b^2 = a^2(1 - e^2)$, while the semiaxis c is normal to the orbital plane. The center of the primary is at a focus of this ellipsoid. The inner disk surfaces are described by paraboloids of revolution (see [41] for details). The orientation of the disk is given by the angle α_e between the radius vector from the center of the compact object to the disk periastron and the line connecting the components of the close binary [41]. Changes in the disk temperature are described using the relation [38]

$$T(r) = T_b \left(\frac{R_1}{r}\right)^{\alpha_g}, \qquad (1)$$

where T_b is the temperature in the inner part of the disk, near the star's equator, a distance R_1 from the star's center. In a first approximation, the parameter α_g is usually taken to be $\alpha_g = 0.75$ [38], so that each point on the disk surface emits as a blackbody. However, the observations demonstrate that the radial temperature distribution is often flatter than $\alpha_g =$

0.75. Though it is weak, heating of the disk by radiation from the secondary is also taken into account when computing the temperatures of area elements on the disk. If the high-temperature radiation from the inner regions of the accretion disk propagates isotropically, the temperature of its outer edges will also increase. This leads to additional heating of the secondary, as well.

(6) The hot line along the flow is represented as part of an ellipsoid with semiaxes a_v, b_v, and c_v, elongated toward the inner Lagrangian point, L_1. The lateral surface of this ellipsoid coincides with the tangent to the elliptical disk for any orientation of the disk; its center is in the orbital plane, inside the disk, at some distance from its edge. Only the part of this ellipsoid located outside the accretion disk is considered to form the hot line. The procedure used to construct the shape of the hot line and compute the light curve of a close binary in this model are described in [40].

The release of the shock energy occurs at the surface of the hot line, both at the shock front (i.e., on the side of the approaching flow, or the "windward" side) and on the opposite ("leeward") side, depending on the physical parameters of the interacting flows (their velocities, densities, etc.). Areas on the surface of the hot line are assumed to radiate according to a Planck law. We computed the temperature of an area element on the surface of the hot line independently for both its sides. At the point with the coordinate y_{max} (the y coordinate of the point where the flow touches the disk's lateral surface), the temperature of the matter in the hot line, $T_i(y)$, is highest on the windward side ($T^{(1)}_{max}$), whereas it is lowest at the point with the coordinate y_{min}. On the leeward side, the highest temperature of the hot line is displaced to the point with the y coordinate

$$y^{(2)}_{max} = y^{(1)}_{max} - dy,$$

where $dy > 0$. Here, the superscripts (1) and (2) refer to the hot line's windward and leeward sides, respectively.

Formally, the parameters to be estimated in this model are $q = M_1/M_2$, i, the secondary's effective temperature T_2, T_b, the eccentricity e and semimajor axis a of the disk, the parameter α_g defining the profile of the temperature variations across the disk surface, the azimuth of the disk periastron α_e, the thickness of the disk's outer edge β_d, and the parameters of the hot line: the semiaxes a_v, b_v, c_v of its ellipsoid, the highest temperatures on the surface of the line near the disk's outer edge, on its windward ($T^{(1)}_{max}$) and leeward ($T^{(2)}_{max}$) sides, and the parameters y_{min} and dy described above. The total number of parameters is 16, but we were able to fix some of the parameters thanks to the availability of additional information about the system.

(7) We searched for the parameters best fitting the system's mean light curve using the Nelder–Mead method [42]. When searching for the global minimum of the residual for each of the curves, we applied several dozen different first approximations due to the large number of independent variables, which typically leads to the existence of a number of local minima in the studied parameter range. We estimated the quality of the fit between the theoretical and observed light curves in a given model using the residual

$$\chi^2 = \sum_{j=1}^{n} \frac{(m_j^{theor} - m_j^{obs})^2}{\sigma_j^2}, \qquad (2)$$

where m_j^{theor} and m_j^{obs} are the object's theoretical and observed magnitudes at orbital phase j, σ_j^2 is the dispersion of the observations for data point j, and n is the number of normal points in the curve.

4. RESULTS OF LIGHT-CURVE MODELING FOR XTE J1118+480

We fit the R light curve of Wagner *et al.* [35] using the hot-line model described in Section 3, assuming both isotropic and anisotropic propagation of the hot radiation from the disk's inner regions, in order to, first, test the validity of the hot-line model for low-mass X-ray binaries and, second, reliably determine the orbital inclination i. As for GU Mus [21], we searched for the parameters that minimized the χ^2 residual in two stages. In the first stage, there were 16 unknown parameters, but the domains of permitted values for some of them were restricted using the results of other studies.

For example, according to the estimates of Wagner *et al.* [35], for the mass function they obtained, the component-mass ratio should be $q = M_1/M_2 > 12$, the primary's mass should be $M_1 > 6.1M_\odot$, and the expected mass of the secondary is $M_2 < 0.52M_\odot$. They used the value $q = 20$ when computing their theoretical light curve, and the amplitude of the curve was fairly insensitive to q in this range of mass ratios. Note that a similar high mass ratio follows from theoretical estimates of q using the relation $(P_{sh} - P_{orb})/P_{orb}$, where P_{sh} is the superhump period and P_{orb} is the orbital period [43, 44]. The light-curve amplitude depends much more strongly on the orbital inclination i. It follows from the observations that $i \sim 40°–80°$. Analysis of the light curve using an adequate model permits reliable estimate of i.

According to [45], the effective temperature of a (K7–M0)V red dwarf is in the range $T_2 \sim 3700–$

4150 K. When deriving the shape of the star, we assumed that its axial rotation is synchronous with the orbital motion and that it fills its critical Roche lobe completely ($\mu = 1$). The dependence of the limb-darkening coefficients on an area element's local temperature was taken into account using the tables from [46].

The largest disk radius (at the apoastron of the elliptical disk) was restricted to $R_{d,max}/\xi = 0.50$, in accordance with [34]. Our preliminary light-curve analysis shows that the accretion disk will not be eclipsed for orbital inclinations $i < 80°$ because of the small size of the red dwarf. The other unknowns include parameters describing the shape of the disk, as well as the shape and size of the hot line: (1) the eccentricity of the disk e (which we assumed did not exceed $e \sim 0.3$ in quiescence; otherwise, the changing area of the visible surface of the disk at different orbital phases would lead to considerable variations of the contribution of the disk to the total flux); (2) the thickness of the disk's outer edge β_d, which we restricted to the range characteristic of a thin disk, $\beta_d \sim 1°-2°$; (3) the azimuth of the disk periastron α_e, which was restricted to the interval $20°-180°$, since the three-dimensional gas-dynamical computations of gas flows in close binaries [47] indicate that, in quiescence, the accretion disk was turned so that the longitude of periastron is in the range $\alpha_e \sim 150°-170°$; (4) the temperature T_b of the matter in the inner parts of the disk; (5) the distance from the center of the compact object to the disk's inner edge R_1 (with $R_1/a_0 \sim 0.0002-0.0015$); (6) the parameter α_g, which determines the character of radial temperature variations of the disk ($\alpha_g \sim 0.6-0.75$); (7) the hot-line parameters a_v, b_v, and c_v; (8) the highest windward ($T^{(1)}_{max}$) and leeward ($T^{(2)}_{max}$) temperatures of the hot line; (9) the y coordinate on the axis of the hot line where the heating of the gas flow's matter by the shock drops to zero, y_{min} (i.e., where the matter has the same temperature as in the absence of the shock); and (10) the displacement dy along the axis of the hot line between the highest-temperature windward and leeward points (usually $dy/a_0 < 0.05$).

The number of normal points used to describe the shape of the mean R curve and the corresponding critical $\chi^2_{0.1,n}$ values for the $\alpha = 0.1$ significance level are $n = 25$ and $\chi^2_{0.1,25} = 34.4$; i.e., the probability that the actual parameters of the system are outside the ranges derived from the light-curve analysis is no greater than 10%.

Our computations show that the minimum residual ($\chi^2 \sim 11-12$) is not very sensitive to certain of the parameters. The confidence intervals for these parameters are very broad, and we accordingly fixed them in the second stage of our solution at the best-fit values obtained during the first stage of the solution, namely: $q = 18.0$, $T_{eff} = T_2 = 4150$ K, $R_d/\xi = 0.5$,

Parameters of the XTE J1118+480 components derived from its R light curve assuming isotropic and anisotropic propagation of the radiation from the inner parts of the accretion disk with temperature T_b and the following fixed parameters: $q = 18$, $T_{eff} = 4150$ K, $R_1 = 0.0007a_0$, $R_2 = 0.179a_0$, $R_d/\xi = 0.50$, $\beta_d = 1.3°$

Parameter	Anisotropic model	Isotropic model
i, deg	80.1	79.0
e	0.156	0.214
a/a_0	0.329	0.314
α_e, deg	175.6	108.4
a_v/a_0	0.054	0.102
b_v/a_0	0.229	0.251
c_v/a_0	0.007	0.019
$T^{(1)}_{max}$, K	21 060	23 480
$T^{(2)}_{max}$, K	14 130	14 320
$\langle T_1 \rangle$, K	10 360	16 350
$\langle T_2 \rangle$, K	8220	5585
y_{min}/a_0	0.212	0.250
y_{max}/a_0	0.172	0.228
dy/a_0	0.004	0.006
T_b, K	281 080	141 020
α_g	0.70	0.65
χ^2	11.1	10.3

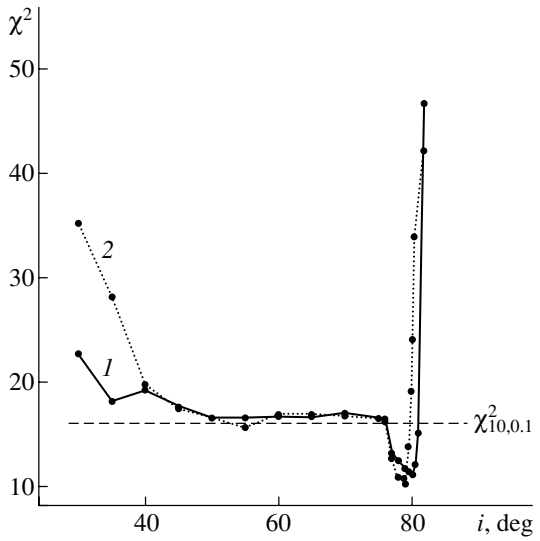

Fig. 1. Dependence of χ^2 minimized over q, T_{eff}, T_b, e, a/a_0, α_g, α_e, β_d, a_v, b_v, c_v, $T^{(1)}_{max}$, $T^{(2)}_{max}$, y_{min}, and dy on the orbital inclination i in the models with anisotropic (solid) and isotropic (dotted) propagation of the high-temperature radiation from the inner parts of the disk. The horizontal dashed line indicates the critical residual $\chi^2_{n-N+1,\alpha}$ for the $\alpha = 0.1$ significance level.

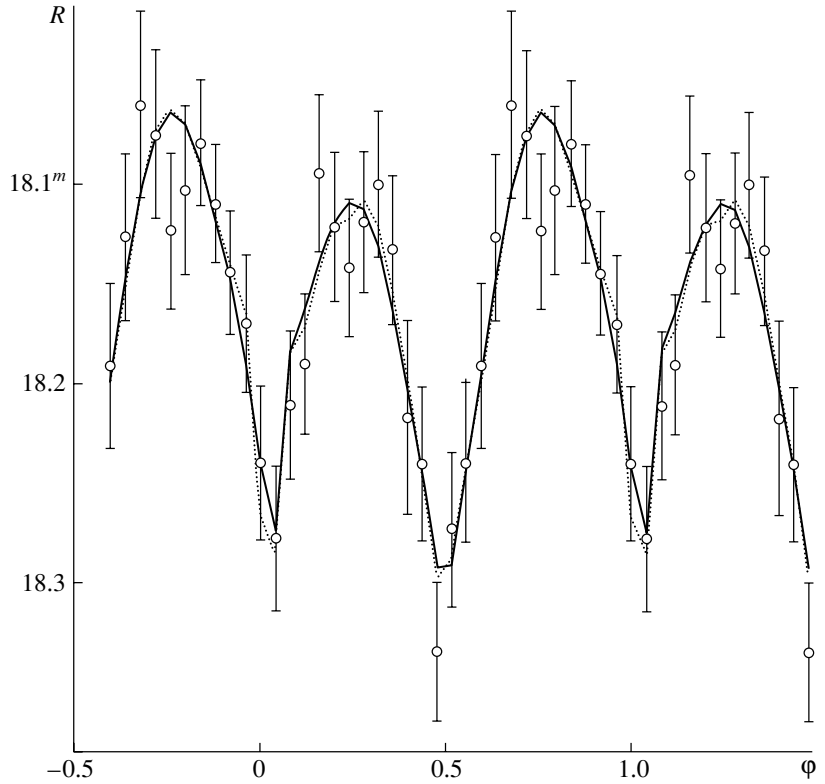

Fig. 2. Light curves computed using the tabulated parameters, obtained via computations assuming anisotropic (solid) and isotropic (dotted) propagation of hot radiation from the inner parts of the accretion disk, on the basis of the R observations of the XTE J1118+480 system.

$\beta_d = 1.3°$, $R_1 = 0.0007a_0$, $\alpha_g = 0.65$ and 0.70, respectively, for isotropic and anisotropic propagation of the hot radiation from inner parts of the disk. This reduced the number of parameters to be determined to 10. We undertook runs for various inclinations i using these parameters. For each fixed i, we minimized the residual by varying the remaining nine parameters. The dependence of the minimum χ^2 on the orbital inclination i for both models is displayed in Fig. 1: the solid and dotted curves are for anisotropic and isotropic models, respectively. Both models exhibit minimum residuals near 76°−81°. To determine the confidence interval for i, we applied the $\chi^2_{n-N+1,\alpha}$ critical level (where N is the number of parameters used during the minimization and n is the number of normal data points in the curve), equal to $\chi^2_{10,0.1} = 16.0$.

The table presents the system parameters and their corresponding uncertainties obtained for both models. We were able to derive disk and hot-spot parameters for both models satisfying the observations according to the χ^2 criterion with the $\alpha > 0.1$ significance level.

Figure 2 displays the synthetic light curves for both models obtained with the tabulated parameters: the solid and dotted curves correspond to the models with anisotropic and isotropic propagation of the radiation from the inner parts of the disk. In fact, the two curves nearly coincide. A satisfactory fit is achieved not only for the brightness amplitudes at quadrature and for the fluxes at the minima, but also for the shape of the narrow minimum at phase 1.0. In particular, the minimum is slightly displaced relative to phase 0.0 in both models. Figure 3 presents the fluxes from the system components: *1*—the compact object (this flux is zero for both models), *2*—the secondary, *3*—the elliptical accretion disk, and *4*—the fairly long hot line in the anisotropic (I) and isotropic (II) models. As in our earlier papers, the fluxes $F(X, \varphi)$ are expressed in relative units; $F(X, \varphi)$ can be translated from relative units to the usual absolute units (per unit wavelength interval) using the expression $f = Fa_0^2 \times 10^{-23}$ [erg s^{-1} cm^{-3}], where a_0 is the distance between the centers of mass of the stars in centimeters. The narrow dip at phase $\varphi \sim 0.04$ is probably due to an eclipse of the hot line by the red dwarf (partial in the isotropic model and total in the anisotropic model). This dip overlaps a symmetric minimum due to the red dwarf's ellipsoidal shape, which distorts the shape of the minimum and displaces it toward larger phases. Recall that, in [35], this minimum, which was

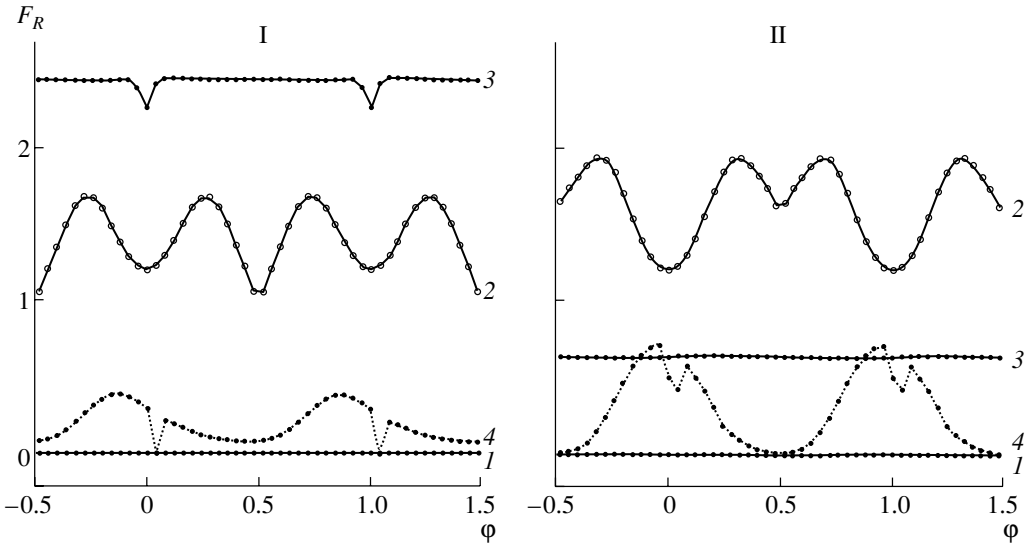

Fig. 3. Contributions to the total flux from the system components (in relative units) for anisotropic (I) and isotropic (II) propagation of the high-temperature radiation from the inner parts of the disk. Shown are radiation from (*1*) the compact object (equal to zero for both models), (*2*) the secondary, (*3*) the elliptical accretion disk, and (*4*) the long hot line. The tabulated best-fit parameters were used.

displaced by $\Delta\varphi \sim 0.02-0.04$, was explained as a partial eclipse of an asymmetrically radiating disk by the red dwarf, whereas, in [36], the displacement of the minimum was attributed to observational errors. However, a similar displacement between the spectroscopic and photometric phases has been detected for another X-ray nova, XTE J2123−058 [48].

The red dwarf's contribution to the total flux varies between 48 and 73% during the orbital motion in the isotropic model and between 29 and 40% in the anisotropic model (Fig. 4). Since spectroscopic observations indicate that the average contribution of the secondary to the total flux is $(34 \pm 8)\%$, the second model seems preferable as a description of the physical processes in the system. In the case of anisotropic propagation of the flux from the inner accretion disk, the heating of the secondary is negligible, and the minimum at phase $\varphi \sim 0.5$ is deeper than the minimum at $\varphi \sim 0.0$. In the isotropic model and for the derived best-fit orbital inclination $i = 79°$, the contribution of the disk is constant, whereas increasing the orbital inclination to $i \sim 80.1°$ in the anisotropic model gives rise to a partial eclipse of the disk at phase $\varphi \sim 0.0$. In the isotropic model, the contributions of the radiation from the disk and the hot line (at maximum light) are approximately the same, with their sum being, on average, ∼40% of the total flux (the contribution of the disk is ∼23%, while that of the hot line is ∼15−17%, on average). In the anisotropic model, the largest contribution to the total flux of the system is made by the disk (∼58%); the highest contribution made by the hot line is ∼10% of the total flux at phase $\varphi \sim 0.84$, but, in contrast to the isotropic model, the flux from the hot line is not eclipsed by the edge of the disk at phase $\varphi \sim 0.5$. The anisotropic model requires that the temperature of the inner parts of the disk be at least $T_b \sim 280\,000$ K. Assuming the energy distribution has a blackbody

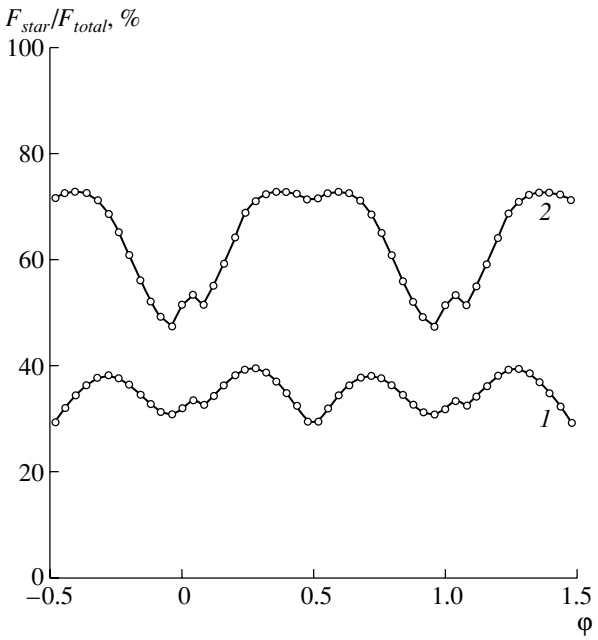

Fig. 4. Relative contribution of the red dwarf to the total flux from the system in percent for (*1*) anisotropic and (*2*) isotropic propagation of the hot radiation from the inner parts of the disk.

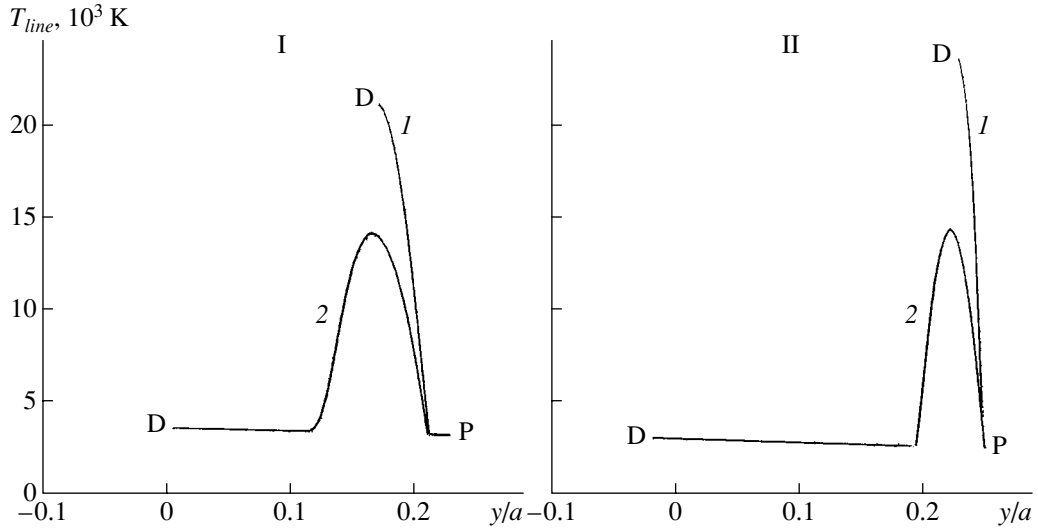

Fig. 5. Brightness-temperature distribution along the hot line on its (*1*) windward and (*2*) leeward sides, for the (I) anisotropic and (II) isotropic propagation models. The D's denote the y coordinates of the contact between the hot line's ellipsoid and the disk; while the P's denote the y coordinates of the pole of the hot-line ellipsoid.

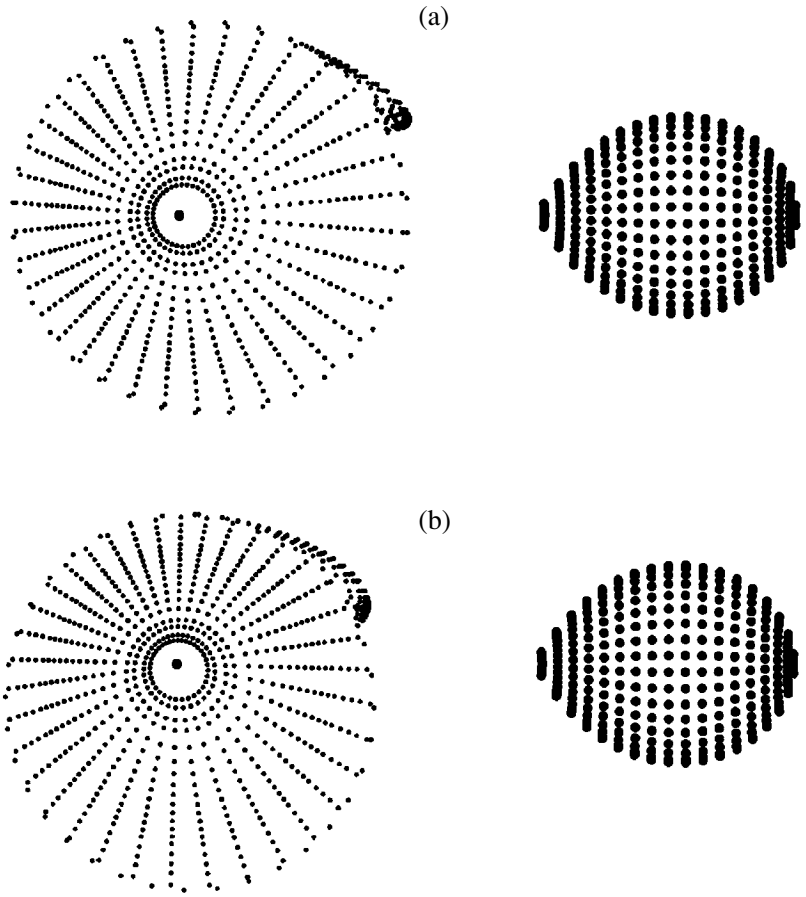

Fig. 6. Schematics of the system in its orbital plane for the parameters derived using the (a) anisotropic and (b) isotropic models.

character, its maximum for such temperatures should be at soft-X-ray energies (∼0.12 keV).

The parameter α_g ($\alpha_g \sim 0.70$) determining the rate of temperature decrease from the center to the outer parts of the disk is close to the standard value, $\alpha_g = 0.75$ [38]. The anisotropic model can easily explain the very low X-ray flux observed for the system as a consequence of the quite narrow beam of the X-ray flux relative to the orbital plane. The observed X-ray flux should also be low in the isotropic model, since the lowest residual in this model corresponds to a temperature in the central region of the disk that is half that for the anisotropic model ($T_b \sim 140\,000$ K; see the table). At such temperatures, the peak of the radiation moves to even softer X-ray energies ($E \sim$ 0.06 keV).

The highest radiation fluxes from the hot line for the two models are not as different as are the fluxes for the disk radiation. Figure 5 shows the brightness-temperature distribution along the hot line on its windward (curve *1*) and leeward (curve *2*) sides for the anisotropic (I) and isotropic (II) models. The temperatures of the hot line are higher for the isotropic that for the anisotropic model on both the windward and leeward sides. This difference is partially compensated by the larger extent of the hot line's radiating area in the anisotropic model. Figure 6 shows schematics of the system in the orbital plane for the parameters derived for the anisotropic (Fig. 6a) and isotropic (Fig. 6b) models. In the isotropic case, the hot line is transformed into a small bulge at the outer edge of the disk. In particular, this can explain the virtually total eclipse of the hot line's radiation by the edge of the disk at phases near $\varphi \sim 0.5$.

Thus, we give preference to the anisotropic model for the flux from the inner accretion disk for the X-ray nova XTE J1118+480. The anisotropy is due to the fact that the inner regions of the disk around the black hole are not spherical; the radiation propagates outward from the flat surface of the accretion disk, thereby acquiring considerable anisotropy [37]. This model can explain in a natural way the unusually low X-ray flux of this object even during outburst, as well as the low ratio of the components' X-ray and optical radiation compared to all other objects of this class.

We used the primary's mass function derived by Wagner *et al.* [35], $f(M) = 6.1(3)M_\odot$, and the values $q = 18 \pm 5$ and $i = 80^{+1}_{-4}$ degrees to estimate the masses of the components of XTE J1118+480 based on our analysis of the photometric R light curve: $M_1 = (7.0{-}7.6)M_\odot$ (or $7.1^{+0.5}_{-0.1}M_\odot$) and $M_2 = (0.32{-}0.54)M_\odot$ (or $0.39^{+0.15}_{-0.07}M_\odot$). As for GU Mus [21], the uncertainty in q was determined via an exhaustive search of possible values of this parameter with the remaining parameters fixed at their best-fit values. The derived mass of the secondary is close to the lower limit for a (K7–M0)V star, $M \sim (0.46{-}0.55)M_\odot$ [49]; the mass of the primary confirms that it is a black hole.

5. CONCLUSION

The main difficulty in deriving the masses of black holes in X-ray novae is the need to correctly take into account the contribution of gas structures to the total optical or infrared luminosity of the system, which is crucial for reliable estimation of the orbital inclination i. We have fit the orbital light curve of an X-ray nova in quiescence using a mathematical model based on modern, three-dimensional, gas-dynamical computations of gas flows in interacting binary systems [14–17], which had been demonstrated earlier to provide the most adequate fits to the main features of the optical and infrared light curves of cataclysmic and X-ray binaries [18–21]. This provides hope that we have obtained a good estimate for i, and, consequently, an accurate estimate of the black hole's mass. Our analysis of the orbital light curve of XTE J1118+480 in quiescence using the disk + hot line model yielded the parameters $i = 80^{+1}_{-4}$ degrees, $M_{BH} = 7.1^{+0.5}_{-0.1}M_\odot$, and $M_{opt} = 0.39^{+0.15}_{-0.07}M_\odot$.

Further application of our modeling techniques to the light curves of many other X-ray novae in quiescence seems a very promising approach to obtaining more reliable masses for the black holes in these systems.

REFERENCES

1. A. M. Cherepashchuk, N. A. Katysheva, T. S. Khruzina, and S. Yu. Shugarov, *Highly Evolved Close Binary Stars. Catalog* (Gordon and Breach, Brussels, 1996).
2. A. M. Cherepashchuk, Space Sci. Rev. **93**, 473 (2000).
3. A. M. Cherepashchuk, Usp. Fiz. Nauk **166**, 809 (1996) [Phys. Usp. **39**, 759 (1996)].
4. P. Charles, *Black Holes in Binaries and Galactic Nuclei,* Ed. by L. Kaper, E. P. J. van den Heuvel, and P. A. Woudt (Springer, 2001), p. 27.
5. A. M. Cherepashchuk, Usp. Fiz. Nauk **173**, 345 (2003) [Phys.–Usp. **46**, 335 (2003)].
6. Y. Tanaka and N. Shibazaki, Ann. Rev. Astron. Astrophys. **34**, 607 (1996).
7. Y. Tanaka, *Black Holes in Binaries and Galactic Nuclei,* Ed. by L. Kaper, E. P. J. van den Heuvel, and P. A. Woudt (Springer, 2001), p. 141.
8. W. Chen, C. R. Shrader, and M. Livio, Astrophys. J. **491**, 312 (1997).

9. Y. Tanaka, *Disk Instabilities in Close Binary Systems. 25 Years of the Disk-Instability Model*, Ed. by S. Mineshige and J. C. Wheeler (Univ. Acad. Press, 1999), p. 21.
10. *Basic Physics of Accretion Disks,* Ed. by S. Kato, S. Inagaki, S. Mineshige, and J. Fukue (Gordon and Breach, Kyoto, 1996).
11. V. V. Lyutyi, R. A. Syunyaev, and A. M. Cherepashchuk, Astron. Zh. **50**, 1 (1973) [Sov. Astron. **17**, 3 (1973)].
12. V. G. Gorbatskii, Astrofizika **3**, 245 (1967).
13. J. Smak, Acta Astron. **20**, 312 (1970).
14. D. V. Bisikalo, A. A. Boyarchuk, O. A. Kuznetsov, *et al.*, Astron. Zh. **74**, 880 (1997) [Astron. Rep. **41**, 786 (1997)].
15. D. V. Bisikalo, A. A. Boyarchuk, O. A. Kuznetsov, *et al.*, Astron. Zh. **74**, 889 (1997) [Astron. Rep. **41**, 794 (1997)].
16. D. V. Bisikalo, A. A. Boyarchuk, V. M. Chechetkin, *et al.*, Mon. Not. R. Astron. Soc. **300**, 39 (1998).
17. D. V. Bisikalo, A. A. Boyarchuk, O. A. Kuznetsov, *et al.*, Astron. Zh. **75**, 706 (1998) [Astron. Rep. **42**, 621 (1998)].
18. D. V. Bisikalo, A. A. Boyarchuk, O. A. Kuznetsov, *et al.*, Astron. Zh. **75**, 40 (1998) [Astron. Rep. **42**, 33 (1998)].
19. T. S. Khruzina, A. M. Cherepashchuk, D. V. Bisikalo, *et al.*, Astron. Zh. **78**, 625 (2001) [Astron. Rep. **45**, 538 (2001)].
20. T. S. Khruzina, A. M. Cherepashchuk, D. V. Bisikalo, *et al.*, Astron. Zh. **80**, 919 (2003) [Astron. Rep. **47**, 848 (2003)].
21. T. S. Khruzina, A. M. Cherepashchuk, D. V. Bisikalo, *et al.*, Astron. Rep. **80**, 675 (2003) [Astron. Rep. **47**, 621 (2003)].
22. R. Remillard, E. Morgan, D. Smith, and E. Smith, IAU Circ. No. 7389, 2 (2000).
23. M. Uemura, T. Kato, K. Matsumoto, *et al.*, Publ. Astron. Soc. Jpn. **52**, L15 (2000).
24. M. Revnivtsev, R. Sunyaev, and K. Borozdin, Astron. Astrophys. **361**, L37 (2000).
25. K. Yamaoka, Y. Ueda, T. Dotani, *et al.*, IAU Circ. No. 7427 (2000).
26. L. Cook, J. Patterson, D. Buczynski, and R. Fried, IAU Circ. No. 7397 (2000).
27. M. Uemura, T. Kato, H. Yamaoka, *et al.*, IAU Circ. No. 7390, 1 (2000).
28. J. Patterson, R. Fried, D. Harvey, *et al.*, IAU Circ. No. 7412, 2 (2000).
29. G. Dubus, R. S. J. Kim, K. Menou, *et al.*, Astrophys. J. **553**, 307 (2001).
30. D. O'Donoghue and P. A. Charles, Mon. Not. R. Astron. Soc. **282**, 191 (1996).
31. E. Kuulkers, Astron. Nachr. **322** (1), 9 (2001).
32. M. Garsia, W. Brown, M. Pahre, *et al.*, IAU Circ. No. 7392 (2000).
33. R. I. Hynes, C. W. Mauche, C. A. Haswell, *et al.*, Astrophys. J. **539**, L37 (2000).
34. J. E. McClintock, M. R. Garcia, N. Caldwell, *et al.*, Astrophys. J. **551**, L147 (2001).
35. R. M. Wagner, C. B. Foltz, T. Shahbaz, *et al.*, Astrophys. J. **556**, 42 (2001).
36. J. E. McClintock, C. A. Haswell, M. R. Garcia, *et al.*, Astrophys. J. **555**, 477 (2001).
37. N. G. Bochkarev, P. A. Syunyaev, T. S. Khruzina, *et al.*, Astron. Zh. **65**, 778 (1988) [Sov. Astron. **32**, 405 (1988)].
38. N. I. Shakura and R. A. Sunyaev, Astron. Astrophys. **24**, 337 (1973).
39. N. I. Shakura and R. A. Sunyaev, Mon. Not. R. Astron. Soc. **175**, 613 (1975).
40. T. S. Khruzina, Astron. Zh. **78**, 298 (2001) [Astron. Rep. **45**, 255 (2001)].
41. T. S. Khruzina, Astron. Zh. **77**, 510 (2000) [Astron. Rep. **44**, 446 (2000)].
42. D. M. Himmelblau, *Applied Nonlinear Programming* (McGraw-Hill, New York, 1972; Mir, Moscow, 1975), p. 163.
43. S. Mineshige, M. Hirose, and Y. Osaki, Publ. Astron. Soc. Jpn. **44**, L15 (1992).
44. L. A. Molnar and H. A. Kobulnicky, Astrophys. J. **392**, 678 (1992).
45. G. M. H. J. Habets and J. R. W. Heintze, Astron. Astrophys., Suppl. Ser. **46**, 193 (1981).
46. H. M. Al-Naimly, Astrophys. J. **53**, 181 (1978).
47. O. A. Kuznetsov, D. V. Bisikalo, A. A. Boyarchuk, *et al.*, Astron. Zh. **78**, 997 (2001) [Astron. Rep. **45**, 872 (2001)].
48. J. Casares, C. Zurita, T. Shahbaz, *et al.*, Mon. Not. R. Astron. Soc. **329**, 29 (2002).
49. C. W. Allen, *Astrophysical Quantities* (Athlone, London, 1973; Mir, Moscow, 1977), p. 295.

Translated by N. Samus'

Astronomy Reports, Vol. 49, No. 2, 2005, pp. 89–101. Translated from Astronomicheskiĭ Zhurnal, Vol. 82, No. 2, 2005, pp. 110–122.

The Evolution of Close Binary Systems with Intermediate-Mass Black Holes and Ultra-Luminous X-Ray Sources

A. V. Tutukov and A. V. Fedorova

Institute of Astronomy, ul. Pyatnitskaya 48, Moscow, 119017 Russia

Received July 10, 2004; in final form, July 15, 2004

Abstract—The results of numerical studies of the evolution of a close binary system containing a black hole with a mass of $\sim 3000 M_\odot$ are presented. Such a black hole could form in the center of a sufficiently rich and massive globular cluster. The secondary could be a main-sequence star, giant, or degenerate dwarf that fills or nearly fills its Roche lobe. The numerical simulations of the evolution of such a system take into account the magnetic wind of the donor together with the wind induced by X-ray irradiation from the primary, the radiation of gravitational waves by the system, and the nuclear evolution of the donor. Mass transfer between the components is possible when the donor fills its Roche lobe, and also via the black hole's capture of some material from the induced stellar wind. The computations show that the evolution of systems with solar-mass donors depends only weakly on the mass of the accretor. We conclude that the observed ultra-luminous X-ray sources ($L_X \gtrsim 10^{38}$ erg/s) in nearby galaxies could include accreting black holes with masses of 10^2–$10^4 M_\odot$. Three scenarios for the formation of black holes with such masses in the cores of globular clusters are considered: the collapse of superstars with the corresponding masses, the accretion of gas by a black hole with a stellar initial mass ($<100 M_\odot$), and the tidal accumulation of stellar black holes. We conclude that the tidal accumulation of stellar-mass black holes is the main scenario for the formation of intermediate-mass black holes (10^2–$10^4 M_\odot$) in the cores of globular clusters.

1. INTRODUCTION

In the last few years, compact, ultra-bright variable X-ray sources with luminosities from 10^{38} erg/s to $(2–3) \times 10^{40}$ erg/s have been discovered in nearby galaxies [1, 2]. A large fraction of these sources with luminosities lower than $\sim 10^{40}$ erg/s are probably massive close binary systems in which a stellar-mass black hole ($4–100 M_\odot$) accretes matter from a nearby companion. The donor in such a system could be a nearby Wolf–Rayet star or a main-sequence star with a mass of $4–8 M_\odot$ that fills its Roche lobe [3]. However, if the emission is emitted spherically symmetrically, the brightest of these ultra-luminous X-ray sources require the presence of black holes (BHs) with masses exceeding stellar values—10^2–$10^4 M_\odot$. Such objects are called intermediate-mass BHs, since their masses appreciably exceed the masses of stellar BHs but are much less than the masses of the BHs associated with galactic nuclei.

The presence of intermediate-mass BHs in the cores of globular clusters can be established through studies of the dynamics of the stars near the cluster core [4], or possibly via the cluster X-ray emission, if the BH has a nearby companion and efficiently accretes its mass. The X-ray luminosities of such BHs can exceed 10^{40} erg/s if the spectrum is soft (0.05–0.3 keV). Indeed, X-ray observations have revealed six BHs with masses of $700–2700 M_\odot$ in the cores of globular clusters in nearby galaxies [5] and two BHs with masses of $\sim 10^3 M_\odot$ in NGC 1313 [6]. The accretion rates in the brightest of these sources reach $10^{-5} M_\odot$/yr [5, 7]. Thus, the existence of intermediate-mass BHs in the cores of at least some fraction of globular clusters can be considered to be firmly established. It is important that some of these BHs are powerful X-ray sources, motivating numerical simulations of the evolution of close binary systems with BHs of such masses. Keeping in mind the similarity of the evolution of different globular clusters, it seems probable that the cores of many, if not all, globular clusters contain BHs with masses of $\sim 10^3 M_\odot$.

Another reason for studying the evolution of close binaries containing intermediate-mass BHs is the desire to understand the formation of the observed supermassive BHs ($M_{BH} \gtrsim 10^4 M_\odot$) in the nuclei of galaxies and quasars. By analogy with the probable cascade (hierarchical) mechanism for the formation of such supermassive BHs, it is thought that intermediate-mass BHs might be produced by the tidal deceleration of stellar BHs in the stellar fields of dense globular clusters. Likewise, tidal deceleration of

1063-7729/05/4902-0089$26.00

star clusters and galaxies in the stellar fields of massive galaxies can lead to the growth of the central BHs in the galactic nuclei to masses of $\sim 10^4$–$10^9 M_\odot$ [8]. Analysis of the dynamics of the central stars in two globular clusters indicates the possible existence of central BHs with masses of 10^2–$10^4 M_\odot$ in their cores [4, 9]. The nearly complete lack of gas in globular clusters rules out the appearance of a bright X-ray source due to the accretion of gas onto the central BH. It is possible that the tidal capture of field stars by intermediate-mass BHs in globular clusters or the collision of BHs with close binary systems could lead to the formation of fairly close binaries containing an intermediate-mass BH and a roughly solar-mass star. Theoretical information about the evolution of such systems is useful for studies of their possible observational manifestations.

To address this problem, we carried out numerical simulations of the evolution of close binaries containing a BH with a mass of $\sim 3000 M_\odot$ and a close companion, which might be a solar-mass star located at various stages of its evolution, a degenerate dwarf, or a main-sequence star with a mass of $\sim 10 M_\odot$. The procedure used for these evolutionary computations was described by us earlier in [3, 10, 11].

2. MAIN SCENARIOS FOR THE FORMATION OF INTERMEDIATE-MASS BLACK HOLES IN GLOBULAR-CLUSTER CORES

A large number of papers have been concerned with theoretical studies of scenarios for the formation of intermediate-mass BHs (10^2–$10^4 M_\odot$) and observational searches for such objects [4, 9, 12–16]). It has become clear that it is quite possible that the cores of many globular clusters—first and foremost, the most dense and massive—may contain such BHs. Taking into account the inevitable merging of the products of the evolution of massive close binaries due to the radiation of gravitational waves [17, 18] and the observed maximum masses of massive stars, ~ 150–$200 M_\odot$ [19], the upper limit for the mass of stellar BHs is close to $100 M_\odot$. Three main scenarios have been considered to explain the formation of more massive BHs. The first proposes that these BHs are produced by the evolution of supermassive stars with masses of $\sim 1000 M_\odot$, which are formed via either initial star formation or the collisional evolution of stars in globular clusters [20]. In the second scenario, BHs with initial stellar masses grow as they accrete gas. In the third scenario, intermediate-mass BHs result from the merging of stellar BHs in the core of a globular cluster due to the action of tidal friction, or alternatively from mergers of BHs as a result of the radiation of gravitational waves in binary systems [21]. Let us consider these three scenarios in more detail.

First scenario for the formation of intermediate-mass BHs. This scenario can be realized in two ways. The first way to form a supermassive ($\sim 1000 M_\odot$) star is a high accretion rate μ [22], due to a high temperature T of the protostellar gas: $\mu = 10^{-7} T^{3/2}$ [23]. To accumulate a star with a mass of $1000 M_\odot$ over the time scale for hydrogen burning in its core ($\sim 2 \times 10^6$ yr), the temperature of the gas must exceed ~ 250 K. The temperature at the center of a globular cluster during its formation may indeed be high, but the probability of forming supermassive stars in globular-cluster cores remains unclear, partly due to large uncertainty about the intensity of their stellar winds.

The second way supermassive stars can form in globular clusters is via the collisional growth of the masses of stars in the dense cluster cores [20]. Let us estimate the possibility of realizing such a collisional scenario. The conservation of energy for a superstar with mass M and radius R and with a luminosity close to the Eddington luminosity can be written

$$\frac{M}{R}\frac{dR}{dt} = \frac{dM}{dt} - 4\pi c \frac{R}{\kappa}, \qquad (1)$$

where dM/dt is the rate at which the superstar accretes stellar material, c is the speed of light, and $\kappa = 0.34$ cm^2/g is the opacity coefficient for ionized gas of solar chemical composition. In order for the size of the star to grow during the collisional accumulation of mass, the right-hand side of this expression must be positive. Such growth is necessary to accelerate the accretion of globular-cluster stars passing near the superstar.

If we define the radius of the capture cross section to be equal to the radius R of the superstar, the impact parameter for collisions r will be

$$r = (2GMR)^{1/2}/v_0, \qquad (2)$$

where G is the gravitational constant, M is the mass of the superstar, and v_0 is the mean spatial velocity of the cluster stars. The rate at which the supermassive star accretes stellar material will be

$$dM/dt = 2\pi\rho GMR/v_0. \qquad (3)$$

It is clear that the growth of the size of the star requires that the right-hand side of (1) be positive; i.e., the density of the cluster core must satisfy the condition

$$\rho > \frac{2cv_0}{3\kappa GM}. \qquad (4)$$

Assuming for the purposes of estimation $v_0 = 2 \times 10^6$ cm/s, we find the condition for the growth in the size of the superstar during its collisional accumulation of mass to be $\rho > 10^{-9}$ g/cm^3. In reality, the density of stellar material in the core of a globular

cluster is $\sim 10^{-17}$ g/cm^3, and the density in the nucleus of our Galaxy is $\sim 10^{-15}$ g/cm^3, thus ruling out the growth of the sizes of superstars via the collisional accumulation of material.

We thus conclude that a supermassive star must remain on the main sequence during the collisional accretion of stellar material. Therefore, the efficient growth of the mass of a superstar requires that the time scale for its mass to double be shorter than the time scale for hydrogen burning in its core, T_H. For a star with a mass of $\sim 1000 M_\odot$, $T_H \sim 1.7 \times 10^6$ yr [22]. Consequently, using (3), the condition that the mass of the superstar grow becomes

$$\rho > \frac{v_0}{2\pi G R T_H}. \quad (5)$$

Taking now $v_0 = 2 \times 10^6$ cm/s and $R = 50 R_\odot$ [22], we find that the collisional accumulation of $\sim 1000 M_\odot$ over the hydrogen-burning time scale requires that the density of the medium exceed $\sim 3 \times 10^{-14}$ g/cm^3. It is clear that this cannot be satisfied in either the core of a globular cluster or at the center of our Galaxy; and again, a possible additional hindrance to the growth of the masses of supermassive stars is the loss of matter via the stellar wind that is characteristic of all observed massive stars, which increases in intensity with the mass of the star, and which we have not taken into account in our estimates above.

It may seem like the estimates for the collision rate for stars in a cluster would correspond only to some "mean" star, while the collisional rate for individual stars could be appreciably higher due to random fluctuations. However, this is not the case due to the large (~ 1000) number of collisions that are required to form a superstar with a mass of $\sim 1000 M_\odot$. Let us suppose that the collisional rate for some star was twice the mean value. It is clear that the probability of this circumstance will be $\sim 2^{-1000} \simeq 10^{-300}$ for each star. However, there are only $\sim 10^6$ stars in a globular cluster, and only $\sim 10^{10}$–10^{13} in a galaxy, thus requiring an improbable deviation of the collisional rate from the mean rate in order to accumulate such a high mass. These arguments make it improbable that a star in a globular cluster or in the nucleus of a typical galaxy can substantially increase its mass via collisions with field stars.

Second scenario for the formation of intermediate-mass BHs. This scenario is based on the possibility that the masses of stellar BHs can be substantially increased via the accretion of surrounding gas. However, the role of the disk accretion of gas in the formation of intermediate-mass BHs can be constrained by observations of the X-ray background. The total X-ray flux for photon energies of 2–10 keV is $\sim 6 \times 10^{-8}$ erg cm^{-2} s^{-1} [24, 25]. If we assume that disk accretion by a BH leads to the release of an X-ray energy of $0.1c^2 \sim 10^{20}$ erg/g, then, within the cosmological horizon and with a constant accretion rate over the cosmological time scale, the local density of matter contained in a BH should be $\sim 6 \times 10^{-38}$ g/cm^3. However, the observed local density contained in BHs with masses exceeding $\sim 10^6 M_\odot$ is $\sim 1.7 \times 10^{-35}$ g/cm^3 [26]. Taking into account the X-ray flux due to the cosmological horizon slightly increases the possible fraction of accreted mass in the local density of the most massive BHs, but this fraction remains small compared to the observed density of matter contained in BHs with masses exceeding $\sim 10^6 M_\odot$.

Let us now estimate the mean density of matter contained in stellar-mass BHs. Let us assume that the evolution of all stars with masses higher than $\sim 25 M_\odot$ ends with the formation of a BH with a mass of $\sim 5 M_\odot$ [27]. We can then use the stellar initial mass function $dN \sim M^{-2.5} dM$ [23] to estimate that several percent of the mass of matter transformed into stars ultimately ends up in stellar-mass BHs (5–$100 M_\odot$). If the overall density of baryonic mass is from 2×10^{-31} g/cm^{-3} [28] to 4×10^{-30} g/cm^{-3} [26], the local density of matter contained in stellar-mass BHs turns out to be $\sim 10^{-33}$–10^{-32} g/cm^3 (or $\sim 10^7$–$10^8 M_\odot$/Mpc^3). It is clear that this density appreciably exceeds both the density in observed supermassive BHs and the density accreted by BHs of all masses. Therefore, we conclude that most of the matter contained in BHs is produced during the evolution of stars with initial masses of 25–$150 M_\odot$ [27].

Third scenario for the formation of intermediate-mass BHs. Let us now consider the last of the indicated mechanisms for the formation of intermediate-mass BHs in globular-cluster cores, in which such BHs are produced by consecutive mergers of stellar-mass BHs. The estimates of [29, 30] show that, under the action of tidal deceleration, stellar BHs "sink" to the center of their globular cluster, where they subsequently merge, radiating gravitational waves. The characteristic time scale for tidal deceleration of a star with mass m and velocity v in a medium with density ρ is given by the formula

$$T_{fr} = \frac{v^3}{4\pi G^2 m \rho \ln \lambda}, \quad (6)$$

where $\ln \lambda$ is the Coulomb logarithm. For a homogeneous equilibrium globular cluster with mass M and radius R, this time is equal to

$$T_{fr} = 3 \times 10^{10} \frac{v^3 R^3}{mM} \text{ yr}, \quad (7)$$

where v is in km/s, R is in pc, and m and M are in $M_\odot$. When $v = 30$ km/s, $R = 3$ pc, $m = 10M_\odot$, and $M = 3 \times 10^5 M_\odot$, this time is close to the Hubble time. Since this time scale is shortened as the mass of the BH is increased, it is primarily the most massive stellar BHs ($\sim 50-100 M_\odot$) that contribute to the growth in the mass of the central BH. The accumulation of mass can also be accelerated if the spatial velocities are low and the BHs are close to the cluster center. Indeed, the most massive stars that produce the most massive BHs are usually located in the central regions of their clusters. Therefore, intermediate-mass BHs ($10^2-10^4 M_\odot$) can form in the cores of even comparatively young globular clusters (ages of $\sim 10^9$ yr). Note that the last stages of the evolution of the orbits of merging BHs just before the merger are not well understood, although it is clear that the density of stars near an intermediate-mass BH must be fairly high if the components are to approach the distance necessary for the efficient radiation of gravitational waves. Ultimately, the mass of the central BH is determined by the initial mass and binding energy of the cluster. The cluster expands during the accumulation of its central BH due to gravitational deceleration [30]; the reduced density of stars slows the tidal deceleration [see (7)], and consequently also the growth of the central BH. This problem has not yet been solved numerically.

Note that only a few percent of the stellar BHs in the globular cluster participate in the formation of the central intermediate-mass BH. This follows from the fact that the masses of the central BHs in spherical stellar systems—globular clusters and galactic bulges—are only 0.001 of their masses [26]. However, according to theoretical estimates, the relative mass of stellar BHs presented above is a few percent of the total mass of stars with the observed initial mass function [8]. Therefore, the merger of only a few percent of the most massive and slowly moving stellar BHs of a globular cluster is sufficient to form a central intermediate-mass BH.

Due to the conservation of energy, the deceleration of a BH in the stellar field of a globular cluster should be accompanied by the expansion of the stellar core of the cluster. Such expansion has indeed been observed [30]. Studies of the core sizes of globular clusters in the LMC and SMC have shown that they tend to increase with cluster age, from 1 pc for globular clusters with ages of $\sim 10^7$ yr to 3 pc for those with ages of $\sim 10^{10}$ yr. It is probable that this expansion with age reflects the growth in the central intermediate-mass BHs in the cores of these clusters.

Expansion of the stellar component of a globular cluster accelerates its tidal dissipation. As a result, the clusters with the most massive central BHs may evaporate completely with time, and the formation of such BHs may represent an efficient mechanism for the disruption of their parent clusters. Another efficient mechanism for the disappearance of the central, most massive globular clusters in a galaxy is their merging with the nucleus of the galaxy as a consequence of tidal deceleration [see (7)]. The merged intermediate-mass BHs of these clusters form a supermassive BH ($>10^5 M_\odot$) in the galactic nucleus. A mechanism such as this is required to explain the formation of such BHs in the centers of galaxies such as our own, which has a BH with a mass of $\sim 2 \times 10^6 M_\odot$, as well as in the nuclei of quasars. The decrease in the number of globular clusters with time must indeed be explained, since observations have found that an increase in the cluster age by a factor of ten in the age range 10^7-10^{10} yr leads to a reduction in the number of clusters by a factor of ten [31].

Note that the realization of the accumulative scenario for the formation of intermediate-mass BHs in globular-cluster cores requires low characteristic speeds for the stellar BHs. Such speeds should be obtained by these BHs during the supernova explosions of their precursors, due to the low (~ 30 km/s) velocity with which stars leave the globular clusters. This excludes, for example, the components of close binary BHs with orbital periods shorter than $\sim 20 M_{BH}/M_\odot$ days from the list of objects that can contribute to the formation of intermediate-mass BHs, since they inevitably obtain relatively large spatial velocities during their formation due to the loss of matter from the system (the Blau effect). It is probable that the spatial velocity obtained by the product of the merger of two BHs as a consequence of the radiation of gravitational waves by the less massive BH likewise remains low ($<10-30$ km/s) [32]. This suggests that it is worthwhile to return to the question of the "kick" velocities of several hundreds of km/s that are often proposed to explain the high spatial velocities of radio pulsars. A "kick" of this magnitude during the formation of the parent objects—black holes—would lead to the evacuation of stellar BHs, and thereby the raw material for the accumulative formation of intermediate-mass BHs, from globular clusters.

Sources of material accreted onto intermediate-mass BHs in globular clusters. The detection of accreting intermediate-mass BHs—X-ray sources—in the cores of some globular clusters [5] poses the question of possible sources of material for this accretion. Observations of pulsars in the globular cluster 47 Tuc were used to estimate the density of the ionized interstellar gas in this cluster to be $\sim 10^{-25}$ g/cm^3 [33]. The corresponding total mass of gas is $0.1 M_\odot$. The gas is ionized by the cores of planetary nebulae, which are formed at a rate

of $\sim 10^{-6}$/yr; their high-surface-temperature cores have lifetimes of $\sim 10^4$ yr. The long recombination time due to the low gas density, $\sim 10^{11}$ yr, causes the gas to remain ionized. This gas is primarily lost via the cluster wind [34], which is probably supported by millisecond pulsars [35], hindering the accumulation of gas in the cluster and its subsequent accretion onto the central BH. It is obvious that the central intermediate-mass BH cannot accrete an appreciable fraction of the gas lost by planetary nebulae, since this would lead to X-ray luminosities that were high ($\sim 10^{39}$–10^{40} erg/s) compared to the observed values and masses for the central BHs that were comparable to the masses of the clusters themselves.

Of course, there is some probability that a planetary nebula forms near the BH. In this case, an appreciable fraction of its matter will be captured by the BH (say 0.001, providing a BH luminosity of $\sim 10^4 L_\odot$) during the superwind phase, when the mass-loss rate is $\sim 10^{-5} M_\odot$/yr. However, estimates show that the probability of this occurring is very small: $\sim 10^{-5}$ per cluster star. Consequently, only a few stars in a typical globular cluster can create sufficiently bright X-ray sources in this way over the cluster lifetime. Since the time for the passage of a star near the BH in the superwind phase is about 3000 yr, the total lifetimes of such X-ray sources in a single cluster will be about 10 000 yr. Therefore, we should expect to detect such X-ray sources in only one cluster among roughly a million. Consequently, this scenario for providing fuel for accretion onto intermediate-mass BHs is possible, but very inefficient.

Globular clusters orbiting the center of a gas-rich galaxy will intersect the galactic disk. Taking the velocity of the clusters relative to the disk to be 100 km/s and expressing the density of the interstellar gas in terms of the number of hydrogen atoms per cubic centimeter n_H, we can find the accretion luminosity of a BH with a mass of $10^3 M_\odot$: $L_X = n_H L_\odot$. Note that the gravitation of the parent cluster may enhance the gas density near the central BH, thereby increasing its X-ray luminosity compared to this estimate. Unfortunately, it is difficult to estimate the importance of this factor in the absence of adequate numerical simulations. Other obvious possible sources of enhanced X-ray luminosity of a cluster core include the passage of dense molecular clouds near the core and a small inclination of the orbital plane of the cluster to the plane of the gaseous disk of its galaxy. The latter provides a low relative velocity of the cluster and the matter of the gaseous galactic disk. We conclude that some globular clusters containing intermediate-mass BHs in their cores and located in the gaseous disks of their galaxies could harbor sufficiently bright X-ray sources. Adequate numerical simulations taking into account the distributions of globular clusters and gas in the galaxy are required before quantitative estimates of this scenario can be obtained.

Another way to provide a high accretion rate is via the tidal disruption of cluster stars that happen to approach the central BH. This mechanism has been invoked to explain the feeding of both BHs in quasars [36, 37] and intermediate-mass BHs [38]. Let us estimate its efficiency for a BH with a mass of $10^3 M_\odot$ in the core of a globular cluster. We will take the most widespread stars to have characteristic masses of $\sim M_\odot$ and characteristic radii of $\sim R_\odot$. In this case, the distance that brings about filling of the star's Roche lobe will be $\sim 25 R_\odot$, while, according to (2), the impact parameter required for the star to fill its Roche lobe is $\sim 4000 R_\odot$. We can now estimate the rate of disruptive collisions, taking the number of stars in the cluster to be 10^6 and the cluster radius to be 3 pc, which turns out to be $\sim 3 \times 10^{-9}$/yr. Over the cluster lifetime of $\sim 10^{10}$ yr, the total mass of cluster stars disrupted in this way will be $\sim 30 M_\odot$. Numerical simulations of the dynamical evolution of a cluster containing $\sim 10^5$ stars and a central BH with a mass of $1000 M_\odot$ confirm this estimate [39, 40]. It is clear that this amount of matter is insufficient not only to form an intermediate-mass BH, but also to appreciably increase its mass via the accretion of material from disrupted stars. However, if the rate at which this material is accreted is confined to the Eddington limit, $10^{-5} M_\odot$/yr, this amount of matter is sufficient to provide a high X-ray luminosity for such a BH over about 3×10^6 yr. During its disruption, a star is first transformed into a gaseous disk around the BH [38], which is then transformed into a decretion–accretion disk under the action of viscosity [41]. Part of the matter in this gaseous disk will be evaporated by X-ray radiation from the hot part of the disk near the BH, but some fraction of the matter from the disrupted star can be accreted onto the BH, contributing to its luminosity. We thus conclude that, judging from the total lifetime of the resulting X-ray source, we can expect to observe a central intermediate-mass BH in a luminous X-ray stage ($L_X > 10^4 L_\odot$) fueled by the accretion of matter from disrupted stars in roughly one globular cluster among several thousand. The time evolution of the X-ray flux in this situation is not well known, since this evolution can be determined only via complex simulations taking into account the evaporation of the peripheral parts of a gaseous decretion–accretion disk irradiated by X-ray radiation from its central region. The time-averaged accretion luminosity of a $\sim 1000 M_\odot$ BH due to the tidal disruption of stars is $\sim 3000 L_\odot$. However, it is likely that a large fraction of the matter will be evaporated by the X-ray radiation

of the accreting BH, in which case this luminosity estimate must be substantially lowered.

Apart from the direct tidal disruption of passing stars, the tidal capture of such stars via the excitation of pulsations is also possible [37]. The cross section for such capture is comparable to the cross section for the disruption of a passing star [42]. Therefore, roughly 30 solar-mass main-sequence stars will be captured over the lifetime of a typical globular cluster. In addition, main-sequence stars and degenerate dwarfs could be supplied to the vicinity of the central intermediate-mass BH by binaries as a result of exchange capture, and also by stellar BHs, which often have companions [27]. As a result, the intermediate-mass BH can acquire a solar-mass main-sequence or degenerate-dwarf companion. The possibility of a solar-mass (sub)giant close companion is also not ruled out, although the probability of this occurring is not very high, since the lifetime of a star in this phase is short. The appearance of more massive stars as companions to the central BH is also possible in young globular clusters [43–45]. The direct identification of the donor of the ultra-luminous X-ray source NGC 1313 X-2 with a star with a mass of ~ 15–$20 M_\odot$ [46] demonstrates this possibility.

The goal of our study is numerical investigation of the evolution of close binary systems containing an accreting intermediate-mass BH and a companion that fills or nearly fills its Roche lobe, based on the algorithm developed by us earlier [3, 10, 11, 47].

3. ACCOUNT OF THE INDUCED STELLAR WIND OF THE DONOR IN BINARIES WITH INTERMEDIATE-MASS BLACK HOLES AND THE RADIATION OF GRAVITATIONAL WAVES BY THESE SYSTEMS

Intensity of the induced stellar wind of the donor. When computing the evolution of binary systems containing BHs and neutron stars, we included the effects of both the magnetic stellar wind and the induced stellar wind (ISW) of the donor, which arises due to the irradiation of the donor by hard radiation from the accretor [47]. It is important that, when the ISW is taken into account, mass transfer becomes possible in detached phases when the donor does not fill its Roche lobe.

Our computations employed a comparatively simple, self-consistent analytical model for the ISW, based on the analytical model of Muzylev and Tutukov [49]. The mass-loss rate due to the ISW was determined by considering the balance between heating of the expanding corona of the star and radiative cooling. In addition, it is necessary to allow for the energy required to raise the stellar-wind material from the surface of the donor.

We calculated the fraction of the donor stellar wind β that is captured by the accretor in the Bondi–Hoyle approximation:

$$\beta = \frac{1}{4\alpha_{\rm ISW}^4}\left(\frac{M_1}{M_2}\frac{R_2}{a}\right)^2. \quad (8)$$

Here, M_1 is the accretor mass, M_2 is the donor mass, R_2 is the donor radius, a is the semi-major axis of the system's orbit, and

$$\alpha_{\rm ISW} = v_{\rm ISW}/(2GM_2/R_2)^{1/2} \quad (9)$$

is the ratio of the stellar-wind velocity to the escape velocity at the donor surface.

We can see that, when the ratio of the accretor and donor masses is sufficiently high ($\gtrsim 10$), the fraction of stellar-wind material β captured by the accretor becomes equal to unity. This circumstance fundamentally changes the dependence of the donor mass-loss rate via the ISW on the mass of the accretor. To illustrate this dependence, we present simple formulas obtained for the case when the donor does not fill its Roche lobe, without taking into account the energy required to raise the ISW matter from the donor surface. In this case, we can obtain comparatively simple analytical expressions for the donor mass-loss rate $\dot{M}_{\rm ISW}$ and the accretion rate onto the BH $\dot{M}_{\rm acc,ISW}$. If the accretor captures only part of the stellar-wind material ($\beta < 1$), these formulas have the form

$$\dot{M}_{\rm ISW} = 1.45\times 10^{-6}\alpha_{\rm ISW}^{-2}\frac{M_1^2}{M_2}\left(\frac{R_2}{a}\right)^4, \quad (10)$$

$$\dot{M}_{\rm acc,ISW} = 3.63\times 10^{-7}\alpha_{\rm ISW}^{-6}\frac{M_1^4}{M_2^3}\left(\frac{R_2}{a}\right)^6, \quad (11)$$

where the masses are expressed in solar units. If the accretor captures all the matter ($\beta = 1$), these formulas become

$$\dot{M}_{\rm ISW} = 5.81\times 10^{-6}\alpha_{\rm ISW}^{2}\left(\frac{R_2}{a}\right)^2 M_2, \quad (12)$$

$$\dot{M}_{\rm acc,ISW} = \dot{M}_{\rm ISW}. \quad (13)$$

Note that M_1 is absent from the expression for $\dot{M}_{\rm ISW}$; i.e., when the accretor captures all of the donor wind, the dependence of the intensity of the ISW on the mass of the accretor disappears.

Let us write these formulas for an arbitrary degree of filling of the donor Roche lobe D, which we will define as R_2/R_R, where R_R is the mean radius of the Roche lobe. If the ratio of the donor and accretor

masses is small, we can use the following simple formula for R_R [50]:

$$R_R = 0.46a\left(\frac{M_2}{M_1+M_2}\right)^{1/3}. \quad (14)$$

If M_2/M_1 is very small, this can be further simplified:

$$R_R = 0.46a\left(\frac{M_2}{M_1}\right)^{1/3}. \quad (15)$$

Formula (10) for the partial capture of the donor's wind by the accretor will have the form

$$\dot{M}_{\rm ISW} = 6.49\times10^{-8}\alpha_{\rm ISW}^{-2}D^4M_1^{2/3}M_2^{1/3}, \quad (16)$$

and formula (12) for the case of complete capture acquires the form

$$\dot{M}_{\rm ISW} = 1.23\times10^{-6}\alpha_{\rm ISW}^{2}D^2\left(\frac{M_2^{5/3}}{M_1^{2/3}}\right). \quad (17)$$

Note that, in the case of partial capture, the higher $\dot{M}_{\rm ISW}$, the higher the accretor mass; however, this dependence changes in the case of complete capture: $\dot{M}_{\rm ISW}$ decreases with increasing accretor mass (for the same degree of Roche-lobe filling by the donor). This is due to the fact that the increase in the separation between the donor and accretor as the accretor mass is increased is not compensated by an increase in the fraction of matter that is captured. Consequently, the intensity of the ISW in a close binary system with an intermediate-mass BH is essentially the same as it would be in a system with a stellar-mass BH.

We should also emphasize that, for a specified degree of Roche-lobe filling by the donor D, the orbital period of a system with $M_2 < M_1$ will essentially depend only on the radius and mass of the donor. If we use (14) for the mean radius of the Roche lobe, the period P in hours will be

$$P = 8.92D^{-3/2}\left(\frac{R_2^{3/2}}{M_2^{1/2}}\right). \quad (18)$$

Thus, the orbital periods for systems containing intermediate-mass BHs will likewise not differ appreciably from the periods of binaries with stellar-mass BHs.

The radiation of gravitational waves by the system. Systems with intermediate-mass BHs exhibit a more intense angular-momentum loss due to gravitational-wave radiation (GWR) than do systems with stellar-mass BHs. The time variations in the orbital semimajor axis a due to GWR are given by the formula [51]

$$\left(\frac{da}{dt}\right)_{\rm GWR} \approx -2\times10^{-9}\frac{M_1M_2(M_1+M_2)}{a^3}, \quad (19)$$

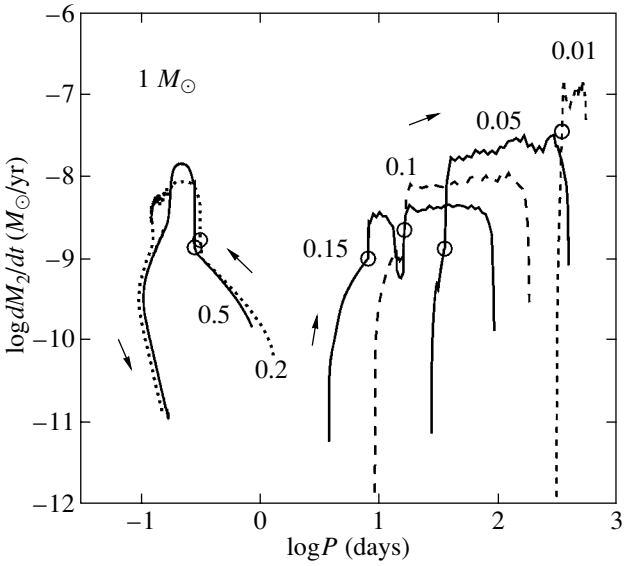

Fig. 1. Theoretical tracks of binary systems with black-hole accretors with masses of $3000M_\odot$ and main-sequence donors with masses of $1M_\odot$ in a plot of the logarithm of the orbital period vs. the logarithm of the donor mass-loss rate. The tracks were computed including the effect of the ISW. The initial degree of Roche-lobe filling by the donor D is indicated next to the tracks. The circles mark times when the donor fills its Roche lobe. The arrows indicate the direction of evolution of the system. Various types of curves are used to distinguish between the tracks.

where a and the masses are expressed in units of the radius and mass of the Sun and the time is expressed in years. When the ratio of the donor and accretor masses is small, this expression is proportional to the square of the accretor mass. Therefore, the influence of GWR is appreciably enhanced in systems with intermediate-mass BHs. As a consequence of this, the orbital periods of close systems with such BHs can be decreased, while the periods of similar systems with stellar-mass BHs will be increased.

4. RESULTS OF NUMERICAL SIMULATIONS OF THE EVOLUTION OF BINARY SYSTEMS CONTAINING INTERMEDIATE-MASS BLACK HOLES

4.1. Systems with Solar-Mass, Main-Sequence Donors

Figure 1 presents evolutionary tracks for binary systems whose accretors are $3000M_\odot$ black holes and whose donors are main-sequence stars with masses of $1M_\odot$. Donors with such masses are the most likely to be present in such systems. The tracks were computed for various initial degrees of Roche-lobe filling by the donor, D. The parameters of the

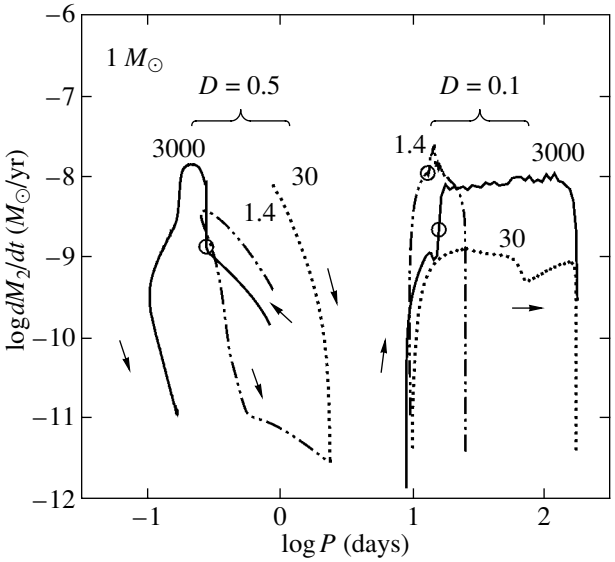

Fig. 2. Same as Fig. 1 for three types of accretor: a $3000M_\odot$ BH (solid), a $30M_\odot$ BH (dotted), and a neutron star with a mass of $1.4M_\odot$ (dot–dashed). The tracks were computed for the two initial degrees of Roche-lobe filling by the donor $D = 0.5$ and 0.1.

main computed tracks are given in the table. The computations showed that a high mass-transfer rate is achieved only for small values of D; i.e., in wide systems. In this case, the mass transfer begins when the donor has appreciably expanded as a result of its evolution. The influence of the ISW is significant only if the initial D is large, so that the donor is close to filling its Roche lobe right from the onset of the computations. (Similar results were obtained for binary systems containing stellar-mass BHs in [3].) Thus, although the donor mass-loss rate in systems containing intermediate-mass BHs is comparatively modest, the accretion rate required to produce an ultra-luminous X-ray source can be reached in wide systems (Fig. 1). Indeed, the accretion rate is higher the further the donor is from the BH at the initial time. The reason for this is the acceleration of the nuclear evolution of the donor with growth in its radius.

Figure 2 illustrates the dependence of the evolution of the system for a specified donor mass on the mass of the accretor. Tracks are shown for a solar-mass donor and three types of accretor: a BH with a mass of $3000M_\odot$, a BH with a mass of $30M_\odot$, and a neutron star with a mass of $1.4M_\odot$. The most striking differences occur in the closest systems ($D = 0.5$). In the case of the $3000M_\odot$ BH, the main driving force of the evolution is GWR. If the accretor is a neutron star, likewise, the ISW cannot compete with GWR (the neutron star does not capture all the material of the donor wind). However, if the accretor is a stellar-mass BH, the main role is played by the ISW, and the entire evolution of the system occurs in the detached stage, with the orbital period increasing as the donor's mass is reduced. One noteworthy property of the evolution of a system with a solar-mass donor is that the mass-transfer rate is limited to $\sim 10^{-7} M_\odot$/yr (Fig. 1), which corresponds to a luminosity of $\sim 10^5 L_\odot$. Observations of 174 X-ray sources in globular clusters in M87 confirm the presence of this limit for their X-ray luminosities [52].

4.2. Systems with Main-Sequence Donors with Masses of $3-10M_\odot$

Figures 3 and 4 present tracks for binary systems with more massive donors—main-sequence stars with masses of $3M_\odot$ and $10M_\odot$. Tracks for systems with a stellar-mass BH and the same donors for $D = 0.5$ are also shown for comparison. There is little difference between the tracks for the various accretors, since the main factor determining the evolution of such systems is the rapid nuclear evolution of the donor, while the influence of the ISW and GWR is comparatively small. The donor mass-loss rates in such systems are appreciably higher than in the case of a solar-mass donor. The mass-loss rate reaches the Eddington limit for a $3M_\odot$ donor and exceeds this limit for a $10M_\odot$ donor. It is likely that there is a high accretion rate onto the BH in such systems. However, if the donor mass-loss rate exceeds the Eddington limit, the formation of a common envelope is possible, which would change the character of the system's evolution.

Note that the direction of the system evolution for a donor with an initial mass of $3M_\odot$ and $D = 1$ (i.e., decreasing orbital period) is the same as that for the track for a donor with an initial mass of $1M_\odot$ (Figs. 1, 3). This is a consequence of the intense GWR for these systems. However, the evolution of an analogous close system with a $10M_\odot$ donor occurs in the opposite direction (i.e., increasing orbital period; Fig. 4). Estimates show that the limiting initial donor mass for which the time scale for GWR is comparable to the time scale for the donor's nuclear evolution is $\sim 6.5M_\odot$. A comparison of our initial mass-transfer rates for $D = 1$ with the results of Hopman *et al.* [42] shows good agreement.

4.3. Systems with Nondegenerate and Degenerate Helium Donors

Figure 5 shows tracks for systems with two types of helium donor: a nondegenerate helium star with an initial mass of $0.5M_\odot$ in the stage of core helium burning and a degenerate helium dwarf with an initial mass of $0.3M_\odot$. The computations were carried out for $D = 0.1$. Tracks for systems with stellar-mass BHs are shown as well for comparison. The

Parameters for tracks of close binary systems with a $3000M_\odot$ BH accretor

Track number	$(M_2)_0$, $M_\odot$	D	P_0, days	$\tau_{\rm UXS}$, 10^6 yr	M_{acc}, $M_\odot$	$(M_2)_f$, $M_\odot$	$m_{\rm He}$	$m_{\rm CO}$	P_f, days	t_f, 10^9 yr
1	1.0	0.50	0.85	37	0.99	0.012	0.00	0.00	0.17	0.97
2	1.0	0.20	3.37	3.8	0.99	0.011	0.00	0.00	0.15	6.55
3	1.0	0.15	5.19	1.4	0.66	0.339	0.98	0.00	90.27	12.44
4	1.0	0.10	9.53	16	0.63	0.371	0.98	0.00	177.67	12.57
5	1.0	0.05	26.96	24	0.58	0.415	0.98	0.00	377.88	12.68
6	1.0	0.01	301.39	1.9	0.15	0.846	0.54	0.00	529.38	12.71
7	3.0	1.00	0.61	80	2.99	0.013	0.00	0.00	0.17	0.88
8	3.0	0.50	1.73	22	2.51	0.488	0.98	0.00	317.80	0.66
9	3.0	0.05	54.78	1.4	1.61	1.392	0.43	0.06	563.73	0.51
10	10.0	1.00	0.80	28	8.65	1.354	0.66	0.00	233.95	0.03
11	10.0	0.50	2.25	21	4.28	2.028	0.63	0.00	260.12	0.02
12	10.0	0.05	71.11	4.7	0.60	4.442	0.49	0.09	831.01	0.05
13	0.5	0.10	0.54	2.1	0.50	0.002	1.00	0.00	0.14	8.54
14	0.3	0.10	0.05	0.61	0.17	0.001	1.00	0.00	0.01	1.03

Note: $(M_2)_0$ is the initial donor mass, D is the initial ratio of the donor radius to the mean radius of its Roche lobe, P_0 is the initial orbital period, $\tau_{\rm UXS}$ is the duration of the evolutionary stage in which the binary is an ultra-luminous X-ray source (i.e., the mass-transfer rate exceeds $1\times10^{-8}M_\odot$/yr, and the donor mass-loss rate is no more than $3\times10^{-5}M_\odot$/yr), M_{acc} is the mass accreted onto the BH during the evolution of the system, $(M_2)_f$ is the donor mass at the end of the track, $m_{\rm He}$ and $m_{\rm CO}$ are the relative masses of helium and carbon/oxygen in the donor core at the end of the track, P_f is the orbital period of the system at the end of the track, and t_f is the age of the system at the end of the track. In tracks 1–12, the donor is initially a main-sequence star, in track 13 a nondegenerate helium star, and in track 14 a degenerate helium dwarf.

differences between the tracks for systems with various accretors reduces in this case to an increase in the donor mass-loss rate with increasing accretor mass, since the main role in the evolution of these systems is played by GWR, which is more intense for intermediate-mass BHs. The differences in the intensity of the GWR lead to differences in the tracks for the system with a nondegenerate helium star donor. As the intensity of the ISW is reduced to $\sim10^{-12}M_\odot$/yr, GWR again becomes the leading factor determining the evolution of the system, and the orbital period begins to decrease (Fig. 5).

It is obvious that a high accretion rate is produced in such systems, but over a short time. In addition, due to the substantial excess of the mass-transfer rate for a system with a degenerate dwarf and intermediate-mass BH over the Eddington limit, the formation of a common envelope or destruction of the dwarf are possible, which would change the character of the system's evolution.

4.4. Influence of the ISW on the System's Evolution

The computational results show that the ISW plays an important role in the evolution of close binaries with solar-mass donors and $D\gtrsim0.1$. This raises the question of the influence of the ISW on the evolution of these systems. In the absence of a fully adequate theory for the ISW, we can only test how variations in the ISW intensity affect the evolution of the systems considered. For this purpose, we carried out computations for a number of tracks with various ISW intensities: decreased by a factor of ten and increased by factors of three and ten compared to the standard value. The initial mass of the donor was one solar mass.

Figure 6 shows the results of these computations. The numerical simulations demonstrate that neither decreasing the ISW intensity by a factor of ten nor increasing it by a factor of three significantly change the character of the late stages of the system's evolution. However, increasing the ISW intensity by a factor of ten leads to appreciable changes in the track: the

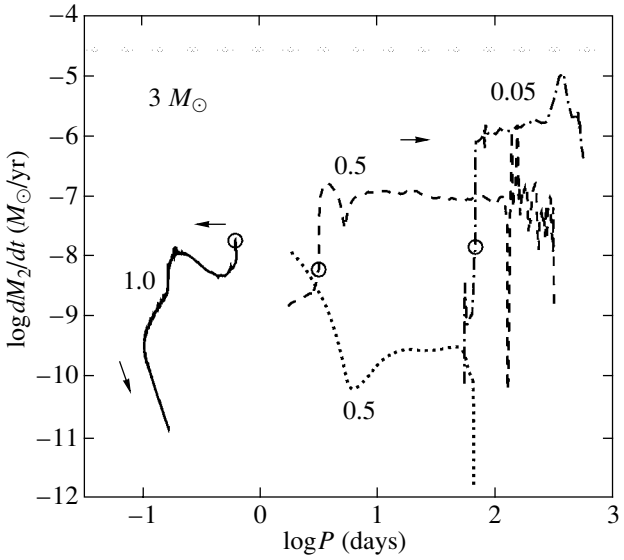

Fig. 3. Same as Fig. 1 for a $3M_\odot$ main-sequence donor (solid, dashed, and dot–dashed curves). The dotted curve shows the track for a system with a stellar mass BH ($30M_\odot$) and $D = 0.5$ for comparison. The thick gray line shows the Eddington limit for accretion onto a $3000M_\odot$ BH.

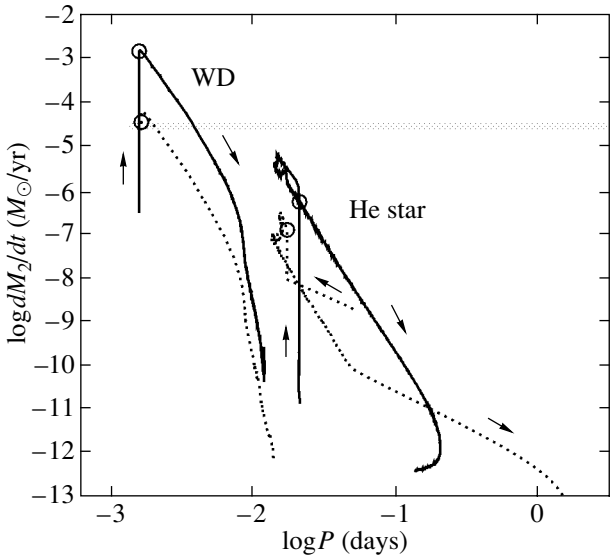

Fig. 5. Same as Fig. 3 for two types of donor: a $0.3M_\odot$ degenerate helium dwarf (WD) and a $0.5M_\odot$ non-degenerate helium star (He star) (solid curves). The initial degree of filling of the donor Roche lobe is $D = 0.1$. The dotted curves show the corresponding tracks for a system with a stellar mass BH ($30M_\odot$) for comparison.

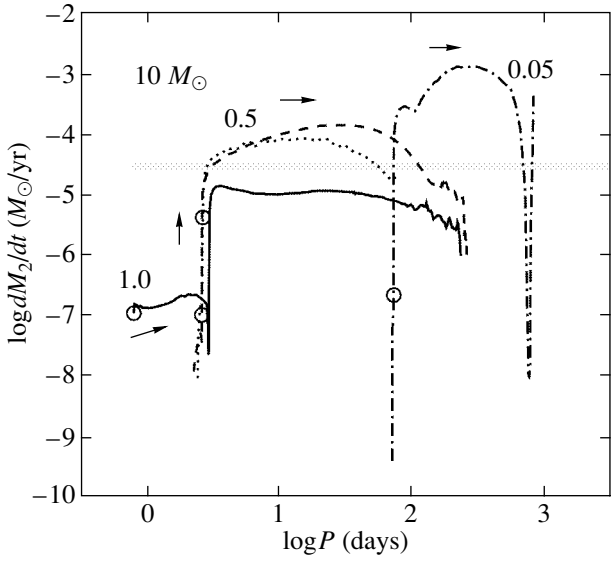

Fig. 4. Same as Fig. 3 for a $10M_\odot$ main-sequence donor.

evolution of the system becomes more "conservative" in terms of the orbital angular momentum, and the dominant factor becomes the increase in the period due to the influence of the ISW, since the characteristic time for mass transfer between the components via the ISW becomes shorter than the time scale for the loss of angular momentum from the system via GWR and the magnetic stellar wind. As a result, the donor does not fill its Roche lobe and high mass-loss rates are not achieved. However, there are arguments suggesting that such a large enhancement in the ISW is not likely: our studies of the evolution of low-mass X-ray binaries with neutron-star accretors [47] show that, if the ISW intensity becomes too high, the period gap displayed by the theoretical tracks for these binaries becomes substantially broader than is observed.

5. CONCLUSIONS

The goal of this work was to investigate the role of intermediate-mass BHs (10^2–$10^4M_\odot$) in the creation of ultra-luminous X-ray sources ($L_X \gtrsim 10^{38}$ erg/s). It is obvious that most of these sources are X-ray binaries whose accretors are stellar-mass BHs (5–$100M_\odot$) [11]. However, to obtain a more complete picture of the evolution of massive close binaries and to more accurately interpret the available observations of comparatively soft (0.1–2 keV) ultra-luminous X-ray sources [5, 53], we carried out numerical studies of the evolution of binaries with accreting BHs with mases of $\sim 3000M_\odot$.

Our analysis of the three main scenarios for the formation of intermediate-mass BHs in the cores of globular clusters—the superstar, accretion, and stellar-mass BH-merger mechanisms—identifies the last as the dominant, if not only, scenario. The stellar-mass BHs—especially the most massive—are first

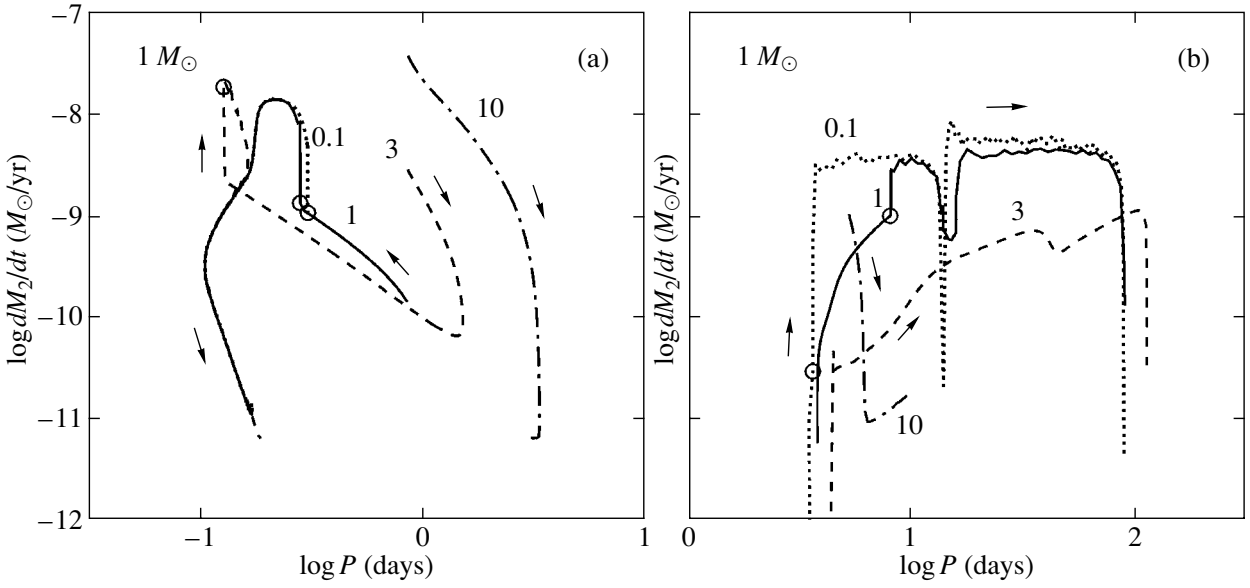

Fig. 6. Same as Fig. 1 for four GWR intensities: the standard value (solid curves), a factor of ten lower (dotted curves), a factor of three higher (dashed curves), and a factor of ten higher (dot–dashed curves). The computations were carried out for initial degrees of filling of the donor Roche lobe of (a) $D = 0.5$ and (b) 0.15. The factor by which the standard GWR intensity is multiplied is indicated near the curves.

decelerated in the stellar fields of dense, massive globular clusters, gradually approaching the cluster centers. In last stages of this process, gravitational-wave radiation by close binary systems consisting of BH components plays an active role in bringing about the merger of the components. This ultimately leads to the formation of a BH with a mass of $\sim 1000 M_\odot$ in the cluster core. This scenario can be generalized to the formation of supermassive BHs in the nuclei of galaxies via the tidal deceleration of the most massive globular clusters in the most massive parent galaxies, as well as via the tidal deceleration of the galaxies themselves in dense clusters of galaxies [8].

The other two scenarios encounter difficulties. The formation of a superstar with a mass of $\sim 1000 M_\odot$ in the core of a globular cluster requires an initial density for the cluster that is too high. In addition, it is not clear to what extent the stellar wind of the superstar, which is likely to be very intense, could hinder the growth in its mass. The accretion-disk scenario for the formation of supermassive BHs ($M > 10^6 M_\odot$) associated with the spherical populations of galaxies probably leads to an overproduction of X-ray emission in the Universe, suggesting we should be cautious about adopting it as the main mechanism for the growth of nonstellar BHs. These arguments constrain the role of accretion in the growth of intermediate-mass BHs to a few percent of their total masses.

The creation of a bright X-ray source near a $\sim 1000 M_\odot$ mass BH requires a high disk accretion rate: $\sim 10^{-8} - 10^{-5} M_\odot$/yr. There are several ways in which such accretion rates can be achieved in a globular cluster, such as the presence of nearby planetary nebulae, the tidal disruption of cluster stars passing through the Roche lobe of the central BH, and Roche-lobe filling by a close companion. The last possibility is most probable, and could come about as a result of the tidal capture of solar-mass field stars. Figures 1 and 2 show that the mean accretion rate remains comparatively low for solar-mass donors—no more than $\sim 10^{-7} M_\odot$/yr. However, it should be borne in mind that due to accumulation instabilities in the accretion disk, the accretion rate onto a BH with a mass of $\sim 1000 M_\odot$ can reach the Eddington limit of the latter, $\sim 10^{-5} M_\odot$/yr, for a short time [5, 7]. In addition, the donor could be a more massive star, leading to accretion rates of the same order of magnitude (Figs. 3, 4). Our analysis indicates a low rate of formation of binary systems with intermediate-mass BHs, which is likely the origin of the relatively small number of corresponding X-ray systems.

Note that some compact X-ray sources near the nuclei of nearby galaxies with luminosities of $10^{37} - 10^{40}$ erg/s [1] could be sources of this type. Their nearness to the nuclei of their parent galaxies ($\lesssim 1$ kpc) could reflect the deceleration of these BHs and the globular clusters surrounding them. The X-ray luminosities of these sources (Figs. 1, 2) do not differ from the luminosities of X-ray binaries containing neutron stars and stellar-mass BHs,

but the X-ray spectrum may provide an indicator of the presence of a close binary containing an intermediate-mass BH ($\sim 1000 M_\odot$). The X-ray spectrum of X-ray binaries containing intermediate-mass BHs should be soft, due to the large size of the hot region on the accretion disk. The characteristic energy of thermal photons is determined by the ratio $\epsilon \sim (dM/dt)^{1/4} M_{BH}^{-1/2}$ [41]. It is possible that this property can be used to distinguish intermediate-mass BHs from other X-ray sources.

Note that the detection of binarity of such sources is a difficult observational task. These systems are very weak in the optical due to their considerable distances. They are also weak in the X-ray, complicating searches for eclipses. As we noted above [see (18) and Fig. 2], the orbital periods of semi-detached systems with massive accretors are nearly independent of the accretor mass, and are determined overall by the radius and mass of the donor (m). However, even under the most favorable circumstances, the relative duration and probability of the eclipses is $\sim 0.1 (m/M)^{1/3}$, and falls with growth in the accretor mass (M). It is clear that, with $M \sim 1000 M_\odot$ and $m \sim M_\odot$, the relative duration and probability of an eclipse will be ~ 0.01 of the orbital period, making searches for eclipses in these weak and often non-stationary X-ray sources difficult.

ACKNOWLEDGMENTS

This work was supported by the Federal Science and Technology Program in Astronomy, the Russian Foundation for Basic Research (project no. 03-02-16254), and the Program for Support of Leading Scientific Schools of Russia (NSh-00-15-96533).

REFERENCES

1. E. Colbert and R. Mushotzky, Astrophys. J. **519**, 89 (1999).
2. G. Fabbiano *et al.*, Astrophys. J. **584**, L5 (2003).
3. A. Tutukov and A. Fedorova, Astron. Zh. **81**, 589 (2004) [Astron. Rep. **48**, 534 (2004)].
4. K. Gebhardt, R. Rich, and L. Ho, Astrophys. J. **578**, L41 (2002).
5. Q. Wang, T. Yao, W. Fukui, *et al.*, astro-ph/0403413 (2004).
6. J. Miller, G. Fabbiano, M. Miller, *et al.*, Astrophys. J. **585**, L37 (2003).
7. M. Gilfanov, astro-ph/0403552 (2004).
8. A. Tutukov, Astron. Zh. (2004, in press).
9. J. Gerssen, R. Marel, K. Gebhardt, *et al.*, Astron. J. **125**, 376 (2002).
10. A. Tutukov and A. Fedorova, Astron. Zh. **78**, 762 (2002) [Astron. Rep. **45**, 659 (2002)].
11. A. Tutukov and A. Fedorova, Astron. Zh. **81**, 589 (2004) [Astron. Rep. **48**, 534 (2004)].
12. R. Humphreys, G. Fabbiano, M. Elvis, *et al.*, Mon. Not. R. Astron. Soc. **344**, 134 (2003).
13. M. Hideaki and T. Voshiaki, Astrophys. J. **585**, 259 (2002).
14. P. Zwart, F. Simon, and L. Stephen, Astrophys. J. **576**, 899 (2002).
15. P. Zwart, Amer. Astron. Soc. Meeting, 20310203P (2003).
16. C. Miller, AIP Conf. Proc. **686**, 125 (2003).
17. A. V. Tutukov and L. R. Yungelson, Mon. Not. R. Astron. Soc. **260**, 675 (1993).
18. A. V. Tutukov and L. R. Yungelson, Astron. Zh. **79**, 738 (2002) [Astron. Rep. **46**, 667 (2002)].
19. H. Lamers, N. Panagia, S. Scuder, *et al.*, Astrophys. J. **566**, 818 (2002).
20. S. Zwart, H. Baumgardt, P. Hut, *et al.*, astro-ph/0402622 (2004).
21. M. Miller, M. Coleman, D. Hamilton, *et al.*, Mon. Not. R. Astron. Soc. **330**, 232 (2002).
22. A. Men'shchikov and A. Tutukov, Astrofizika **29**, 714 (1989) [Astrophys. **29**, 495 (1989)].
23. A. G. Masevich and A. V. Tutukov, *Stellar Evolution. Theory and Observations* (Nauka, Moscow, 1988) [in Russian].
24. C. Vignali, astro-ph/0403100 (2004).
25. A. Finogenov, U. Briel, J. Henry, *et al.*, astro-ph/0403216 (2004).
26. J. Wyithe and A. Loeb, Astrophys. J. **595**, 614 (2003).
27. A. V. Tutukov and A. M. Cherepashchuk, Astron. Zh. **80**, 419 (2003) [Astron. Rep. **47**, 386 (2003)].
28. C. W. Allen, *Astrophysical Quantities* (Athlone Press, London, 1973; Mir, Moscow, 1977).
29. Yo. Taniguchi, Ya. Shiova, T. Tsuru, *et al.*, Publ. Astron. Soc. Jpn. **52**, 533 (2000).
30. D. Merritt, S. Piatek, S. Zwart, *et al.*, astro-ph/0403331 (2004).
31. B. C. Whitemore, astro-ph/0403709 (2004).
32. M. Favata, S. Hughes, and D. Holz, astro-ph/0402056 (2004).
33. P. Freier, M. Kramer, A. Lyne, *et al.*, Astrophys. J. **557**, L105 (2001).
34. G. Knapp, J. Gunn, P. Bowers, *et al.*, Astrophys. J. **462**, 231 (1996).
35. D. Spergel, Nature **352**, 221 (1991).
36. J. Halpern, S. Gerari, S. Komossa, *et al.*, Astrophys. J. **592**, 42 (2003).
37. C. Hopman, S. Zwart, and T. Alexander, Astrophys. J. **604**, 65 (2004).
38. S. Kobayashi, P. Laguna, E. Phinney, *et al.*, astro-ph/0404173 (2004).
39. H. Baumgardt, J. Makino, and T. Ebisuzaki, astro-ph/0406227 (2004).
40. H. Baumgardt, J. Makino, and T. Ebisuzaki, astro-ph/0406231 (2004).
41. A. Tutukov and Ya. Pavlyuchenkov, Astron. Zh. (2004, in press).
42. C. Hopman, S. Zwart, and T. Alexander, Astrophys. J. **604**, L101 (2004).
43. A. Alonso-Herrero, G. Rieke, M. Rieke, *et al.*, Astron. J. **124**, 166 (2002).

44. S. Larsen, Mon. Not. R. Astron. Soc. **319**, 893 (2000).
45. S. Larsen, astro-ph/0403244 (2004).
46. L. Zampieri, P. Mucciurelli, R. Falomo, *et al.*, astro-ph/0310739 (2003).
47. I. Iben, Jr., A. V. Tutukov, and A. V. Fedorova, Astrophys. J. **486**, 955 (1997).
48. I. Iben, Jr., A. V. Tutukov, and L. R. Yungelson, Astrophys. J., Suppl. Ser. **100**, 233 (1995).
49. V. V. Muzylev and A. V. Tutukov, Nauchn. Inform. Astrosovet Akad. Nauk SSSR **26**, 3 (1973).
50. B. Paczynski, Annu. Rev. Astron. Astrophys. **9**, 183 (1971).
51. L. D. Landau and E. M. Lifshitz, *The Classical Theory of Fields* (Nauka, Moscow, 1962; Pergamon Press, Oxford, 1971).
52. A. Jordan, P. Cote, L. Ferrarese, *et al.*, astro-ph/0405188 (2004).
53. P. Kaaret, A. Prestwich, A. Zezas, *et al.*, Mon. Not. R. Astron. Soc. **321**, L29 (2001).

Translated by D. Gabuzda